GEOCHEMISTRY OF KARST DEPOSITS IN BORNEO DETAILING HYDROCLIMATE VARIATIONS IN THE WARM POOL ACROSS THE LATER PLEISTOCENE

A Dissertation
Presented to
The Academic Faculty

By

Stacy Carolin

In Partial Fulfillment
Of the Requirements for the Degree
Doctor of Philosophy
in the School of Earth and Atmospheric Science

Georgia Institute of Technology
August, 2014

GEOCHEMISTRY OF KARST DEPOSITS IN BORNEO DETAILING HYDROCLIMATE VARIATIONS IN THE WARM POOL ACROSS THE LATER PLEISTOCENE

Approved By:

Dr. Kim Cobb, Advisor
School of Earth and Atmospheric Science
Georgia Institute of Technology

Dr. Jess Adkins
Division of Geological and Planetary Sciences
California Institute of Technology

Dr. Peter Webster
School of Earth and Atmospheric Science
Georgia Institute of Technology

Dr. Jean Lynch-Stieglitz
School of Earth and Atmospheric Science
Georgia Institute of Technology

Dr. Taka Ito
School of Earth and Atmospheric Science
Georgia Institute of Technology

Dr. Martial Taillefert
School of Earth and Atmospheric Science
Georgia Institute of Technology

Date Approved: June 17, 2014

To

Temango Bayak Malang, Penghulu Lejau Malang, TK Tama Kasip Epoi Baluluk,
SPG Syria Lejau and SPG Jenny Malang
Guardians of Orang Ulu and Mulu National Park

ACKNOWLEDGEMENTS

My biggest thank you is to Guillaume, whose ridiculously generous personality never ceases to amaze me. Guillaume has stopped his life to come assist me with the Neptune more times than I can remember, and not once has he done it without the quintessential French charm that is the only thing that can keep me from putting my head through the wall. Guillaume, your charitable actions and smirky grin are contagious, I am so fortunate to have spent 4 years in and out of your office. My wish is that all the future scientists I work with have half as big a heart as yours.

Thank you also to my core group of motivators and science lovers: Jessica, Andrea, and James. You all taught me that there do exist truly good people in this sometimes outrageous world of scientists. I look forward to all the stories we will share for the next 30 years.

Thank you to Kim and Jess, my science parents. Kim saw my science potential well before I ever did, and it was her pushing (yes, on our leech-filled hike out of Camp 5 in 2008) that made me finally begin to even consider graduate school. Two years later I came around. There have definitely been many bumps along the road, but Kim has always worked to adjust to my wandering mind, and fortunately for both of us in the end her hard work paid off. Jess has likewise had an incredible impact on my science life. Apart from coming to find me in the hospital after my near-fatal Hollywood bike accident to throwing my wife and I our own backyard BBQ wedding party, Jess has guided me in science and life in ways that I cannot begin to describe. Thank you Jess for showing me the light, in more ways than one.

Thank you to my lab families: Jessica, Hussein, Pam, Bronwen, Jess Conroy, Eleanor, Liz, Corey (east coast) and Andrea, James, Guillaume, Morgan, Sophie, Ted, Adam, Nithya (west coast) and my home family: Mom, Dad, Jen, Melanie, Bryan, Grandma, and Nanny.

And thank you most of all to my wife. We met in 2008 on my first Borneo field expedition, and unbelievably to both of us, six years later we exchanged rings in California. Life is crazy, and we are happy to be in the whirlwind together.

Stacy Carolin

June, 2014

TABLE OF CONTENTS

LIST OF TABLES

LIST OF FIGURES

stalagmite 160 ky record (200yr sampling resolution). Citations provided in Figure 3.4.

LIST OF SYMBOLS AND ABBREVIATIONS

WPWP	West Pacific Warm Pool
IPWP	Indo Pacific Warm Pool
ENSO	El Niño Southern Oscillation
SST	sea surface temperature
SLP	sea level pressure
SSS	sea surface salinity
ITCZ	Intertropical Convergence Zone
LGM	Last Glacial Maximum
NH	Northern Hemisphere
SH	Southern Hemisphere
P-E	Precipitation minus evaporation
AMOC	Atlantic Meridional Overturning Circulation
WEP / WP	West equatorial Pacific
EEP / EP	East equatorial Pacific
GHG	Greenhouse gas
GCM	Global climate model
G-IG	Glacial-Interglacial
JJA	June July August
$\delta^{18}O$	Oxygen isotopic composition
VPDB	Vienna Pee Dee Belemnite isotopic standard
SMOW	Standard mean ocean water standard

D/O events	Dansgaard-Oeschgar events
^{xxx}U	Uranium isotopes
^{xxx}Th	Thorium isotopes
MC-ICPMS	Multi-collector Inductively coupled plasma mass spectrometer
PTFE	Polytetrafluoroethylene (Teflon)
HNO_3	Nitric acid
$HClO_4$	Perchlorate acid
HCl	Hydrochloric acid
NH_4OH	Ammonium hydroxide
MQ water	Ultra pure water out of Milli-Q system
CRM-145	Uranium isotope standard
SEM	Secondary electron multiplier
PFA	perfluoroalkoxy polymer resin (Teflon)
MIC	Multi ion counter
IC3, IC4	Ion counters
HF	Hydrogen fluoride
H_3PO_4	Phosphoric acid
O_2	oxygen
N_2	nitrogen
CO_2	Carbon dioxide
λ_{xxx}	Decay constant
(X/Y)	Activity ratio between X and Y
ppm	Parts per million

ppb	Parts per billion
ppt	Parts per trillion
ppmv	Parts per million by volume
MSWD	Mean Square of Weighted Deviates
df	Degrees of freedom
2σ	2-sigma error (95% confidence level)
MIS	Marine Isotope Stage
NADW	North Atlantic Deep Water
kybp	Thousand years before present
EASM	East Asian summer monsoon
IASM/ AISM	Indo-Australian summer monsoon
DRE	dense rock equivalent
SCS	South China Sea

SUMMARY

Variability in the tropical ocean-atmospheric system causes global scale climate anomalies, most evident in the El Niño-Southern Oscillation's coupled climate feedbacks. Despite being an area of high interest, many questions still remain regarding the tropical Pacific's response to external forcing, particularly its response to increases in anthropogenic greenhouse gases. Paleoclimate reconstructions coupled with model simulations provide insight into the tropical Pacific's role in past climate variability. Most paleoclimate records, however, still lack the resolution, length, and chronological control to resolve rapid variability against a background of orbital-scale variations. In this study we present stalagmite oxygen isotope ($\delta^{18}O$) reconstructions that provide reproducible centennial-scale records of western Pacific hydrologic variability that are U/Th-dated and continuous throughout most of the late Pleistocene.

In Chapter 2 we use four overlapping stalagmite $\delta^{18}O$ records to investigate millennial-scale climate variability in the last glacial period. We find that regional convection likely decreased during the six massive iceberg discharges defined in the North Atlantic sediment records (so-called "Heinrich events"). The inferred western tropical Pacific dry events aligned with all six Heinrich events are consistent with a southward shift of the Intertropical Convergence Zone, the dominant paradigm to explain global climate anomalies originating in the north Atlantic. However, any hydrologic variability related to Dansgaad-Oeschgar (D/O) events, millennial-scale sawtooth temperature anomalies of the last glacial period first evident in the Greenland ice records,

is notably absent in the tropical stalagmite records. The absence of any coherent D/O signal in the Mulu stalagmites suggests D/O events and Heinrich events may be characterized by fundamentally different climate mechanisms and feedbacks.

In Chapter 3 we extend the record back through 160kybp to comprise an entire glacial-interglacial cycle, enabling the investigation of orbital-scale climate forcings as well as the comparison of two well-dated glacial terminations in the western tropical Pacific. The ice-volume-corrected stalagmite $\delta^{18}O$ records suggest that glacial forcing, characterized by lower atmospheric CO_2 and cooler global temperatures, did not drive significant changes in Mulu rainfall $\delta^{18}O$. Further, no significant correlation exists between Borneo stalagmite $\delta^{18}O$ and either global sea level shifts or Sunda Shelf areal exposure. The Borneo record does vary in phase with local mid-fall equatorial insolation, suggesting that precessional forcing may impart a strong influence on hydroclimate variability in the West Pacific Warm Pool. The dominance of precessional forcing is best illustrated across Glacial Termination II, when the oscillation of equatorial fall insolation is large and out of phase with ice sheet decay.

In Chapter 4 we summarize two areas of ongoing and future research: (1) investigating the climate effects of the Toba super-eruption through geochemical tracers in Mulu stalagmites, and (2) modeling the Mulu karst hydrologic system to explore why Mulu stalagmites are so depleted in ^{234}U relative to most other karst settings.

Appendix A presents a summary of best-practices in U-series dating used to minimize analytical errors. Appendix B and C provide the Supplementary Materials to Chapter 2, “Varied response of western Pacific hydrology to climate forcings during the

last glacial period" and Chapter 3, "0-160kybp multi-stalagmite $\delta^{18}O$ record from northern Borneo."

CHAPTER 1

INTRODUCTION

1.1 Tropical Pacific Warm Pool: a paleoclimate target

Variability of the West Pacific Warm Pool (WPWP) hydrologic cycle today causes global scale climate anomalies through teleconnections within the coupled ocean-atmosphere system (eg., Ropelewski and Halpert, 1987), most evident during El Niño Southern Oscillation (ENSO) extremes. The disruption of zonal sea surface temperature (SST) and sea level pressure (SLP) gradients, and the adjustment of the thermocline depth in the tropical Pacific that occur during El Niño (warm phase) and La Niña (cool phase) events, have dramatic impacts on large-scale atmospheric heating, meridional and zonal atmospheric circulation, and global hydrology (eg. Cane and Clement, 1999). Despite decades of research on the ENSO cycle, many questions still remain regarding the tropical Pacific's response to variable internal and external forcings on lower frequencies. Indeed, our understanding of the tropical Pacific's role in past climate change is poorly resolved by most existing paleoclimate records from this region, which are relatively low-resolution, short, and poorly dated.

Over the past decade, many paleoclimate studies have sought to reconstruct tropical Pacific temperature and hydrology. Several WPWP marine sediment records have investigated SST and sea surface salinity (SSS) variability at high-resolution targeting the last glacial maximum through the Holocene (Stott et al., 2002, 2007; Koutavas et al., 2002; Rosenthal et al., 2003; Visser et al., 2003; Lea et al., 2005; Levi et al., 2007; Steinke et al., 2008; Xu et al., 2008; Gibbons et al., 2013), or at lower-

resolution targeting multiple glacial cycles (Lea et al., 2000; Oppo et al., 2003). More recently, stalagmite records, which can be absolutely dated via U-series dating and sampled at relatively high temporal resolution, have examined rainfall variability that spans most of the last glacial period at multiple sites around the tropical western Indo-Pacific (Partin et al., 2007; Griffiths et al., 2009; Meckler et al., 2012; Carolin et al., 2013; Denniston et al., 2013a,b,c; Ayliffe, et al., 2013).

Modeling studies provide an important complement to paleoclimate reconstructions, as they focus on comparing the existing archive of paleoclimate data with model output to probe the mechanisms of past climate change, and to test the accuracy of climate models (eg. Clement et al., 1999, 2004; Zhang and Delworth, 2005; Timmerman et al., 2007; DiNezio et al., 2011; DiNezio and Tierney, 2012). For example, comparison studies relate stalagmite hydrologic reconstructions along a meridional transect in the western Pacific to Zhang and Delworth's (2005) hosing experiments and modeled shifting of the ITCZ. This comparison plays a key role in strategies to improve state-of-the-art global circulation climate models' accuracy in projecting future climate change (see Schmidt et al., 2013).

1.2 Orbital-scale hydroclimate variability

Global climate over the past two million years has been dominated by glacial cycles with periods of 23ky, 41ky, and 100ky (eg. Imbrie et al., 1984; Mix et al., 1995; Petit et al., 1999; Lisiecki and Raymo, 2005; Luethi et al, 2008). The statistical correlations between global temperature or atmospheric pCO_2 and the parameters of earth's orbit (precession, obliquity, and eccentricity) support the Milankovitch theory that insolation variations cause significant changes in climate (Milankovitch, 1941). The polar

temperature, pCO_2, and global ice volume have been found to all vary concurrently in the canonical 100ky G-IG sawtooth pattern (abrupt deglaciation followed by gradual trend toward maximum glaciation).

Glacial-interglacial cycles in the tropics allow us to investigate the response of the coupled tropical ocean-atmosphere system to orbital-scale glacial forcing (ice volume, global temperature, CO_2). Long tropical marine records examine the coupling of greenhouse gas levels and tropical SSTs. Late Pleistocene alkenone-based SST records from global tropical sites (Herbert et al., 2010) and Mg/Ca-derived SST records from the equatorial east and west Pacific (Lea et al., 2000) show consistent SST changes synchronized with the atmospheric pCO_2 cycle, linking orbital-scale SST variations to the high latitudes (Lea et al., 2004; Herbert et al., 2010). Lea et al. (2004) suggests that on orbital time scales varying atmospheric CO_2 is the dominant forcing on tropical climate. Other higher-resolution western tropical SST records from glacial terminations agree, with the SST rise aligned with the rise in atmospheric CO_2 (eg. Stott et al., 2007; Visser et al., 2003). Notably, one last deglaciation SST record from the cold tongue found SST to instead vary most coherently with precession-induced changes in seasonality, instead of the CO_2 rise (Koutavas et al., 2002).

Relatively few paleodata studies resolve orbital-scale hydrologic variability in the tropical Pacific. Tropical to subtropical cave stalagmite records (25-32^{o}N) from China resolve several glacial-interglacial cycles and show east Asian summer monsoon (EASM) strength to strongly correlate with northern hemisphere (NH) summer precession (Wang et al., 2008; Cheng et al., 2009). Clement at al.'s (2004) modeling study comparing precession (modern boundary conditions) experiments and Last Glacial Maximum

experiments found that tropical hydrology responded equally to glacial forcing and precessional forcing.

Variations in ENSO frequency/strength and meridional shifts in the Intertropical Convergence Zone (ITCZ) drive a large portion of modern-day hydrological variability in the tropical Pacific. Forcing of tropical hydrological variability due to past variations in ENSO frequency/strength is still highly debated. A compilation of Pacific and east Indian SST records of the last deglaciation suggests the tropical Pacific moves between an "amplified ENSO" state and a "damped ENSO" state driven by orbital precession (Koutavas and Joanides, 2012). A compilation of Pacific and east Indian ice-volume adjusted $\delta^{18}O_{sw\text{-}ice}$ records of the last deglaciation, however, do not support a significant role for an ENSO-like mechanism on glacial–interglacial time scales, or during millennial events of the last deglaciation (Gibbons et al., 2013).

1.3 Glacial millennial-scale hydroclimate variability

Studies of north Atlantic sediments show that the circulation of surface and deep waters were repeatedly perturbed during the glacial period of Marine Isotope Stages 2 – 4 (~12 thousand years before the present (kybp) to ~74kybp) by massive surges and melting of icebergs, known as "Heinrich events" (eg. Heinrich, 1988). The duration of the discharge of icebergs from the Laurentide Ice Sheet through the Hudson Straight ranges from ~500 to ~2000 years, depending on the event and the sample core (Hemming, 2004). Heinrich events are characterized by an extreme millennial-scale cold period followed by an abrupt warming in the North Atlantic. The massive iceberg discharge suggests an abrupt large influx of freshwater to the North Atlantic and a

subsequent shutdown of north Atlantic deep water (NADW) production (eg. Hemming 2004).

Large millennial-scale sawtooth temperature anomalies in the Greenland ice cores occurred repeatedly throughout the last glacial period (Dansgaard, 1993), and have been observed in a wide range of NH records (eg., Clement and Peterson, 2008), yet the mechanisms surrounding these abrupt climate change events remain unclear. D/O events are defined differently than Heinrich events: the former refers to NH temperature anomalies derived from ice cores, while the latter is defined by the amount of ice rafted debris in marine sediments. The decadal-scale abrupt warming of a D/O event may follow a Heinrich event stadial period. Glacial records from proxies across the NH show similar recorded variability to these termed "Dansgaard-Oeschgar (D/O) events" (e.g., Sachs and Lehman, 1999; Hendy and Kennett, 2000; Shackleton et al., 2000; Peterson et al., 2000; Altabet et al., 2002; Schulz et al., 1998; Wang et al., 2001). Other studies show evidence of D/O events in the southern hemisphere (SH) tropics (Kanner et al., 2012; Cheng et al, 2013b; Denniston et al 2013) and Antarctica (EPICA Community Members, 2005).

Several studies suggest that the north Atlantic region may be the dominant driver of millennial-scale tropical hydroclimate anomalies. Studies suggest that a weakening of the Atlantic meridional overturning circulation (AMOC) and/or a dramatic increase in north Atlantic albedo due to sea ice cover would drive a southward shift of the ITCZ (Zhang and Delworth, 2005; Chiang and Bitz, 2005). Further, analysis of inter-hemisphere ice core records reveals an interesting coupling between the two poles: a strong and consistent inverse relationship exists, whereby Antarctic warming leads

Greenland cooling (EPICA Community Members, 2005). The reigning paradigm for explaining the "bipolar seesaw" of climate signals invokes a collapse of the ocean's meridional overturning circulation (Broecker, 1998).

Recent stalagmite records from the western tropical Pacific region have begun to provide insight on the mechanisms responsible for glacial millennial-scale hydroclimate variability in the western tropical Pacific. Together with the Chinese stalagmite $\delta^{18}O$ records, stalagmite $\delta^{18}O$ records from Liang Luar cave in Flores, Indonesia ($8^{o}S$, $120^{o}E$) (Ayliffe et al., 2013) and Ball Gown cave in tropical northern Australia ($17^{o}S$, $125^{o}E$) (Griffiths et al., 2013a) form a meridional transect (Wang et al., 2001). The 0-31kybp Flores $\delta^{18}O$ record suggests abrupt southward shifts in the Australian-Indonesian monsoon (IASM) synchronous with north Atlantic cold intervals of the deglaciation, with the most pronounced signal directly in phase with Heinrich stadial 1 (14.6-17.6kybp). The tropical northern Australia study resolves 8-27kybp and 31-40kybp, and also suggests increased IASM rainfall to be coincident with Heinrich stadials and the Younger Dryas. The Australian $\delta^{18}O$ record further claims to have found decreased rainfall coincident with D/O event interstadials.

Marine records of the tropical western Pacific provide insight into tropical Pacific hydrology by reconstructing seawater $\delta^{18}O$ from forams, which is sensitive to changes in precipitation minus evaporation (P-E). A high-resolution glacial record on the eastern edge of the Philippines ($6^{o}N$, $125^{o}E$) contains evidence that D/O events impacted WPWP hydrology, with higher (lower) salinities corresponding to high latitude cooling (warming) (Stott et al., 2002). Another high-resolution glacial marine record from the Sulu Sea ($8^{o}N$, $121^{o}E$) found that millennial-scale variations in planktonic $\delta^{18}O$ were out

of phase with Mg/Ca-derived SST, suggesting that seawater $\delta^{18}O$ (and by extension, sea surface salinity (SSS)) varied over D/O events, in agreement with Stott et al. (2002). Evidence for D/O events in both marine records, however, is somewhat marginal given the relatively low resolution of the records with respect to the millennial-scale signals of interest (100-300yr/sample in the Sulu Sea record and 500yr/sample in the Philippine record).

1.4 Glacial terminations

Over the course of a deglaciation, sea levels rise approximately 125 meters due to ice sheet melting (eg. Waelbroeck et al., 2002), atmospheric CO_2 increases by ~100 ppmv (eg. Petit et al., 1999), and global average temperatures increase by ~3^{o}C (Shakun et al., 2012). The trigger for this massive reorganization of earth's climate and the sequence and timing of ice age terminations from region to region remain highly debated. The Milankovitch orbital forcing theory (Milankovitch, 1941) of ice sheet growth and decay does not completely explain glacial terminations, as there are some intervals in the glacial record in which northern summer insolation increases without a coupled glacial termination, and other full terminations, such as Termination 2 (130kybp) and 4 (340kybp), that occur while northern summer insolation is low. Denton et al.'s (2010) "Essential Elements of a Termination" begins with a large and isostatically depressed NH ice sheet and rising NH summer insolation. The increased insolation causes ice sheet melting that delivers fresh water to the North Atlantic. The ensuing reduced AMOC produces cold NH stadials and shifts the ITCZ south, weakening monsoon strength in east Asia. A bipolar seesaw ensues which warms Antarctica and raises atmospheric CO_2 above the threshold needed to sustain interglacial conditions. Denton et al. (2010)

propose that the critical climate threshold for an ice age termination involves (1) rising NH summer insolation and (2) large NH ice sheets prone to instabilities, with a key factor that the delivery of freshwater to the Atlantic must have persisted for long enough to raise CO_2 above a minimum level.

Multiple overlapping stalagmite $\delta^{18}O$ records from tropical and subtropical China cover the last 380ky, resolving four glacial-interglacial terminations (Cheng et al. 2009, Yuan et al., 2004; Dykoski et al., 2005). The authors found that all EASM terminations originated with a multiple-thousand year "weak monsoon interval" that began when NH summer insolation was low but increasing. They concluded that rising summer insolation triggers the disintegration of the massive ice sheet, leading to a slowing of the AMOC, southern shift of the ITCZ, rising Antarctic temperature, stronger southern hemisphere (SH) westerlies, and release of CO_2, in agreement with the Denton et al. (2010) termination theory.

Whether tropical ocean-atmosphere dynamics have any influence on the proposed Termination mechanisms is still unresolved. Lea et al. (2000) found tropical SST to lead planktonic $\delta^{18}O$ during Terminations by 3kyr, while the SST shift rise aligned with Antarctic temperature and atmospheric CO_2 from the Vostok ice core. Kawamura et al.'s (2007) Dome Fuji O_2/N_2 orbitally-tuned age scale places the midpoint of Antarctic temperature and global CO_2 Termination II at 135 kybp. Stott et al. (2007) sampled a high-resolution Termination 1 marine sediment core from 2114m in the western Pacific, whose benthic forams are bathed in upper Pacific Deep Water representative of Southern Ocean temperature and salinity. The authors suggest glacial deep water warming preceded deglacial warming in the tropical Pacific and increases in CO_2 concentration,

therefore concluding the mechanism responsible for initiating deglaciation does not lie directly in the tropics and cannot be explained solely by CO_2 forcing. Finally, a last deglaciation stalagmite $\delta^{18}O$ record from Borneo began its trend toward more enriched values (drier conditions) while tropical SST and CO_2 began to rise (Partin et al., 2007; Lea et al., 2000; Stott et al., 2007; Monnin et al., 2001). The Borneo stalagmite record reached maximum $\delta^{18}O$ values during Heinrich event 1, not the LGM (Partin et al., 2007). The authors suggest climatic feedbacks in the tropical Pacific may have played a part in driving the variability of the AMOC across H1, which in turn affected tropical Pacific hydrology (Partin et al., 2007). The deglaciation in the Borneo record may be described as 2-step, with first decreasing convective activity during temperature and CO_2 rise, followed by increasing convective activity through the latter half of the deglaciation.

1.5 Gunung Mulu National Park hydroclimate and karst

Gunung Mulu National Park on the northern side of Borneo island (4^oN) is situated in the center of the Indian and west Pacific Warm Pools (115^oE), and is an ideal field site for investigating past tropical Pacific climate variability using stalagmite proxies. An outcrop of Melanau limestone, covered with dense tropical rainforest, forms a band of limestone hills on the eastern shale and sandstone slopes of 2375m high Gunung Mulu (Figure 1.1), and receives over 5 m of rainfall per year percolating into the rock and throughout the vast cave chambers, 295 km explored (Figure 1.2) (Mulu Caves 2009 Expedition Report). There is little seasonal variability in both temperature and rainfall amount at our site (Moerman et al., 2013) due to the present annual meridional migration of the ITCZ in the western Pacific (Xie and Arkin, 1997). Presently, the largest shifts in convective activity occur during ENSO extremes. During an El Niño event, warm SSTs in the central and

eastern Pacific drive convective activity eastward, leading to drier conditions over the Warm Pool. During a La Niña event, convection strengthens over Borneo (eg. Cobb et el., 2007).

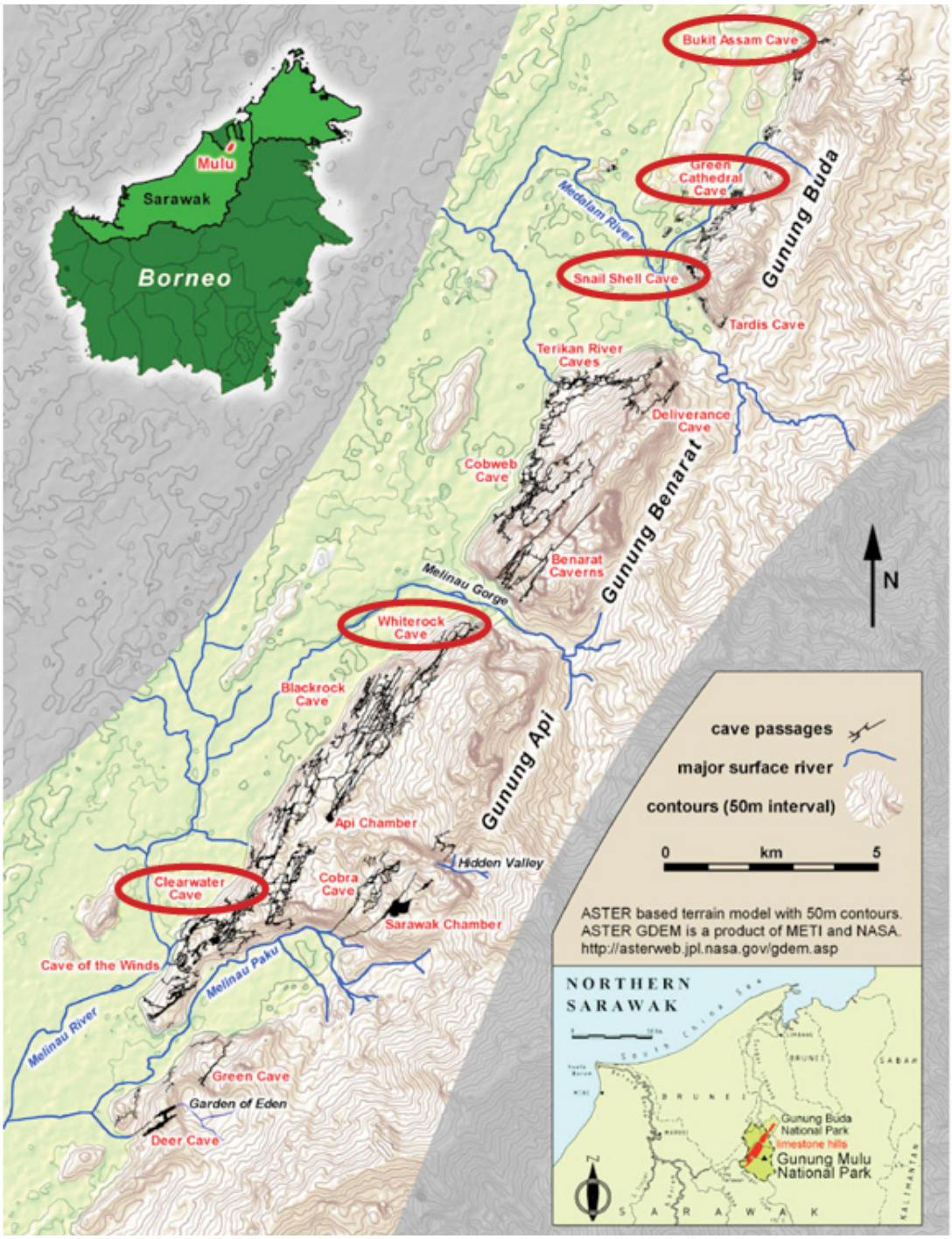

Fig. 1.1. Caves of Gunung Mulu National Park with cave study sites indicated. From *J. Wooldridge and T. Waltham, in Encyclopedia of Caves 2nd Ed. (2012)*

Figure 1.2. Selected Secret Chamber (high ceiling) and Whiterock Cave (low ceiling) calcite collection sites. (Credit: Syria Lejau)

1.6 Mulu rainwater and dripwater $\delta^{18}O$ variability

Rainfall $\delta^{18}O$ variability at Mulu tracks the strength of regional convective activity (Moerman et al., 2013). Consistent with the tropical amount effect (Dansgaard 1954; Rozanski et al.,1992), rainfall $\delta^{18}O$ variations measured at Mulu airport from 2005-2011 are significantly anti-correlated with regional precipitation amount at monthly and longer timescales, closely tracking the Madden-Julian Oscillation and ENSO (Moerman et al., 2013). Notably, a correlation between monthly averages of satellite precipitation and Mulu rainfall $\delta^{18}O$ reveals significant basin-wide correlations (Moerman et al., 2013). Additionally, a weak semi-annual seasonal cycle in rainfall $\delta^{18}O$ is characterized by relative minima in June-July and November-January, and relative maxima in February-April and August-October. Such a pattern suggests that the twice-yearly passage of the ITCZ over the site is associated with shifts in the moisture sources and/or trajectories that drive the observed seasonal fractionations (Moerman et al., 2013). Dripwater $\delta^{18}O$ values match rainfall $\delta^{18}O$ values averaged over the preceding 3-9 months (Moerman et al, in prep), suggesting a short residence time of dripwater $\delta^{18}O$ relative to our centennial-scale sampling of stalagmite $\delta^{18}O$.

1.7 Mulu stalagmite $\delta^{18}O$ proxy

At equilibrium conditions, the isotopic composition of calcite formed from super-saturated drip waters is dependent on the temperature and isotopic composition of the dripwater. An expression for the oxygen isotope fractionation between calcite and water at low temperatures is determined experimentally by Kim and O'Neil (1997), and is provided in Equation 1.1, where α is the fractionation factor and T is in kelvin.

$$1000 \ln \alpha_{H_2O}^{calcite} = \delta_{calcite} - \delta_{H_2O} = 18.03\left(\frac{1000}{T}\right) - 32.42 \quad (1.1)$$

$\delta_{calcite}$ is calculated with respect to VPDB standard, and δ_{H2O} is with respect to SMOW standard. Hendy (1971) outlined the various equilibrium and nonequilibrium processes that govern oxygen isotope variability during calcite stalagmite formation. Dorale and Liu (2009) argue that the only method that can be used to ensure isotopic equilibrium is maintained during calcite formation is to replicate oxygen isotopic values in two or more stalagmites. If the isotopic profiles correlate they conclude that the calcite formed under equilibrium conditions.

Several lines of evidence support the equilibrium precipitation of calcite in the Borneo stalagmites. A modern 5-year continuous study at Mulu measures present-day amount weighted mean rainwater $\delta^{18}O$ equal to -8.5‰ SMOW and average fast and slow drip water (3 total) $\delta^{18}O$ equal to -8.2 ± 1‰ (1σ) SMOW, which agree within error (Moerman et al., 2014, in prep). Modern calcite from one of the stalagmites used for this project is approximately -9.1‰ VPDB measured, which is in good agreement with calculated $\delta^{18}O_{calcite}$ (-8.5‰ VPDB) at equilibrium with T_{cave} = 25°C (299K), as measured in Cobb et al. (2007). Further evidence of calcite precipitation under equilibrium

conditions at our site is provided in Partin et al. (2007), where it was demonstrated that $\delta^{18}O$ values in three different stalagmites did not vary significantly across a single growth layer (the "Hendy" test). Finally, the sub-millennial scale $\delta^{18}O$ variability between multiple stalagmites extracted from several caves at most 20 km apart is also strongly correlated (Partin et al., 2007; Meckler et al., 2012; Carolin et al., 2013). This further indicates that calcite $\delta^{18}O$ variability is due to regional climate changes associated with rainfall $\delta^{18}O$ variability and not a result of precipitation at disequilibrium states.

1.8 Research scope and objectives

In this thesis, mass spectrometry is used to generate multiple overlapping $\delta^{18}O$ records coupled to well-dated U-Th age models. These reconstructions allow us to address the following research questions:

1. **What global-scale mechanisms can be invoked to explain millennial-scale climate changes in the Warm Pool during the last glacial period?**
2. **What are the relevant roles of greenhouse gases, precession, and Sunda Shelf exposure on western Pacific hydrological variability over multiple glacial-interglacial cycles?**

Chapter 2 presents four stalagmite $\delta^{18}O$ records spanning 0-100kybp and comments on the suggested hydroclimate variability in the western tropical Pacific associated with north Atlantic millennial-scale events. A preliminary investigation into the magnitude of precessional and glacial forcing is also presented.

Chapter 3 presents a large compilation of overlapping U/Th-dated Gunung Mulu stalagmite $\delta^{18}O$ records spanning 0-160 kybp. We comment on the complex response of

northern Borneo convection to both polar and tropical forcings and external insolation as demonstrated in the record. Lastly, we present a detailed multi-record comparison between Termination I and II to investigate the timing of Mulu $\delta^{18}O$ variability during deglaciations.

CHAPTER 2

. **VARIED RESPONSE OF WESTERN PACIFIC HYDROLOGY TO CLIMATE FORCINGS OVER THE LAST GLACIAL PERIOD**

.

This is a reprint of an article whose final and definitive form has been published in *Science*, authored by S.A. Carolin, K.M. Cobb, J.F. Adkins, B. Clark, J.L. Conroy, S. Lejau, J. Malang, and A.A. Tuen entitled Varied response of western Pacific hydrology to climate forcings over the last glacial period.

2.1 Abstract

Atmospheric deep convection in the west Pacific plays a key role in the global heat and moisture budgets, yet its response to orbital and abrupt climate change events is poorly resolved. Here we present four absolutely-dated, overlapping stalagmite oxygen isotopic records from northern Borneo that span most of the last glacial cycle. The records suggest that northern Borneo hydroclimate shifted in phase with precessional forcing, but was only weakly affected by glacial-interglacial changes in global climate boundary conditions. Regional convection likely decreased during Heinrich events, but other northern hemisphere abrupt climate change events are notably absent. The new records suggest that the deep tropical Pacific hydroclimate variability may have played an important role in shaping the global response to the largest abrupt climate change events.

2.2 Climate record and discussion

The response of the tropical Pacific to changes in the earth's climate system remains highly uncertain. The most recent glacial-interglacial cycle encompasses several precessional cycles, changes in ice volume, sea level, global temperature, and atmospheric pCO_2, and millennial-scale climate events, and thus provides insights into the tropical Pacific response to a variety of climate forcings. Chinese stalagmites show that East Asian monsoon strength closely tracks precessional insolation forcing over several glacial-interglacial cycles, and exhibits prominent millennial-scale variability (Wang et al., 2001; 2008). The timing and structure of these abrupt climate changes are nearly identical to millennial-scale events recorded in the Greenland ice cores (so-called Dansgaard-Oeschger (D/O) events) (Dansgaard, 1993), and in sediment records that document ice-rafted debris across the North Atlantic (so-called Heinrich events) (Heinrich, 1988; Hemming, 2004). A relatively smooth Borneo stalagmite record of the last 27,000 years provides a markedly different view of hydrology in the western tropical Pacific, showing a dominant Heinrich 1 excursion with the absence of other abrupt climate events, and sensitivity to boreal spring/fall precessional forcing (Partin et al., 2007). At its most basic, this finding illustrates the complexity of regional responses to various climate forcings, especially at sites located far from the North Atlantic, and demands a more exhaustive tropical Pacific hydrologic record encompassing a full glacial-interglacial cycle.

Here we present four overlapping stalagmite oxygen isotopic ($\delta^{18}O$) records from Gunung Buda and Gunung Mulu national parks, located in northern Borneo (4°N, 115°E) (Figure B-S1, Appendix B), that together span most of the last glacial cycle. The research

site is located near the center of the West Pacific Warm Pool (WPWP), where changes in sea surface temperatures (SST) and sea level pressure have significant impacts on large-scale atmospheric circulation and global hydrology (Cane and Clement, 1999). Using multiple stalagmites from different caves, we distinguish shared climate-related features from cave-specific signals in the overlapping $\delta^{18}O$ records.

The four stalagmite records span portions of the last glacial cycle with many intervals of overlap, based on U-series dates (Figure 2.1). Stalagmites were recovered from Secret Cave at Gunung Mulu (SC02, 37-94 kybp (thousands of years before present) and SC03, 32-100 kybp), and from Bukit Assam (BA02, 15-46 kybp) and Snail Shell Cave (SCH02, 31-73 kybp) at Gunung Buda, 20 km distance from Gunung Mulu (Figure B-S2, Appendix B). The deglacial and Holocene $\delta^{18}O$ records from stalagmite SCH02 were presented in Partin et al., 2007. Eighty-six new U/Th dates measured across the 4 stalagmites fall in stratigraphic order within 2σ errors (see Appendix A, Supplementary Materials). Large uncertainties in the $^{230}Th/^{232}Th$ ratio of the contaminant phases translate into large uncertainties associated with the correction for detrital thorium contamination. Fourteen isochrons measured across stalagmites from three separate caves give initial $^{230}Th/^{232}Th$ atomic ratios of 56 ± 11 (2σ) for Bukit Assam Cave, 59 ± 13 (2σ) for Snail Shell Cave, and 111 ± 41 (2σ) x 10^{-6} for Secret Cave (see Appendix A, Supplementary Materials), which fall within the range of previously published values from our site (Partin et al., 2007). Absolute age errors for each U/Th date were calculated with a Monte Carlo approach that combined multiple sources of error. The resulting dating errors average ±200, ±250, ±400, and ±500 yrs (2σ) for BA02, SCH02, SC02, and SC03, respectively. Age models were initially constructed by linearly interpolating

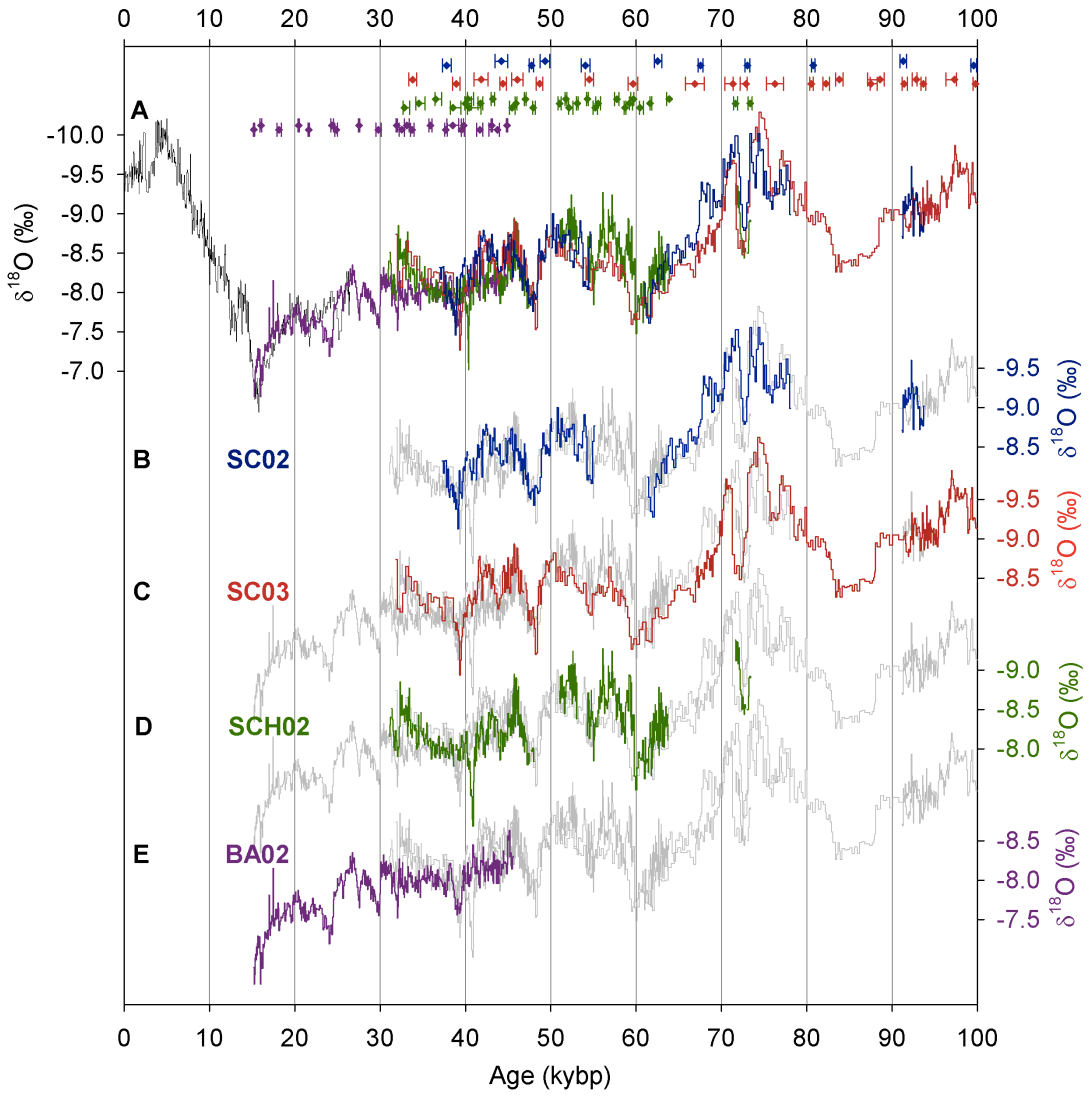

Figure 2.1. Comparison of four overlapping stalagmite $\delta^{18}O$ records from northern Borneo. (**A**) $\delta^{18}O$ records from SC02 (navy), SC03 (red), SCH02 (green), and BA02 (purple) are overlain after aligning five major millennial-scale $\delta^{18}O$ excursions shared across all four stalagmites to within 2σ dating errors (see Appendix A, Supplementary Materials), plotted with previously published stalagmite $\delta^{18}O$ data from our site (black) (Partin et al., 2007). SC03 and SC02 mean $d^{18}O$ have been offset +0.2‰ and BA02 mean $\delta^{18}O$ has been offset -0.45‰ to match the absolute value of SCH02, consistent with the prior use of SCH02 as a benchmark for the deglacial/ Holocene Borneo records (Partin et al., 2007). **(B)** The $\delta^{18}O$ record for SC02, plotted using its raw age model (navy), plotted with the three other overlapping Borneo stalagmite $\delta^{18}O$ records using their raw age models (grey). **(C)** Same as (B), but for SC03 (red). **(D)** Same as (B), but for SCH02 (green). **(E)** Same as (B), but for BA02 (purple). U–Th-based age model used to construct the aligned composite $\delta^{18}O$ record plotted in corresponding colors at top, shown with 2σ uncertainty limits (see Appendix A, Supplementary Materials).

between each date, and were refined by aligning five major millennial-scale $\delta^{18}O$ excursions visible across all four records within age error (see Appendix A, Supplementary Materials). The fact that both chronologies fall nearly completely within the StalAge (Scholz and Hoffman, 2011) algorithm's 95% confidence interval (Figures B-S3 through B-S6) adds confidence to our assigned chronologies and associated error estimates. With our 1mm sampling interval, the temporal resolution of the associated $\delta^{18}O$ records average 60 yrs/sample for faster-growing stalagmites BA02 and SCH02 and 200 yrs/sample for slower-growing stalagmites SC02 and SC03. During the 50kybp to 38kybp interval, SC02 and SC03 were sampled at 0.5mm-resolution to achieve ~100 yrs/sample resolution. Ultra-slow growth intervals (<10 μm/yr for the faster-growing stalagmites and <3 μm/yr for the slower growing stalagmites) may represent unresolved hiatuses and as such were excluded from the resulting paleoclimate reconstructions, following Partin et al., 2007 (see Appendix A, Supplementary Materials).

The stalagmite $\delta^{18}O$ records provide reconstructions of rainfall $\delta^{18}O$ variability at the research site, which in turn tracks the strength of regional convective activity (Moerman et al., 2013). Consistent with the tropical amount effect (Dansgaard, 1964; Rozanski et al., 1992), rainfall $\delta^{18}O$ variations measured at the site from 2006-2011 are significantly anti-correlated with regional precipitation amount, and closely track the El Niño Southern Oscillation on monthly timescales (Moerman et al., 2013). A weak semi-annual seasonal cycle in rainfall $d^{18}O$ is characterized by relative minima in June-July and November-January, and relative maxima in February-April and August-October. Such a pattern suggests that the twice-yearly passage of the Intertropical Convergence Zone (ITCZ) over the site is associated with shifts in the moisture sources and/or

trajectories that drive the observed seasonal fractionations (Moerman et al., 2013). Dripwater $\delta^{18}O$ values match rainfall $\delta^{18}O$ values averaged over the preceding 2-6 months (Cobb et al, 2007), suggesting a short residence time of dripwater $d^{18}O$ relative to our centennial-scale sampling of stalagmite $d^{18}O$. Timeseries of Buda and Mulu stalagmite $\delta^{18}O$ are highly reproducible (Partin et al., 2007; Meckler et al., 2012), strongly supporting their interpretation as rainfall $\delta^{18}O$ reconstructions and, by extension, as records of past regional convective activity.

The overlapping Borneo stalagmite $\delta^{18}O$ records show orbital-scale variability related to precessional insolation forcing and glacial-interglacial (G-I) changes (Figure 2.2). The similarity of our stalagmite $\delta^{18}O$ timeseries to indices of G-I variability greatly diminishes after removing the mean $\delta^{18}O$ of seawater due to changes in ice volume (see Appendix A, Supplementary Materials; Waelbroeck et al., 2012) from the Borneo $d^{18}O$ records (Figure 2.2, B-S7, Appendix B). After this correction, Last Glacial Maximum (LGM) $d^{18}O$ values are nearly identical to $d^{18}O$ values at ~85kybp, despite the presence of significantly larger ice sheets, cooler regional temperatures (Zhao et al., 2006; Oppo et al., 2005), and a completely exposed Sunda Shelf during the LGM. In particular, Sunda Shelf emergence has been implicated in shaping glacial western tropical Pacific hydroclimate in previous studies (Partin et al., 2007; Bush and Fairbanks, 2003; DiNezio et al., 2011). However, we find little correspondence between Borneo stalagmite $d^{18}O$ and an index of Sunda Shelf areal extent over the entire glacial cycle (Figure B-S7, Appendix B). For example, significant Borneo stalagmite d18O variations in the 70-90kybp interval bear little resemblance to reconstructed sea level changes, especially from ~76-71kybp (Cutler et al., 2003), when a large drop in sea level almost

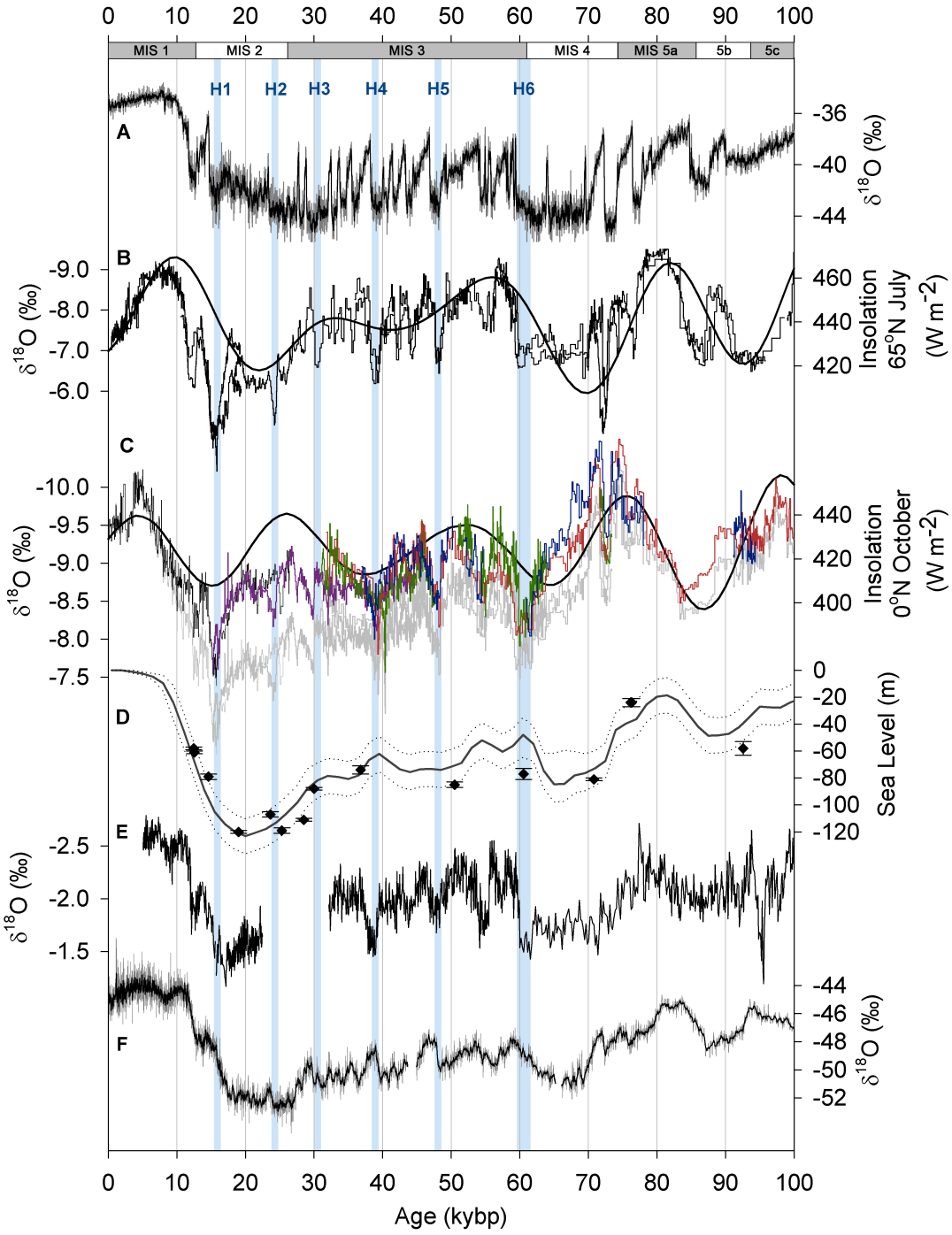
0
10
20
30
40
50
60
70
80
90
100
MIS 1
MIS 2
MIS 3
MIS 4
MIS 5a
5b
5c
H1
H2
H3
H4
H5
H6
A
B
C
D
E
F
-36
-40
-44
δ18O (‰)
-9.0
-8.0
-7.0
-6.0
δ18O (‰)
460
440
420
Insolation 65°N July (W m-2)
-10.0
-9.5
-9.0
-8.5
-8.0
-7.5
δ18O (‰)
440
420
400
Insolation 0°N October (W m-2)
0
-20
-40
-60
-80
-100
-120
Sea Level (m)
-2.5
-2.0
-1.5
δ18O (‰)
-44
-46
-48
-50
-52
δ18O (‰)
Age (kybp)

Figure 2.2. Comparison of Borneo stalagmite $\delta^{18}O$ records to climate forcings and records of paleoclimate from key regions. **(A)** Greenland NGRIP ice core $\delta^{18}O$ (grey; NGRIP, 2004) with 100yr averages (black), plotted using the GICC05modelext age model (Wolff et al., 2010). **(B)** Hulu/Sanbao cave stalagmite $\delta^{18}O$ records from China (Wang et al., 2001; 2008); where Sanbao has been offset by +1.6‰ to match Hulu), plotted with July insolation at 65°N (Berger and Loutre, 1991). **(C)** Borneo stalagmite $\delta^{18}O$ records, plotted with age models aligned and adjusted to account for changes in ice volume-related changes in global seawater $\delta^{18}O$ (see Appendix A, Supplementary Materials). Also plotted are October insolation at 0°N (black) (Berger and Loutre, 1991) and non-ice-volume-corrected versions of the Borneo stalagmite $\delta^{18}O$ records (grey). **(D)** Coral-based estimates of paleo-sea level record (Cutler et al., 2003; Bard et al., 1990a,b) (black symbols) and derived global mean sea level record *(*Waelbroeck et al, 2002) (solid line: average, dotted line: minimum and maximum). **(E)** Sulu Sea planktonic foraminifera $\delta^{18}O$ (Dannenmann et al., 2003), plotted with revised age model using updated IntCal09 calibration curve 41kybp-modern and aligning 60kybp $d^{18}O$ excursion to the Hulu/Sanbao stalagmite $d^{18}O$ records. **(F)** EPICA Dronning Maud Land (EDML) ice core $\delta^{18}O$ (grey; Barbante et al., 2006) with 7-year averages (black). Vertical blue bars indicate the timing of Heinrich events H1-H6 (Hemming et al., 2004) as recorded by the Hulu/Sanbao stalagmite $\delta^{18}O$ records (Wang et al., 2001; 2008).

doubled the size of the exposed shelf (Figure B-S7, Appendix B). As such, the new Borneo $d^{18}O$ records suggest that the cumulative influence of G-I boundary conditions, including changes in global temperature and CO_2, did not drive significant changes in rainfall $d^{18}O$ at our site. That said, the complexity of influences on rainfall $d^{18}O$ (Moerman et al., 2013) means that LGM climate may have been characterized by two or more competing influences on regional rainfall $d^{18}O$. For example, regional drying during the LGM inferred from WPWP sediment cores (De Deckker et al., 2002) and modeling studies (DiNezio et al., 2011) may have increased rainfall $d^{18}O$, while longer moisture trajectories associated with the emergence of the Sunda Shelf may have decreased rainfall $d^{18}O$.

The Borneo stalagmite $d^{18}O$ records vary in phase with insolation at the equator during boreal fall in Stage 5 and the Holocene, when precessional forcing is relatively strong (Figure 2.2c). The impact of precessional forcing on Borneo stalagmite $d^{18}O$ is weak during Stage 3, in part owing to reduced precessional amplitude during this time. Precessional forcing is also apparent in older glacial-interglacial stalagmite $\delta^{18}O$ reconstructions from Borneo (Meckler et al., 2012). Taken together, the Borneo records suggest that precession may be the dominant source of orbital-scale hydroclimate variability in the WPWP. The implied sensitivity of northern Borneo hydrology to boreal fall insolation is consistent with results from a previous modeling study (Tierney et al., 2012). Moreover, results from a long-term rainfall $d^{18}O$ monitoring program at Mulu demonstrate that mean annual rainfall $d^{18}O$ values depend, in part, on the magnitude of rainfall $d^{18}O$ enrichments during the boreal spring/fall seasons (Moerman et al., 2013). In this sense, the observed sensitivity to boreal fall insolation may represent a direct

response of mean annual rainfall $d^{18}O$ to local changes in seasonal moisture sources and trajectories. However, ENSO and the Madden-Julian Oscillations (Madden and Julian, 1972) have large impacts on modern Mulu rainfall $d^{18}O$ variability (Moerman et al., 2013), such that Borneo stalagmite $d^{18}O$ signals may represent a combination of one or more climatic influences.

The Borneo stalagmite $\delta^{18}O$ records are dominated by six millennial-scale increases in $\delta^{18}O$ that coincide with Heinrich events, inferring a decrease in regional convection during these abrupt climate changes (Figure 2.2). Indeed, a nearby Sulu Sea sediment core (Figure 2.2e) also documents increased planktonic foraminiferal $d^{18}O$ values during Heinrich events (Dannenmann et al., 2003), consistent with a reduction in regional convective activity. The dominant paradigm to explain millennial-scale tropical hydroclimate anomalies is that they are driven from the North Atlantic region, either from weakening of the Atlantic thermohaline circulation or from a dramatic albedo change due to sea ice cover, both of which drive a southward migration of the ITCZ that dries most of the northern tropics (Zhang and Delworth, 2005; Chiang and Bitz, 2005). A similar chain of events is used to describe D/O abrupt climate changes that are well-documented outside of the tropical Pacific, most notably in Chinese and Peruvian stalagmite $\delta^{18}O$ records (Wang et al., 2001, 2008; Kanner et al., 2012) and in a high-resolution ice core $\delta^{18}O$ record from the south Atlantic sector of Antarctica (Barbante et al., 2006). However, the Borneo stalagmite $d^{18}O$ records lack any coherent signature of D/O events (Figure 2.2 and Figure B-S8, Appendix B). The Borneo stalagmite $d^{18}O$ records show no consistent response to D/O events 8 and 12, the prominent D/O events that occur on the heels of Heinrich events 4 and 5 (Figure B-S8, Appendix B). Of particular note, the records show

little millennial-scale variability from ~30-40kybp across D/O events 5-8 (Figure B-S8, Appendix B). The records do bear a strong resemblance to the Chinese $d^{18}O$ records during the 50-60kybp interval, as both records contain a significant $d^{18}O$ increase at ~55kybp. This shared $d^{18}O$ enrichment may reflect the influence of an additional Heinrich event, referred to as "Heinrich 5a" in one study (Rashid and Hesse, 2003), or may indicate a regional hydrological sensitivity to the relatively prolonged D/O events that occurred during this time interval. Contrary to inferences drawn from a deglacial Borneo stalagmite $d^{18}O$ record (Partin et al., 2007), there is no evidence for a southern hemisphere influence on millennial-scale variability in Borneo hydroclimate over the last glacial cycle (Figure B-S8, Appendix B).

The unambiguous signature of Heinrich events in the Borneo stalagmite $d^{18}O$ records stands in stark contrast to the lack of consistent D/O-related signals in the records, implying a selective response of WPWP hydrology to high-latitude abrupt climate change forcing Specifically, the absence of any readily identifiable D/O signals in the Borneo $\delta^{18}O$ record represents a clear challenge to our understanding of abrupt climate change mechanisms. Indeed, the new Borneo records suggest that one of two possibilities must be true: i) if D/O events reflect a similar mechanism to Heinrich events, then they must not be strong enough to significantly affect northern Borneo hydrology, or ii) D/O events and Heinrich events are characterized by fundamentally different climate mechanisms and feedbacks.

The largest millennial-scale anomaly in the Borneo records is not a Heinrich event, but rather an abrupt increase in $\delta^{18}O$ that occurs at 73.42±0.30(2σ) kybp, coincident with a similarly large and abrupt increase in Chinese stalagmite $\delta^{18}O$ (Figure

2.2). Whether this event is associated with the Toba super-eruption, dated at 73.88±0.64(2σ) kybp) (Storey et al., 2012), and/or a prominent early abrupt climate change event visible in Greenland ice core $d^{18}O$ (Figure 2.2a) merits investigation in additional high-resolution paleoclimate records from the Indo-Pacific.

The Borneo composite records demonstrate the sensitivity of western equatorial Pacific hydrology to both high-latitude and low-latitude forcings. However, the response of northern Borneo hydroclimate to these forcings is not uniform: glacial conditions and D/O events apparently had much smaller impacts on regional hydrology than either insolation or Heinrich-related forcing. Our results imply that once the hydrological response threshold is reached, then climate feedbacks internal to the tropics may serve to amplify and prolong a given climate change event, whether the trigger originates from internal dynamics or external radiative forcing.

2.3 Acknowledgements

We thank Nele Meckler, Jud Partin, and Sue Clark (Gunung Mulu National Park) for field assistance. We also thank Guillaume Paris, Morgan Raven, Sophie Hines, and Adam Subhas for assistance in U–Th dating, and Jean Lynch-Stieglitz for providing comments on early versions of the manuscript. S.A.C, K.M.C., and J.F.A were involved in the writing and design of this study. A.A.T. and B.C. facilitated the fieldwork for this study, S.A.C, K.M.C., S.J., and J.M. collected samples, and S.A.C. analyzed them. The research was funded by NSF PECASE Award #0645291 to K.M.C., NSF AGS award #0903099 to JFA, and a NSF Graduate Research Fellowship to S.A.C. Permits for this work were granted by the Malaysian Economic Planning Unit, the Sarawak State Planning Unit, and the Sarawak Forestry Department. All data reported in this paper are

archived at NCDC (ftp://ftp.ncdc.noaa.gov/pub/data/paleo/speleothem/ pacific/gunung-mulu2013.txt).

CHAPTER 3

0-160KYBP MULTI-STALAGMITE $\delta^{18}O$ RECORD FROM NORTHERN BORNEO

3.1 Abstract

The tropical hydrologic response to variations in greenhouse gas and global temperate changes over glacial-interglacial cycles in the past is still poorly-constrained. Paleoclimate records of past variations in tropical hydrology and temperature are useful in validating the accuracy of climate model simulations in the tropics. Most paleoclimate records, however, still lack the resolution, length, and chronological control to resolve rapid variability against a background of orbital-scale variations. Here we present a large compilation of overlapping U/Th-dated Gunung Mulu stalagmite $\delta^{18}O$ records spanning 0-160 kybp, the first tropical Pacific terrestrial record to resolve multiple glacial-interglacial cycles at decadal to centennial resolution. The fact that the ice-volume corrected Mulu stalagmite $\delta^{18}O$ reconstruction does not exhibit a linear relationship with glacial boundary conditions suggests that glacial forcing is not the dominant driver of orbital-scale hydrologic variability in the western tropical Pacific. Pronounced deglacial $\delta^{18}O$ enrichments that occur prior to the major deglaciations coincident with implied drying events out of the north Atlantic are the largest signals in the 570 ky composite Mulu stalagmite $\delta^{18}O$ record. The composite Mulu $\delta^{18}O$ record varies in phase with equatorial mid-fall insolation, suggesting that precessional forcing is a strong driver of western Pacific hydroclimate on orbital timescales. This is best illustrated across Termination II, when the equatorial insolation change is large and out of phase with both pCO_2 and ice sheet decay. As a whole, the Mulu stalagmite $\delta^{18}O$ records demonstrate the

significant differences that existed between tropical sea surface temperature and tropical hydrologic response to greenhouse gas forcing on orbital timescales. The lack of a linear relationship between Mulu stalagmite $\delta^{18}O$ and CO_2 suggests that the hydrologic cycle is influenced by a variety of mechanisms, including monsoonal and El Niño Southern Oscillation dynamics. Trends in western tropical Pacific hydrology may be only weakly related to increasing anthropogenic CO_2.

3.2 Introduction

Past changes in tropical Pacific hydrology are poorly constrained by available records, making it difficult to assess the relationship between past climate forcings and hydrological response in this region. Studies show the strength of the late Pleistocene east Asian summer monsoon (EASM) strongly correlates with northern hemisphere (NH) summer precession (Wang et al., 2008; Cheng et al., 2009), while tropical sea surface temperature (SST) has strong coherence with the CO_2 record at the 41ky and 100ky periods (Lea, 2004). A tropical Pacific nitrogen isotope record has a strong linear relationship between relative nitrate utilization and seasonal insolation over the past 1 million years (Rafter and Charles, 2012). A comparison of the tropical Indo-Pacific Last Glacial Maximum (LGM) climate in six coupled general circulation models (GCM) found the tropical atmospheric overturning circulation to strengthen in all models in response to tropical SST cooling due to lower greenhouse gas levels, in agreement with the Held and Soden (2006) mechanism (DiNezio et al., 2011). Clement et al.'s (2004) modeling study found that tropical hydrology responded equally to glacial forcing and precessional forcing.

How tropical climate responds to glacial terminations, and if tropical ocean-atmosphere dynamics have any influence on the timing and structure of terminations, is still unresolved. Tropical SST leads planktonic $\delta^{18}O$ during Terminations by 3kyr, while the SST shift aligns with Antarctic temperature and atmospheric CO_2 (Lea, 2000). A high-resolution Termination 1 marine sediment core in the western Pacific suggests deep water warming preceded increases in CO_2 concentration and deglacial warming in the tropical Pacific (Stott et al., 2007). Cheng et al. (2009) found that all EASM terminations originated with a multiple-thousand year "weak monsoon interval" that began when NH summer insolation was low but increasing. The authors suggested that rising summer insolation triggers the disintegration of massive ice sheets, leading to a slowing of the Atlantic Meridional Overturning Circulation (AMOC), southern shift of the Intertropical Convergence Zone (ITCZ), rising Antarctic temperature, stronger southern hemisphere (SH) westerlies, and release of CO_2, in agreement with Denton et al. (2010). Denton et al. (2010) proposed that the critical climate threshold for an ice age termination involves (1) rising NH summer insolation and (2) large NH ice sheets prone to instabilities, with a key factor that the delivery of freshwater to the Atlantic must have persisted for long enough to raise CO_2 above a minimum level. The deglacial Borneo stalagmite $\delta^{18}O$ record reached its peak dry conditions at Heinrich event 1, not the LGM (Partin et al., 2007). The deglaciation in the Borneo record may be described as a 2-step deglaciation, with decreasing convective activity while temperatures and CO_2 rise, followed by increasing convective activity through the latter half of the deglaciation.

As a proxy for terrestrial hydroclimate variability, tropical stalagmite $\delta^{18}O$ are well-suited for the reconstruction of tropical climate's sensitivity to a variety of different

forcings. Stalagmites accrete for many thousands to tens of thousands of years, can be precisely-dated with U-Series dating (eg. Edwards et al., 1987), and provide a reconstruction of rainfall $\delta^{18}O$ variability through time closely tied to rainfall amount in the tropics (Dansgaard, 1964). The Chinese stalagmites have demonstrated the utility of generating long, overlapping stalagmite $\delta^{18}O$ records spanning many ice age cycles, but it has been difficult to extend this approach to other tropical sites. Robust reconstructions of the tropical terrestrial hydrologic cycle over many orbital cycles are lacking and are sought in order to complete a comprehensive assortment of tropical climate data proxies at the level of the ice core reconstructions.

Here we present a high-resolution 160ky multi-stalagmite $\delta^{18}O$ record to investigate the terrestrial response of west Pacific Warm Pool convection on glacial-interglacial timescales. We collected the stalagmites from Gunung Mulu National Park, where present-day rainfall and dripwater $\delta^{18}O$ reflects regional scale convection (Moerman et al., 2013, in prep). We extend two stalagmite records from previously published data (Carolin et al., 2013), and analyze five new stalagmites to create a sub-centennial scale composite record spanning two glacial terminations and seven precessional cycles. We compare our new record to other regional and global paleorecords as well as relevant climate model output in order to provide insights into the mechanisms responsible for western tropical Pacific hydroclimate variability on millennial to orbital scales.

3.3 Location and sample collection

3.3.1 Gunung Mulu National Park hydroclimate and karst

Gunung Mulu National Park on the northern side of Borneo island (4^{o}N, 115^{o}E) is an ideal field site to investigate past tropical Pacific climate variability using stalagmite proxies. An outcrop of Melanau limestone, covered with dense tropical rainforest, forms a band of hills on the eastern shale and sandstone slopes Gunung Mulu (2376 masl), and receives over 5 m of rainfall per year. The sample collection chambers are ~120-200masl. There is little seasonal variability in both temperature and rainfall amount at our site (Moerman et al., 2013) due to the present annual meridional migration of the ITCZ in the western Pacific (Xie and Arkin, 1997). Presently, the largest shift in convective activity occurs during El Niño Southern Oscillation (ENSO) extremes. During an El Niño event, warm SSTs in the central and eastern Pacific drive convective activity eastward, leading to drier conditions over the Warm Pool. During a La Niña event, convection strengthens over Borneo (eg. Cobb et al., 2007).

A 5-year daily rainfall collection study in Mulu shows present-day rainfall $\delta^{18}O$ variability to reflect regional precipitation amount with significant basin-wide correlations at monthly and longer timescales (Moerman et al., 2013), in agreement with isotope-enabled climate model simulations (Lewis et al., 2010). Dripwater $\delta^{18}O$ values match rainfall $\delta^{18}O$ values averaged over the preceding 3-9 months (Moerman et al, in prep), suggesting a short residence time of dripwater $\delta^{18}O$ relative to our centennial-scale sampling of stalagmite $\delta^{18}O$.

3.3.2 Sample Collection

Stalagmites have been collected from Gunung Mulu National Park (4°6'N, 114°53'E) over multiple expedition trips: 2003-2006 (Gunung Buda limestone) and 2005-2012 (Gunung Mulu limestone). After preliminary test sampling, broken fallen stalagmites were selected from the cave floors with targeting based on common criteria used for uranium-series dating methods: measurable quantity of uranium, minimal daughter-nuclide present at the time of deposition or introduced through diagenesis, and no post-deposition migration of radionuclides. Samples were visually inspected before collection for permeability, evidence of dissolution or secondary calcite precipitation, and extent of detrital contamination.

Stalagmites analyzed in this study include FC12-12, FC12-14, and FC12-15 from Fairy City chamber, within 1 km of Secret Chamber stalagmites published in Carolin et al. (2013), and WR12-01 and WR12-12 from Whiterock Cave. Cave chamber location maps and descriptions provided in Supplementary Materials (Appendix C).

3.4. Analytical methods

3.4.1 Stable oxygen isotope measurements

Oxygen isotopic analyses were conducted on 70-100 μg sample powders drilled at 0.2-1mm increments, depending on individual stalagmite growth rates, along the central growth axis of the stalagmites using a 1.6 mm drill bit. The $\delta^{18}O$ ratios were analyzed on either a Finnigan 253 or a Delta V Plus equipped with Kiel devices at Georgia Institute of Technology (long-term reproducibility of less than ±0.07‰ (1σ)). Small sections of the stalagmite were run twice on both instruments to confirm calibration and reproducibility.

Two in-house aragonite powder oxygen/carbon isotope standards bracket every 10-12 samples to monitor instrument drift. All $\delta^{18}O$ data are reported with respect to VPDB.

3.4.2 U-Series isotope measurement and age calculation

Age models were constructed for each stalagmite using U-series disequilibrium (^{238}U-^{234}U-^{230}Th) measurements with the isotopic compositions of the U and Th fractions determined using a Finnigan Neptune MC-ICPMS at California Institute of Technology. Calcite powder (150-400mg, depending on U concentration) for each U-series sample was drilled along visual growth bands. U-series chemistry and MC-ICP-MS data collection methods follow those described in Partin et al., 2007. At least three spiked procedural blanks were included with each batch of U-series samples. The standard deviation (2σ) for the population of procedural blank values within a batch is added in quadrature with the internal instrument error standard deviation (2σ). The half-lives of ^{234}U and ^{230}Th are provided in Cheng et al (2013). Measured concentrations and activity ratios are reported in Table C-S1 (Appendix C) for all samples. U-234 samples ranged from 1e9 - 2.7e10 total atoms with average procedural blanks <1e6 atoms, and Th-230 samples 1e8 - 4e9 total atoms with average procedural blanks <1e5 atoms.

The reported ages and their 2σ uncertainties (see Table C-S1, Appendix C) were estimated using a Monte Carlo simulation that accounts for the errors in all isotope ratios and the uncertainty in the initial $^{230}Th/^{232}Th$ ratio (see Section 3.4.3). If the relative age error is greater than 2% of the calculated age, the date was not used in constructing a stalagmite's age model. Also, if a repeat dating sample was drilled directly above or below a previously analyzed sample, the date with the smaller age error is used in constructing the age model.

3.4.3 Isochrons and ^{230}Th-Corrected Age Model

Isochrons were used to correct for the non-carbonate invasive ^{238}U, ^{234}U, and ^{230}Th isotopes. Three or more co-precipitated samples with variable (^{238}U/^{232}Th) were analyzed on multiple stalagmites from multiple cave chambers for a total of 25 isochron-derived initial (^{230}Th/^{232}Th) ratios (see Supplementary Materials, Appendix C). A large scatter of ^{230}Th/^{232}Th values in our individual isochrons is an indication that more than one source of initial ^{230}Th exists in our system and we therefore take a conservative approach (i.e. larger error bars) in estimating a detrital ^{230}Th/^{232}Th ratio. We assign detrital atomic ^{230}Th/^{232}Th ratios as follows (previously published in Partin et al. (2007) and Carolin et al. (2013)): SSC01 = 127 ± 20 ppm; SCH02 = 59 ± 13 ppm; BA04 = 55 ± 5 ppm; BA02 = 56 ± 11 ppm; SC03 and SC02 = 111 ± 41 ppm (2σ errors). Fairy City stalagmites are assigned a detrital atomic ^{230}Th/^{232}Th ratio = 78 ± 42 ppm (2σ errors) (see Supplementary Materials, Appendix C).

Due to high (^{238}U/^{232}Th) activity ratios, Whiterock stalagmite isochrons could not to be used confidently to calculate an initial detrital ^{230}Th/^{232}Th ratio. To circumvent this problem, we compared plots of each of the Whiterock stalagmite δ^{18}O timeseries with age models constructed from various initial (^{230}Th/^{232}Th) ratios. Figure 3.1 compares the Termination 2 WR12-01 (top) and WR12-12 (bottom) δ^{18}O records using initial (^{230}Th/^{232}Th) equal to 60 ppm (red) and 4 ppm (black). If the two records overlapped, we concluded that detrital Th does not have a significant effect on the age model during that period and that the overlapping records highlight robust age model control sections. Experimenting with different initial ^{230}Th/^{232}Th ratios and comparing the δ^{18}O timeseries

amongst other overlapping U-series dated Mulu stalagmite records, we assigned the Whiterock initial $^{230}Th/^{232}Th$ to be 60 ± 20 ppm.

The age models for the stalagmites in this study were constructed using the StalAge algorithm (Scholz and Hoffman, 2011) (see Supplemental Materials, Appendix C). Age-depth profiles for FC12-12, FC12-14, FC12-15, WR12-01, WR12-12, and new lower section SC03 are provided in Figure C-S4 through C-S10, Appendix C. Secret and Whiterock stalagmites have the greatest U concentration (100-200ppb and 200-500ppb, respectively) and the least detrital contamination, and therefore are associated with the most robust age models (0.4-1.0% (2σ) relative age error, and ±520 years (2σ) at Termination II). FC12-14 and FC12-15 stalagmites have low U concentration (40-80ppb) and larger detrital contamination, resulting in significantly larger age errors (0.7-4.2% (2σ) relative).

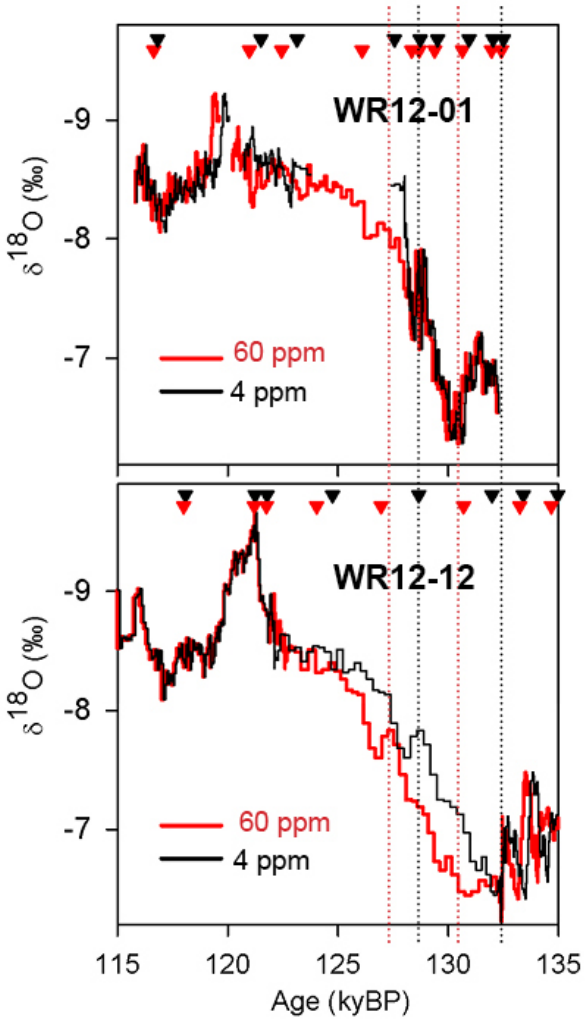

Figure 3.1. (top) WR12-01 and (bottom) WR12-12 $\delta^{18}O$ timeseries plotted against 2 age models, initial $^{230}Th/^{232}Th$ = 4ppm (black) and initial $^{230}Th/^{232}Th$ = X ppm (red). U-Th ages plotted as triangles at top of both plots. Vertical dotted lines indicate peaks in the respective $\delta^{18}O$ timeseries. Note areas where the black and red curves overlap for a given stalagmite record.

3.5. Results

3.5.1 Composite 160-ky Mulu $\delta^{18}O$ record construction

This study presents five new Mulu stalagmite $\delta^{18}O$ records to extend the previously published Mulu records to 160kybp. They are as follows: WR12-01 (115.7-153.8kybp), WR12-12 (113.9-144.4kybp), FC12-12 (109.0-121.5kybp), FC12-14 (73.8-87.3kybp and 129.4-161.6kybp), and FC12-15 (139.9-164.0kybp). We also extend previously published stalagmites SC03 (103.5-119.5kybp) and SC02 (94.1-99.0kybp). Figure 3.2 shows the individual stalagmite $\delta^{18}O$ records in separate panels with their associated U-series sample ages, along with the combined composite 0-160kybp Mulu $\delta^{18}O$ record. To overlap new Mulu stalagmite $\delta^{18}O$ records with previously published records, individual stalagmite $\delta^{18}O$ values were offset by the following amounts: WR12-01 and WR12-12, +0.3‰; FC12-12 and FC12-14, +0.35‰; FC12-15, +0.6‰.

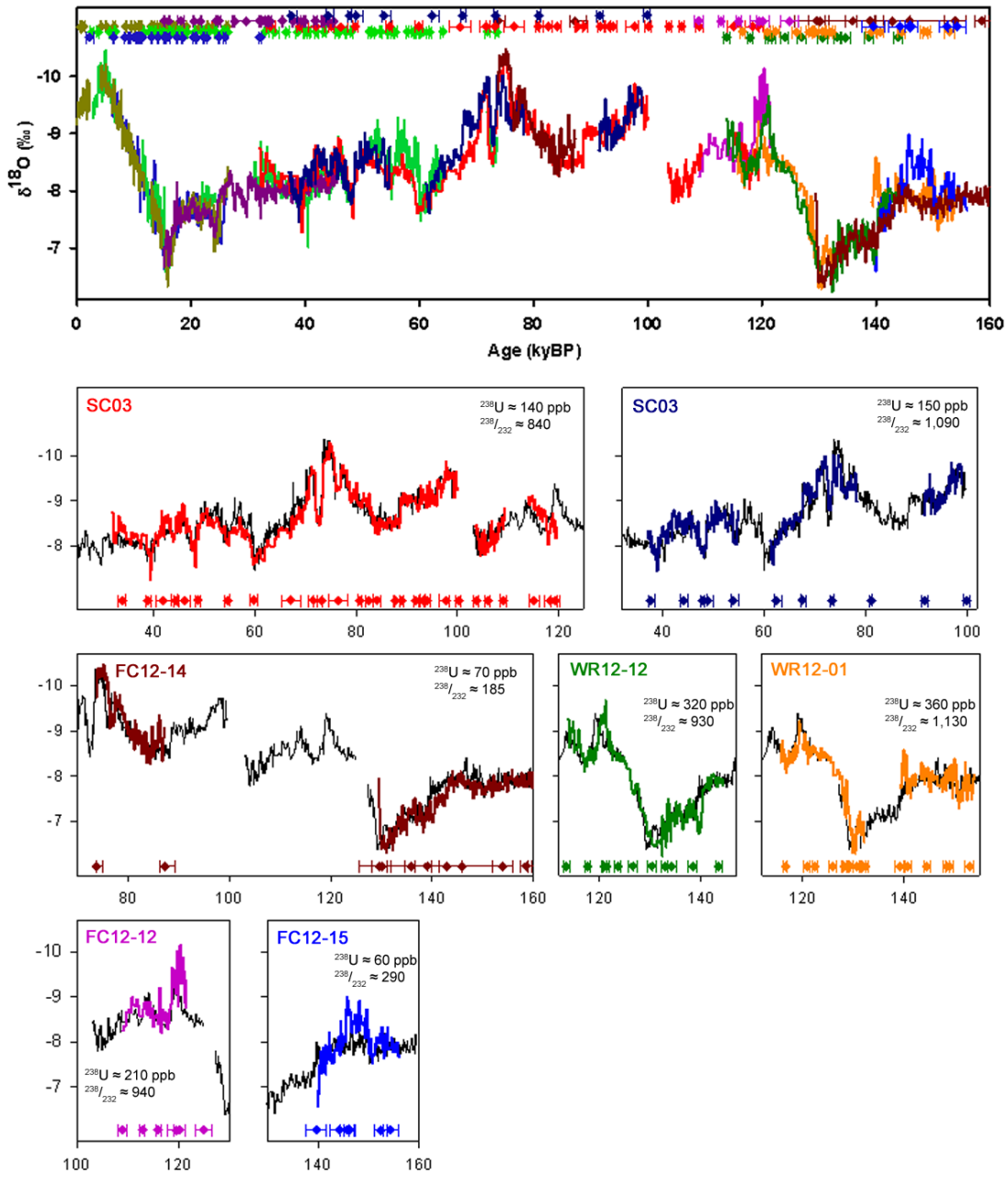

Figure 3.2. Comparison of overlapping Mulu stalagmite $\delta^{18}O$ records using Stalage age models (see text): SC03 (red), SC02 (navy), FC12-14 (dark red), WR12-12 (dark green), WR12-01 (orange), FC12-12 (pink), FC12-15 (royal blue) plotted with previously published stalagmite $\delta^{18}O$ data from our site (Partin et al., 2007; Carolin et al., 2013). WR12-01 and WR12-12 have been offset +0.3‰; FC12-12 and FC12-14, +0.35‰; FC12-15, +0.6‰ to match the absolute value of SCH02, consistent with the prior use of SCH02 as a benchmark for the deglacial/ Holocene Borneo records (Partin et al., 2007). U–Th-based age samples plotted in corresponding colors, shown with 2σ uncertainty limits.

To create a continuous, evenly-spaced composite record, averages of all measured Mulu stalagmites' $\delta^{18}O$ were calculated using 100-yr boxcar bins. Any gap in the composite record was filled by linearly interpolating between filled boxcar bins. An evenly-spaced ice-volume corrected composite record was created following the procedure in Carolin et al. (2013). The two composite records are shown in Figure 3.3.

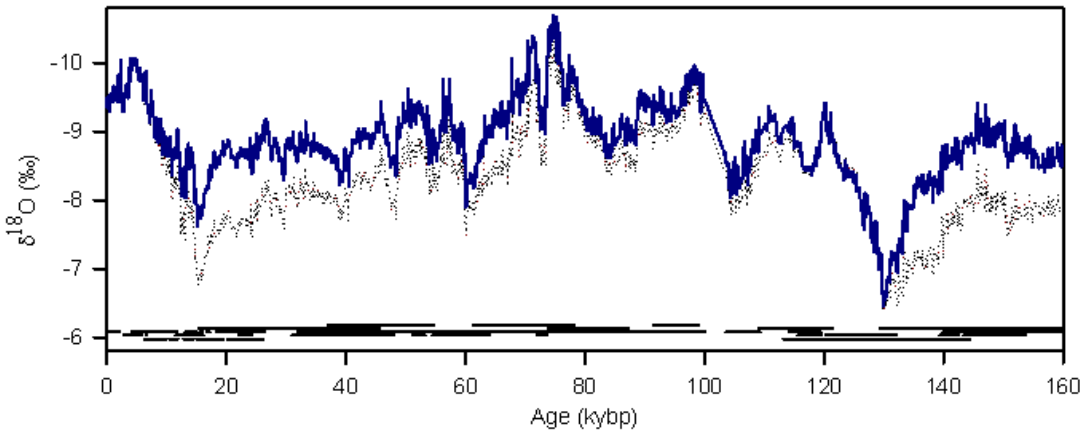

Figure 3.3. (dotted grey) Composite Mulu stalagmite $\delta^{18}O$ record, created by averaging all measured Mulu stalagmites' $\delta^{18}O$ in 100-yr intervals using 100-yr boxcar bins. Any gap in the composite record was filled by linearly interpolating between filled boxcar bins. (solid blue) Same as above, but ice-volume corrected (see text). Black bars below indicate how many overlapping stalagmite records are used to create the composite at each timestep.

3.5.2 Features of the 160-ky Mulu $\delta^{18}O$ record

3.5.2.1 Glacial-interglacial variability

The overlapping stalagmite records allow for absolute $\delta^{18}O$ comparisons between different Marine Isotope Stages. Stage 5a (~74-85 kybp) is the most depleted period of the 160ky record, ~4‰ more depleted than the greatest enrichment at H11 (130 kybp), and ~1‰ more depleted than average 0-1 kybp (both original and ice-volume corrected). The last interglacial (~115-131 kybp), alternatively, is ~0.5‰ more enriched than present day, and only slightly more depleted than the LGM (~20-22kybp), after ice-volume corrections.

With the addition of the new records, the Borneo cave $\delta^{18}O$ records resolve tropical hydrologic variations across the last five glacial-interglacial cycles. The 100-160ky Mulu stalagmite $\delta^{18}O$ record addition (this study) plotted with all other published Mulu stalagmite $\delta^{18}O$ records (Partin et al., 2007; Meckler et al., 2012; Carolin et al., 2013) is provided in Figure 3.4 to form an extended tropical hydrologic strength reconstruction that resolves multiple glacial-interglacial cycles with five glacial terminations (I-V). The stalagmite $\delta^{18}O$ records in Figure 3.4D are not ice-volume corrected due to the dating uncertainty in the Meckler et al., 2012 record (210-570 kybp) and the uncertainty in older global mean $\delta^{18}O_{sw}$ estimations (in both age and $\delta^{18}O$). The full Mulu stalagmite $\delta^{18}O$ reconstruction shows some evidence of a glacial-interglacial 100-ky cycle.

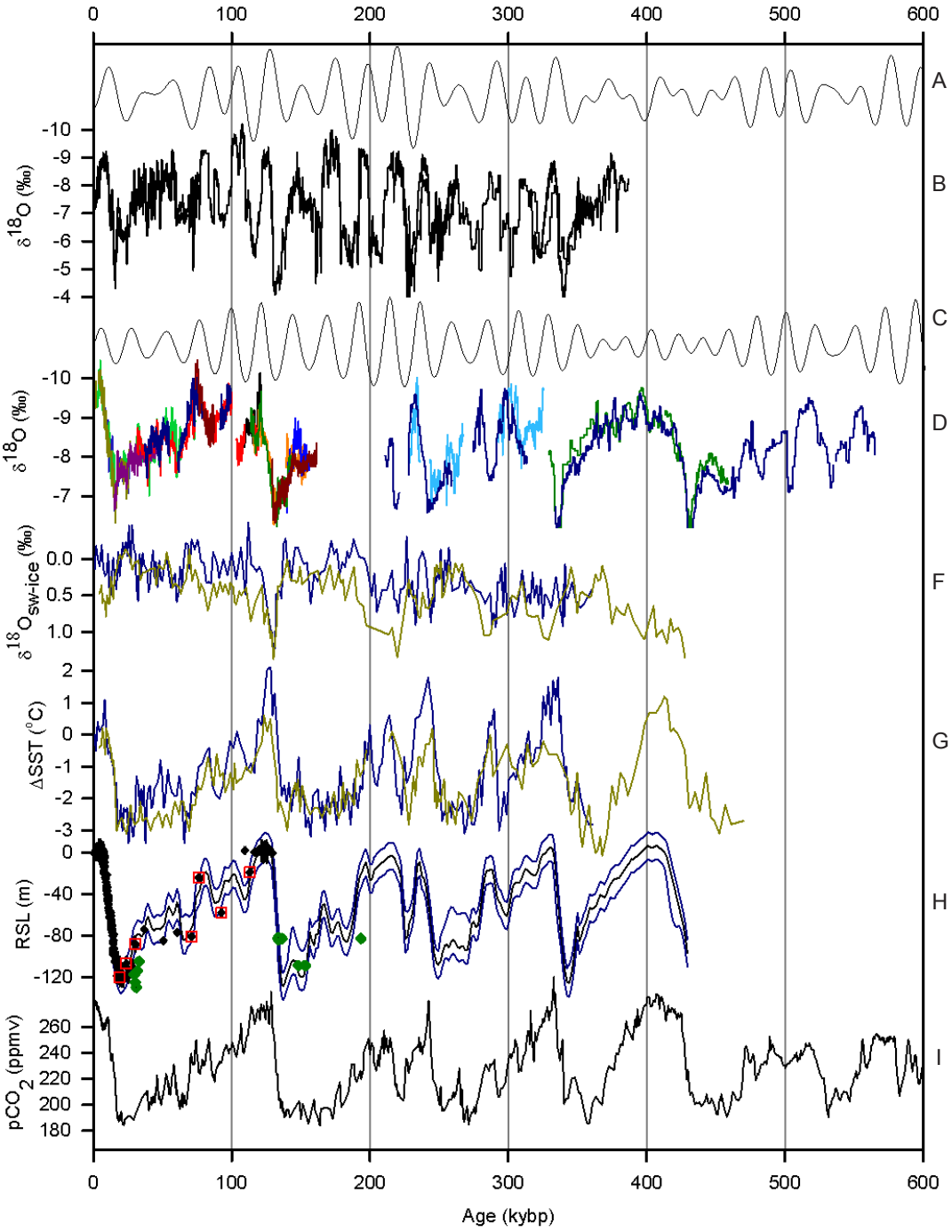
0
100
200
300
400
500
600
A
B
C
D
F
G
H
I
δ18O (‰)
-10
-9
-8
-7
-6
-5
-4
δ18O (‰)
-10
-9
-8
-7
δ18Osw-ice (‰)
0.0
0.5
1.0
2
ΔSST (°C)
2
1
0
-1
-2
-3
RSL (m)
0
-40
-80
-120
pCO2 (ppmv)
260
240
220
200
180
0
100
200
300
400
500
600
Age (kybp)

Figure 3.4. (A) Insolation forcing (W/m2) at 65N boreal summer (Berger, 1978). (B) Hulu, Dongge, Sanbao, and Linzhu stalagmite $\delta^{18}O$ records on published age model (Wang et al., 2001; Dykoski, et al., 2005; Wang et al., 2008; Cheng et al., 2009). (C) Insolation forcing (W/m2) at 0N October 15 (Berger, 1978). (D) Mulu stalagmite $\delta^{18}O$ records (Partin et al., 2007; Carolin et al., 2013, in prep; Meckler et al., 2012). (E) Marine sediment $\delta^{18}O_{SW}$ and (F) Mg/Ca SST reconstructions from WEP site ODP 806b (dark yellow) (Lea et al., 2000) and EEP site TR163-19 (light blue) (Lea et al., 2000) on original published age model. (H) Coral relative sea level estimates (same citations as Figure 6) plotted on top of Waelbroeck et al. (2002) sea level derivation from benthic foraminifera compilation. (I) EDC (Monnin et al., 2001; Siegenthaler et al., 2005) and Vostok (Petit et al., 1999) CO_2 records on the EDC3 timescale (Parrenin 2007), and composite EDML and Talos Dome CO_2 record on the EDML1_Sc4 gas age scale (Bereiter et al. 2012).

After ice volume effects are removed, however, there is little evidence that glacial boundary conditions affected Mulu stalagmite $\delta^{18}O$. In general, Mulu stalagmite $\delta^{18}O$ variability reflects changes in seawater $\delta^{18}O$ (whether related to ice volume or regional hydrological effects), temperature, and changes in rainfall $\delta^{18}O$. Therefore, we infer that either i) none of these various contributions changed appreciably during glacial times, or 2) that the changes in these parameters may have cancelled each other out. Assuming calcite precipitation under equilibrium conditions (see Supplementary Materials, Appendix C), the remaining variability in rainwater isotopes ($\delta^{18}O_{rw}$) is due to either variability in ocean source $\delta^{18}O_{sw}$, rainwater trajectory from source to site, and/or changes in seasonality effects.

3.5.2.2 Glacial terminations

We compare our extended Mulu stalagmite $\delta^{18}O$ record to other well-dated records from Termination I and II in order to place the unique features that we see in the Mulu records in a global climate context. A notable peak in the Mulu $\delta^{18}O$ record is at 130.6 ± 0.6 (2σ) kybp near the Stage 6-5e transition (Figure 3.5). Partin et al. (2007) found the significant Mulu $\delta^{18}O$ peak at 16.3 ± 0.3 ky to correspond within error to the $\delta^{18}O$ peak in the Hulu cave records attributed to Heinrich event 1 (H1) (Wang et al., 2001). As such, we propose that the significant 640 yr Mulu $\delta^{18}O$ peak beginning at 130.6 ± 0.6 (2σ) kybp corresponds to Heinrich event 11 (H11), in agreement with the alignment of north Atlantic records in Cheng et al. (2006). Prior to the H11 maximum in stalagmite $\delta^{18}O$, Mulu stalagmite $\delta^{18}O$ plateaus from ~136-140kybp, similar to the plateau in variability shown in the Mulu record at the LGM, before it gradually trends to

the most enriched values at H11. Finally, in both terminations the Mulu stalagmite $\delta^{18}O$ trends into and out of the Heinrich-related maximum smoothly, with no sign of subsequent reversals during the deglaciation.

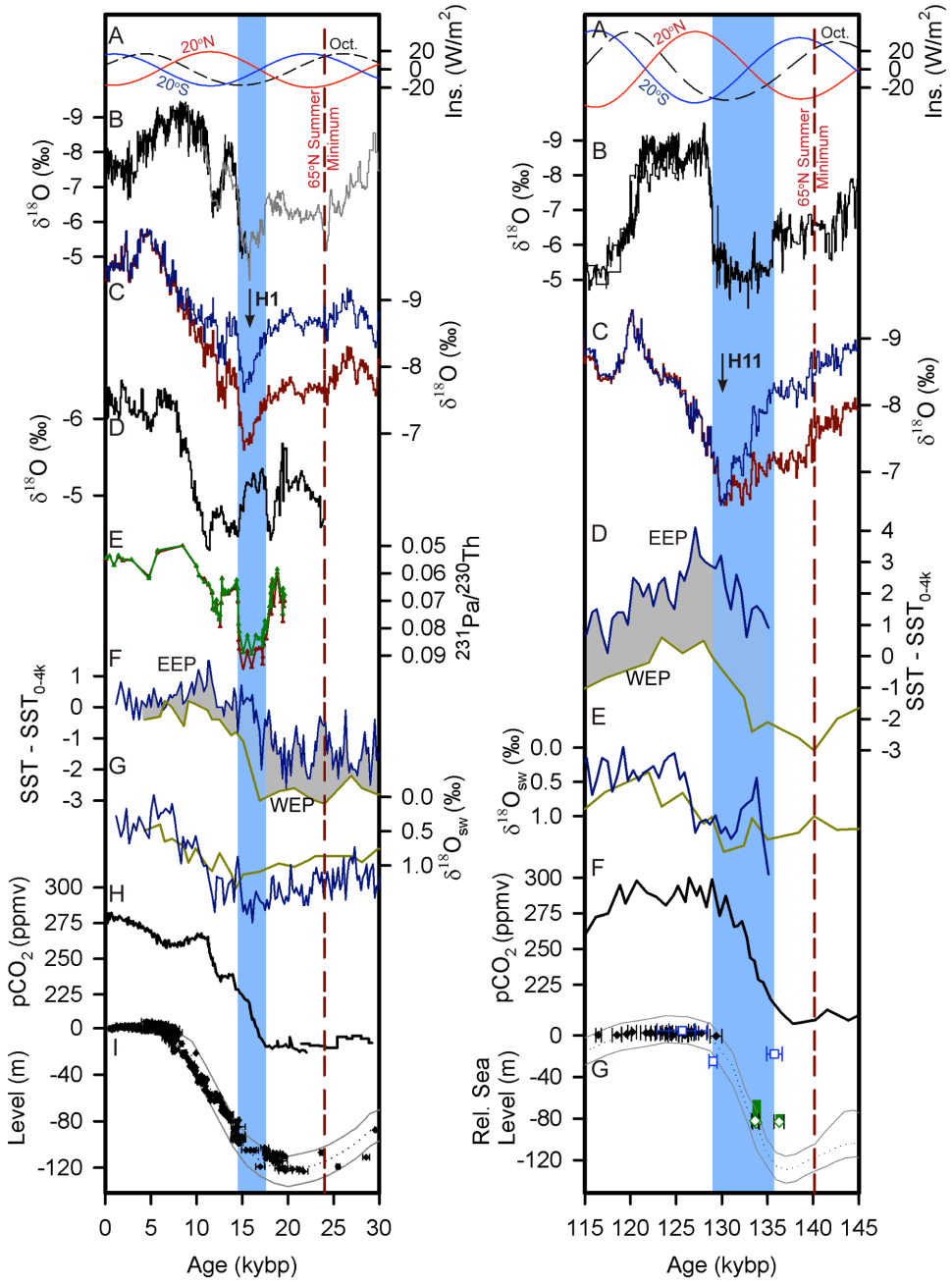
A
20°N
20°S
Oct.
Ins. (W/m2)
65°N Summer Minimum
B
δ18O (‰)
C
H1
H11
D
EEP
WEP
E
231Pa/230Th
F
SST - SST0-4k
G
δ18Osw (‰)
H
pCO2 (ppmv)
I
Level (m)
Rel. Sea Level (m)
Age (kybp)

Figure 3.5. **(left)** Comparison of records over Termination 1. (A) Insolation forcing (W/m2) at 20N boreal summer (red), 20S austral summer (blue), and 0N October 15 (Berger 1978). (B) Hulu (grey) and Dongge (black) $\delta^{18}O$ stalagmite records on published age model (Wang 2001; Dykoski 2005). (C) Composite Mulu stalagmite $\delta^{18}O$ records, original published (red) and ice-volume corrected (blue) (Partin et al, 2007; Carolin 2013) averaged in 100yr boxcar bins. (D) Liang Luar (Flores) stalagmite $\delta^{18}O$ records on published age model (Griffiths 2009). (E) $^{231}Pa/^{230}Th$ in marine sediment core GGC5 near the Bermuda Rise, North Atlantic (McManus 2004). (F) Marine sediment Mg/Ca SST reconstructions and (G) $\delta^{18}O_{SW}$ reconstructions from WEP site ODP 806b (dark yellow) (Lea et al., 2000) and EEP site TR163-22 (dark blue) (Lea et al., 2006) on published age model. (H) EDC CO_2 records (black) (Monnin et al., 2001) on the EDC3 timescale (Parrenin et al., 2007) and Taylor Dome CO_2 records (black) (Indermühle et al., 1999) on the st9810 timescale (Steig et al., 2000). (I) Coral relative sea level estimates (Bard, 1996, 1990; Yokoyama 2000; Edwards 1993; Cutler 2003; Fleming et al., 1998; Peltier and Fairbanks, 2006) plotted on top of Waelbroeck (2002) sea level derivation from benthic foraminifera compilation. **(right)** Comparison of records over Termination 2. (A) same as left. (B) Dongge $\delta^{18}O$ stalagmite records on published age model (Kelly et al., 2006). (C) Composite Mulu stalagmite $\delta^{18}O$ records, original (red) and ice-volume corrected (blue) (Carolin et al., in prep). (D) Marine sediment Mg/Ca SST reconstructions and (E) $\delta^{18}O_{SW}$ reconstructions from WEP site ODP 806b (dark yellow) (Lea et al., 2000) and EEP site TR163-22 (dark blue) (Lea et al., et al., 2006) on published age model. (F) Dome Fuji wet extraction CO_2 concentration on DFO-2006 timescale (Kawamura et al., 2007). (G) Coral relative sea level estimates (Stirling et al., 1995, 1998; Thomas et al., 2009; Gallup et al., 2002) plotted on top of the Waelbroeck et al. (2002) sea level derivation from benthic foraminifera compilation. Blue shading indicates the north Atlantic stadial, interpreted as the enriched Chinese $\delta^{18}O$ event (eg. Wang et al., 2001, Cheng et al., 2009). The vertical dashed line marks the initial increase in NH summer insolation (Berger, 1978). Arrows point to the maximum deglaciation peaks in Mulu stalagmite $\delta^{18}O$, which we interpret as coincident with Heinrich events H1 and H11.

A notable difference between glacial Terminations I and II is the timing of the Heinrich event with respect to the rise in atmospheric CO_2 and sea level. During Termination I, H1 occurs near the midpoint of the deglacial rise in CO_2, temperature, and sea level (eg. Denton et al., 2010), while the Mulu 130.6 ± 0.6 (2σ) kybp $\delta^{18}O$ peak suggests the maximum iceberg discharge event occurs nearer to the end of the rise in CO_2. The ice-volume corrected Mulu records are 3‰ greater than present day at H11, while only 2‰ greater at Heinrich 1, with a portion of the difference due to ice-volume correction: ~0.9‰ at the H1 peak and only ~0.2‰ at the H11 peak. In comparison, Mulu stalagmite $\delta^{18}O$ enrichment anomalies associated with glacial Stage 3 Heinrich events 2-6 are <1‰. At H1, WPWP SSTs were a few degrees cooler than present, while at the H11 peak WPWP SST had already risen to present-day values (Lea et al., 2000; 2006; Visser et al., 2003). With a temperature-dependent calcite fractionation of -0.22 ‰/°C (Epstein et al., 1953) the difference in Mulu precipitation $\delta^{18}O$ from today (ice volume effects removed) is roughly twice as enriched at H11 than H1.

3.5.2.3 Precessional control on Mulu $\delta^{18}O$

Previous studies have established that precessional insolation forcing exerts a primary control on Mulu stalagmite $\delta^{18}O$ (Meckler et al., 2012; Carolin et al., 2013), and our new records are likewise coherent with precession. Mulu stalagmite $\delta^{18}O$ is in phase with equatorial fall insolation, and China stalagmite $\delta^{18}O$ is in phase with NH summer insolation (Wang et al., 2001) (Figure 3.6). Spectral analysis confirms that the Chinese stalagmite $\delta^{18}O$ records are more heavily influenced by precession than the Mulu $\delta^{18}O$ records (see Supplementary Materials, Appendix C), but the Mulu records may contain

an influence from obliquity that is not present in the Chinese stalagmite $\delta^{18}O$ records. The Mulu stalagmite $\delta^{18}O$ record has a small 41ky peak at the obliquity frequency that is above red noise but below the red noise 95% confidence interval (see Supplementary Materials, Appendix C) (Figure 3.6).

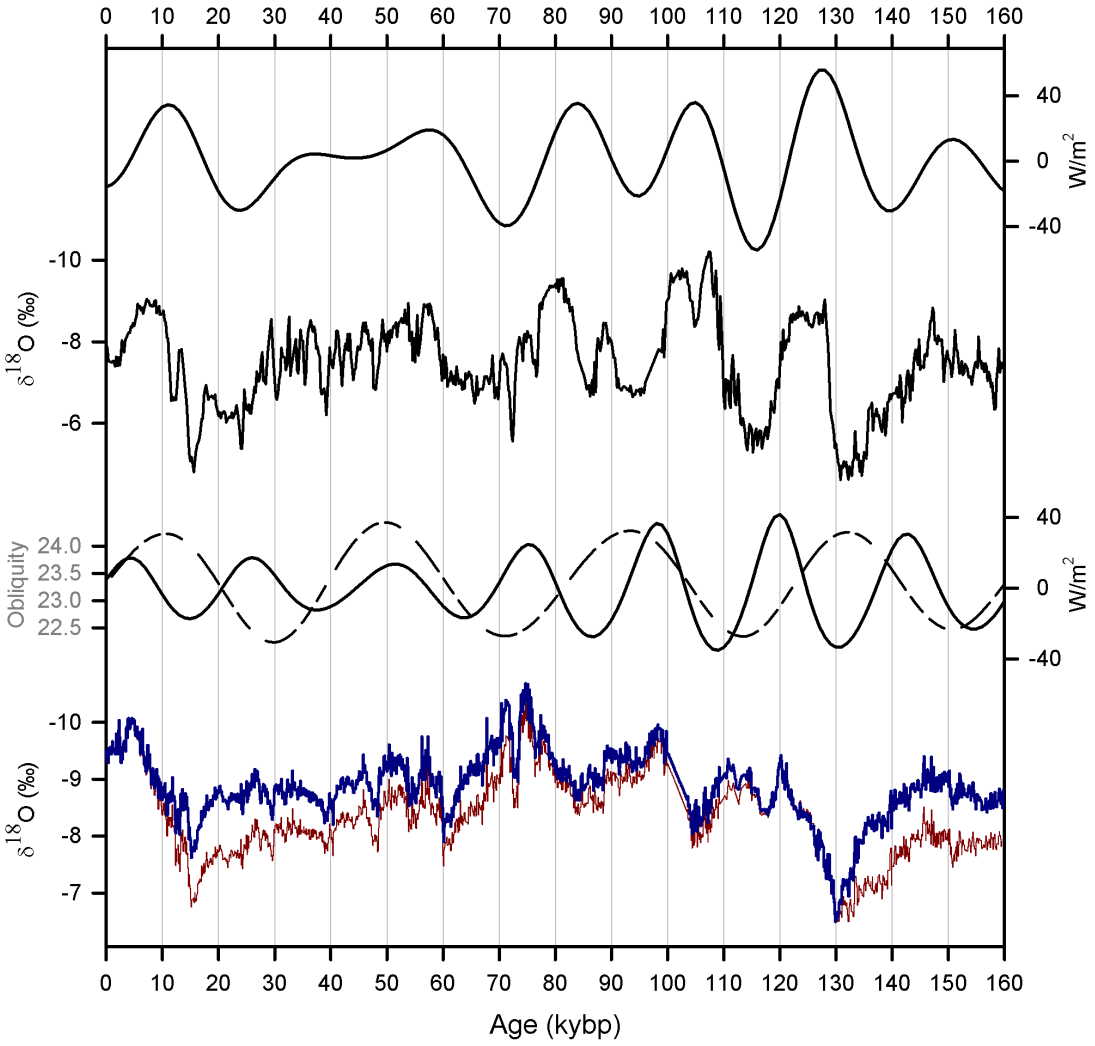

Figure 3.6. (A) Insolation forcing (W/m2) at 65^{o}N boreal summer (Berger, 1978). (B) Composite Hulu, Dongge, and Sanbao stalagmite $\delta^{18}O$ records (Wang et al., 2001; Dykoski et al., 2005; Kelly et al., 2006; Wang et al., 2008) constructed by averaging in 200ky boxcar bins. (C) Obliquity variability and insolation forcing (W/m^2) at 0^{o}N October 15 (Berger, 1978). (D) Composite Mulu stalagmite $\delta^{18}O$ records, original (red) and ice-volume corrected (blue) (Partin et al., 2007; Carolin et al., 2013, in prep) averaged in 100yr boxcar bins.

3.6. Discussion

3.6.1 Tropical hydrologic response to glacial-interglacial variations

The full Mulu stalagmite $\delta^{18}O$ reconstruction shows no evidence of a glacial-interglacial 100-ky cycle, similar to the Chinese monsoon record and opposite to the west Pacific SST sawtooth pattern (Lea et al., 2000) (Figure 3.4). This observation is in agreement with climate model simulations suggesting annual mean temperature response to glacial forcing to be an order of magnitude greater than the temperature response to precessional forcing, while the response of the hydrologic cycle to both forcings is comparable (Clement et al., 2004). We conclude that over the span of our record orbital forcing strength is similar to or greater than glacial-interglacial forcing.

Sunda shelf exposure from lowered sea levels suggests potential alterations in the rainfall $\delta^{18}O$-to-rainfall amount relationship, possibly resulting from changes in source water and/or source trajectory. Other nearby stalagmite hydrologic studies in Flores, Indonesia ($8^{o}S$, $120^{o}E$) suggest increased convection coupled to the inundation of the Sunda shelf (Griffiths et al., 2013; Ayliffe et al., 2013). Further, analysis of tropical LGM model simulations suggests that the mechanisms responsible for strengthening the tropical overturning circulation in response to tropical glacial cooling also weakens vertical motion over the exposed Sunda shelf land area (DiNezio et al., 2011; DiNezio and Tierney, 2013). Carolin et al. (2013), however, found no isolated evidence of a first-order influence of Sunda shelf areal exposure on local rainfall $\delta^{18}O$ in the 0-100ky Mulu stalagmite $\delta^{18}O$ record. Signals coincident with Meltwater Pulse 1A (~14.0 kybp, ~20m rise to 80 mbsl) and 1B (~11.3 kybp, ~12m rise to 45 mbsl) (Fairbanks, 1989; Reimer et al., 2013) are also not distinct in the Mulu deglaciation record (Partin et al., 2007). We

therefore note that as of yet there is no proxy evidence directly linking Mulu rainfall $\delta^{18}O$ to shelf exposure.

3.6.2 Glacial terminations: western tropical hydrology

Deglacial $\delta^{18}O$ enrichments coincident with north Atlantic millennial-scale stadials are the largest signal throughout the entire 570 ky Mulu composite stalagmite record, suggesting that the combination of forcings responsible for the large Heinrich enrichments are particular to western tropical Pacific hydrology. The large deglacial excursions are not mirrored in either the long EASM stalagmite records or the tropical SST reconstructions (Figure 3.4).

Mulu stalagmite $\delta^{18}O$ records provide the opportunity to compare two robustly-dated terrestrial deglaciation records of the Warm Pool hydrologic cycle. There are notable similarities in both Termination I and II records. Warm Pool convection (Partin et al., 2007; this study) is not strongly affected by the abrupt shifts into and out of stadial conditions HS1 (14.6-17.4kybp) and HS11 (129.0-135.5kybp) (ages chosen from Wang et al., 2001; Kelly et al., 2005). We attribute this trend into and out of the Heinrich events to two complementary forcings: (1) AMOC strength and north or south shifting of the ITCZ to cause a maximum dry event at the peak Heinrich event (eg. Zhang and Delworth, 2005), and (2) equatorial fall insolation, which reaches a minimum coincident with the Heinrich event to force the gradual trend in and out of the Heinrich event (Berger, 1978). Carolin et al. (2013) found no evidence of polar SH influence on Borneo convection during MIS 2-4, and indeed Termination II Antarctic temperatures rise several thousand years prior to the Mulu record's H11 $\delta^{18}O$ maximum (Kawamura et al., 2007).

Based on the timing of Mulu stalagmite $\delta^{18}O$ variability to north Atlantic climate forcings during Termination I, Partin et al. (2007) suggested climatic feedbacks in the tropical Pacific may have played a part in driving the variability of the AMOC across H1. Per this study's Termination record comparison, we suggest that Mulu stalagmite $\delta^{18}O$ is strongly driven by a mechanism(s) relatable to equatorial mid-fall insolation (see Section 3.6.3) during Terminations, which is the primary cause of the more gradual trends into and out of deglaciation Heinrich events.

Our records suggest that reductions in Warm Pool convective activity at H11 were approximately twice as large as those during H1. Lack of additional hydrologic records north and south of the equator that span Termination II makes it difficult to resolve what is forcing twice as large drier conditions at the end of Heinrich stadial 11 versus Heinrich event 1. Records from the Ontong Java Plateau (0^oN, 159^oE) and just north of the Galapagos islands (0^oN, 92^oW) indicate the SST gradient between western equatorial Pacific (WEP) and eastern equatorial Pacific (EEP) sites is ~2-3^{o}C less than present day over Termination II and ~0-1^{o}C less over Termination 1 (Lea et al., 2000; 2006) (Figure 3.5), possibly suggesting an increase in ENSO variance weighted toward a modern Pacific El Niño-like state during Termination II. Using an extrapolated timeseries of collected Mulu dripwater $\delta^{18}O$, Moerman et al. (2014, in prep) suggests an increase in ENSO variance similar in magnitude to the maximum variance observed in 20th century measurements and Holocene proxy data would likely enrich Mulu stalagmite $\delta^{18}O$ <1‰ when sampled at 30-yr-average resolution. Equatorial mid-fall insolation was at a local minimum of 411 W/m^2 (17 W/m^2 less than mean) during Heinrich 1 compared to 395 W/m^2 (33 W/m^2 less than mean) during Heinrich 11. Equatorial mid-fall insolation

strength is in phase with the Mulu $\delta^{18}O$ 0-160ky record and the related fall insolation mechanism may be a dominant driver of west Pacific hydrology. We therefore propose the combination of low equatorial mid-fall insolation plus a large southward shift in ITCZ as the primary cause of the H11 3‰ enrichment, with a possible smaller fraction of enrichment resulting from increased ENSO variance.

We note that Esat et al. (1999) found corals within Aladdin's Cave on the terraces of Huon Peninsula in PNG to imply a drop in sea level of 60-80 m at 130 ± 2 kyr, exactly coincident with our peak in stalagmite $\delta^{18}O$ at H11. Assuming +1.0 ± 0.1‰/125m sea level drop (eg. Schrag et al., 2002), 80 m ≈ +0.65‰, which would adjust the SL-corrected Mulu records to +2.35‰ more enriched than today, excluding any temperature differences, which is more equivalent to the H1 enrichment (~+2‰).

3.6.3 Precession and seasonality forcing

The Mulu hydrologic record's strong coherence and minimal phase lag with the fall equatorial precessional cycle (see Supplementary Materials, Appendix C) demonstrates greater fall insolation on orbital timescales (Figure 3.6) in general correspondence to wetter, "La Niña-like", conditions in Mulu. The Mulu record is in agreement with Clement et al. (1999): late summer/early fall insolation strength variability (a tropical zonally uniform forcing) produces a more zonally asymmetric response, El Niño or La Niña-like, due to seasonal shifts in ITCZ location. The authors suggest that the coupled system may amplify this signal on inter-annual timescales, to result in precession-driven signals in tropical Pacific climate records. Other authors, however, found a lack of ENSO-variability in compiled marine $\delta^{18}O_{SW}$ records from the Indo-Pacific Warm Pool (IPWP) and the EEP over the LGM or deglaciation (Gibbons et

al., 2013). The authors proposed large-scale variations in tropical hydrology to more closely parallel the NH-SH temperature gradient, strengthening the idea that the tropical atmosphere responds directly to AMOC variability (Gibbons et al., 2013). On the other hand, Tierney et al. (2012) hypothesized the alignment of the Holocene Buda stalagmite $\delta^{18}O$ record (Partin et al., 2007) with local mid-fall insolation to reflect a balance between two mechanisms: the direct effect of local summer insolation and the indirect effect of local summer insolation on the Indian Walker circulation manifest during the September-October-November season. Future high-resolution glacial-interglacial (G-IG) records from the IPWP at varying latitudes and in the Indian Ocean in addition to simple-model experiments that span orbital timescales with many G-IG cycles are needed to complement the Mulu stalagmite $\delta^{18}O$ record and discriminate between the various theories regarding the origins of precessional hydrological variability in the western Pacific.

Although equatorial fall insolation does not have an obliquity signal, the small obliquity peak in the 160ky Mulu record spectral analysis suggests a possible correlation between western tropical hydrology and obliquity variations (see Supplementary Materials, Appendix C). Because obliquity influences the meridional gradient of annual mean insolation there is likely to be a response in the mean meridional circulation with some effect on the hydrologic cycle (Clement et al., 2004). A cross-spectral analysis between the obliquity curve and the Mulu stalagmite record, however, found little coherence at the obliquity period (see Supplementary Materials, Appendix C). The lack of coherence may be due to the limitations of the relatively short 160ky record, which spans only four obliquity cycles. Alternatively, a portion of the tropical response to

obliquity forcing may be nonlinear and undetectable in a cross-spectral analysis. For example, because an increase in the earth's tilt increases annual mean insolation at higher latitudes and increases the amount of insolation in the summer season in both hemispheres, an increase in earth's tilt would extend the span of the north-south ITCZ annual migration to higher latitudes. Presently, at close to mean obliquity, Mulu sits beneath the ITCZ year round with an absence of a hydrologic seasonal cycle. At greater tilt, the ITCZ may have moved further north and south in the Warm Pool region during boreal and austral summers, respectively, introducing a seasonal rainfall pattern to Mulu and altering the mean annual $\delta^{18}O$. Additionally, modeling studies have found the strength of the Indonesian-Australian monsoon (AISM) to be sensitive to both precession and obliquity (Wyrwoll et al., 2007), providing another means for obliquity to influence Mulu stalagmite $\delta^{18}O$ that is not local. Simple isotope-enabled climate simulations with the addition or removal of obliquity v. precessional forcing will be investigated in the future to quantify response to different orbital forcings.

3.7 Conclusions

The Mulu stalagmite $\delta^{18}O$ record demonstrates that western tropical Pacific hydrology is sensitive to a wide variety of climate forcings. Once ice-volume corrected, the full Mulu stalagmite $\delta^{18}O$ reconstruction shows no evidence of a G-IG 100-ky cycle, confirming that climate variability related to hydrologic activity in the western tropical Pacific is either not strongly sensitive to greenhouse gas forcing or contributions from multiple forcings work in opposition. Pronounced deglacial $\delta^{18}O$ enrichments coincident with millennial-scale north Atlantic events are the largest signal throughout the entire 570 ky Mulu composite stalagmite record and are absent in other regional hydrologic records.

This suggests that the combination of forcings responsible for the anomalous Heinrich $\delta^{18}O$ enrichments are particular to western tropical Pacific hydrology. When insolation signals are not muted, the composite Mulu $\delta^{18}O$ record varies in phase with equatorial mid-fall insolation, suggesting that the mechanism(s) responsible for the coupling of Mulu stalagmite $\delta^{18}O$ and mid-fall insolation is the dominant cause of western Pacific hydroclimate variability on orbital timescales. This is best illustrated across Termination II, when Mulu $\delta^{18}O$ tracks fall insolation that is out of phase with the timing of the deglaciation.

The composite Mulu $\delta^{18}O$ record at the penultimate deglaciation shares similarities with Termination 1 regarding the timing of deglaciation events, but the ice-volume corrected Mulu records are 1‰ larger at H11 than H1. We propose the combination of low equatorial mid-fall insolation plus a large southward shift in ITCZ as the primary cause of the significant enrichment at H11, and to a lesser extent, H1.

As a whole, the Mulu stalagmite $\delta^{18}O$ records suggest a limited role for greenhouse gas forcing in driving western tropical Pacific hydrology over the last G-IG cycle. This observation, when combined with the unique structure of millennial-scale deglacial enrichments in stalagmite $\delta^{18}O$, makes the Mulu stalagmite $\delta^{18}O$ records compelling targets for paleoclimate modeling studies aimed at resolving the mechanisms of G-IG variability. This is a significant addition to our understanding of the response of tropical hydrology to greenhouse forcing, and useful to data-model simulation comparisons used to validate future climate change projections.

3.8 Acknowledgements

We thank Jessica Moerman, Danja Mewes, and Sang Chen for field work assistance, our exceptional park guides Syria Lejau and Jenny Malang for their expertise and guidance through the forest and into the cave chambers, and all the staff at Gunung Mulu National Park World Heritage Site for their dedicated assistance during fieldtrips. We also thank Guillaume Paris, Sophie Hines, James Rae, and Andrea Burke for their assistance in U–Th dating, and Hussein Sayani, Pamela Grothe, and Tammy Chang for their assistance in oxygen isotope measurements. The research was funded by NSF PECASE Award #0645291 to K.M.C., NSF AGS award #0903099 to JFA, and a NSF Graduate Research Fellowship to S.A.C. Permits for this work were granted by the Malaysian Economic Planning Unit, the Sarawak State Planning Unit, and the Sarawak Forestry Department. All data reported in this paper are archived at NCDC (ftp://ftp.ncdc.noaa.gov/pub/data/paleo/speleothem/pacific/gunung-mulu2014.txt).

CHAPTER 4

CONCLUDING REMARKS AND FUTURE WORK

An understanding of the mechanisms responsible for variability in the tropical hydrologic cycle is a crucial component in projecting future changes in rainfall patterns. Past tropical hydroclimate variability, however, is a poorly-constrained system currently subject to multiple climate forcings. In this thesis we present a large compilation of overlapping U/Th-dated Gunung Mulu stalagmite $\delta^{18}O$ records spanning 0-160 kybp, the first tropical Pacific terrestrial record to resolve a complete G-IG cycle at high resolution (predominantly less than 100yr/sample) with the majority of relative age errors <1%. The extended Mulu stalagmite 160ky $\delta^{18}O$ record allows us to draw conclusions on the extent of different forcings on millennial and orbital timescales. The full Mulu stalagmite $\delta^{18}O$ reconstruction shows no evidence of a G-IG 100-ky cycle, suggesting that a linear relationship does not exist between CO_2 and western Pacific rainfall variability on orbital timescales. The composite Borneo $\delta^{18}O$ record does vary in phase with equatorial mid-fall insolation, suggesting that the mechanism(s) responsible for the coupling of Mulu stalagmite $\delta^{18}O$ and mid-fall insolation is the dominant cause of western Pacific hydroclimate variability on orbital timescales. Simple models able to simulate orbital scale variability of tropical hydrology will be used in the future to investigate different insolation, CO_2, and Sunda shelf exposure effects in coupled scenarios to investigate possible mechanisms. Finally, the glacial record implies a selective response of WPWP hydrology to high-latitude abrupt climate change forcing, challenging the idea that the mechanisms responsible for Heinrich events and D/O events have similar global effects.

4.1 Future and ongoing research

4.1.1. Mulu karst system modeling

The depleted ($^{234}U/^{238}U$) found in almost every stalagmite sample in this thesis is a puzzling observation. Uranium disequilibrium in waters can be caused by two different mechanisms, (1) alpha recoil of ^{234}U directly into solution, or (2) preferential leaching of ^{234}U from crystal lattice sites disrupted from alpha decay (Rosholt in Ivanovich and Harmon, 1982), both of which input additional ^{234}U into the karst waters, increasing ($^{234}U/^{238}U$) > 1. Mulu bedrock samples reveal the sampled overlying limestone to be enriched in ^{234}U, leading to the "Mulu limestone conundrum" of apparent depleted stalagmite-forming waters and enriched overlying bedrock. One proposed theory to explain the bedrock/stalagmite enrichment/depletion is that the Mulu karst system is composed of mixed previously weathered limestone (depleted) and secondary precipitated calcite (enriched), and that the collected stalagmites are forming from dripwaters in contact with the weathered limestone and not the secondary calcite precipitate. Construction of a box model that incorporates uranium isotopes, Mg, and Sr (trace elements related to prior calcite precipitation) should be done to investigate uranium isotope transport through a karst system with varying flow rates and residence times in order to quantify expected dripwater and stalagmite uranium disequilibrium to test this theory.

4.1.2. Climate effects of the Toba super-eruption

The largest millennial-scale anomaly in the Borneo records is not a Heinrich event, but rather an abrupt increase in $\delta^{18}O$ coincident with a similarly large and abrupt increase in Chinese stalagmite $\delta^{18}O$, possibly associated with the Toba super-eruption.

Climate models suggest that climate anomalies associated with a large Toba-sized eruption should dissipate within a few decades (Timmreck, 2012). However, the Borneo and Chinese stalagmite records imply that anomalously dry conditions ensued immediately following the Toba super-eruption, suggesting that the eruption triggered at least a regional shift in large-scale climate patterns that persisted for a millennium. If the eruption caused a millennial-scale hydroclimate shift that reached throughout Southeast Asia and the Indo-Pacific, then the climate models may be missing an important source of multi-century persistence in the region's climate response. Additional high-resolution records from across the tropics, as well as a better understanding of the radiative effects of an eruption the size of Toba, would better constrain Toba's role in global climate during this time period.

The amount of sulfur gas injected into the stratosphere, and consequently the extent to which earth's atmospheric albedo was perturbed, is one key component to the discussion surrounding Toba's global and regional impact on climate that remains highly uncertain. Sulfur incorporated into stalagmites has the potential to provide a wealth of new information, including a record of regional volcanic eruptions and an additional vote on the magnitude of sulfur emissions from large stratospheric eruptions. A first-pass SIMS analysis of sulfur concentration variability in sample SC03 (200-yr resolution $\delta^{18}O$ measurements around the Toba super-eruption published in Carolin et al. (2013)) reveals promising results. Some evident sulfur peaks are within age error of the sulfur peaks in the ice cores (Svennson et al., 2013), though an extended record and demonstrated reproducibility is needed before any conclusions can be made.

APPENDIX A:

METHODS FOR MINIMIZING AGE ERROR

U-series age model constraints in Mulu calcite

U/Th age model construction is a distinct attribute of stalagmite paleorecords that distinguishes them from other radiocarbon-dated climate proxy records. A stalagmite with substantial uranium concentration and minimal detrital contamination can produce U/Th ages to constrain the age and growth rate of the calcite formation to <0.5% over the past several glacial cycles. Several stalagmites collected from Gunung Mulu National Park, however, have either low uranium concentrations (<200 ppb), high detrital contamination, or both, leading to much greater age errors and necessitating a robust approximation of initial thorium isotope ratios at deposition. Here we present a summary of best-practices that result in the lowest relative age errors for a particular sample with specified constraints, developed over the past several years by dating over 450 Mulu stalagmite samples.

1. Introduction

The equation used to calculate the age of carbonate from nuclides ^{230}Th, ^{234}U, and ^{238}U is provided below, with an initial ^{230}Th correction term included (eg., Ivanovich and Harmon 1992). Round parentheses indicate activity ratios. ^{230}Th and ^{234}U half-lives are provided in Cheng et al. (2013) (75,584 yrs and 245,520 yrs, respectively).

$$\left(\frac{230}{238}\right) = 1 - e^{-\lambda_{230}t} + \left[\left(\frac{234}{238}\right) - 1\right]\left(\frac{\lambda_{230}}{\lambda_{230} - \lambda_{234}}\right)\left(1 - e^{(\lambda_{234} - \lambda_{230})\cdot t}\right) + \left(\frac{232}{238}\right)\left(\frac{230}{232}\right)_{init} e^{-\lambda_{230}t}$$

As shown in the age model equation, age errors result from 3 measured isotopic ratios, (^{230}Th/^{238}U), (^{234}U/^{238}U), and (^{232}U/^{238}U), and one set value, $(^{230}U/^{232}U)_{init}$. The total error for each age is estimated using a Monte Carlo simulation (n=10,000). Isotope ratio errors

are a combination of chemical procedure blank errors and internal ICP-MS errors. Initial $^{230}Th/^{232}Th$ error is an artifact of the isochron analysis.

Minimizing analytical errors and accurately constraining the initial $^{230}Th/^{232}Th$ ratio are the two key components to constructing a robust age model with small relative age errors. An analysis of the initial $^{230}Th/^{232}Th$ ratio is provided in Partin et al. (2007), Carolin et al. (2013), and Chapter 3 of this thesis. Here we describe best-practices that result in the lowest relative age errors for a particular sample with specified constraints, developed over the past several years by dating over 450 Mulu stalagmite samples.

2. Minimizing analytical errors

Table A-S1 lists example measured isotopic ratios and the associated overall relative age error calculated using a Monte Carlo simulation. Figure A-S1. visually demonstrates age error contributions from the measured isotope ratios, excluding detrital isotope contamination. On the left are plotted the 192 measured U-series samples from the 9 stalagmites used in this thesis, and on the right are example error bars in the x- and y-axis correlated to ±10ky for three different ages with measured $(^{234}U/^{238}U) \approx 0.9$. While at younger ages $(^{234}U/^{238}U)$ has almost no influence in the age equation, for older samples errors associated with both $(^{230}U/^{238}U)$ and $(^{234}U/^{238}U)$ contribute significantly to the total age error. Stalagmites used in Chapters 2 and 3 are particularly disadvantaged, as all samples' measured $(^{234}U/^{238}U)$ are depleted in ^{234}U, making an already tiny measurement even smaller, several factors less than most other published stalagmite concentrations.

Table A-S1. Example measured isotopic ratios and the associated overall relative age error calculated using a Monte Carlo simulation. Yellow highlight indicates lowest age error in scenario pool for specified age of sample.

Sample	$\left(\frac{234}{238}\right)$	2σ err.	$\left(\frac{230}{238}\right)$	2σ err.	$\left(\frac{232}{238}\right)$	2σ err.	$\frac{230}{232}^{init}$	2σ err.	Total 2σ Err
Age = 35 ky									
Ex. 1A	0.900	1 ‰	0.250	1 ‰	8.0 e-4	10 ‰	50	20	390 yr (11 ‰)
Ex. 1B	0.900	**0.5 ‰**	0.250	1 ‰	8.0 e-4	10 ‰	50	20	375 yr (11 ‰)
Ex. 1C	0.900	1 ‰	0.250	**0.5 ‰**	8.0 e-4	10 ‰	50	20	380 yr (11 ‰)
Ex. 1D	0.900	**0.5 ‰**	0.250	**0.5 ‰**	8.0 e-4	10 ‰	50	20	355 yr (10 ‰)
Ex. 1E	0.900	1 ‰	0.250	1 ‰	**4.0 e-4**	10 ‰	50	20	220 yr (5 ‰)
Ex. 1F	0.900	1 ‰	0.250	1 ‰	8.0 e-4	10 ‰	50	**5**	155 yr (5 ‰)
Ex. 1G	0.900	1 ‰	0.250	1 ‰	**4.0 e-4**	10 ‰	50	**5**	130 yr (4 ‰)
Ex. 1H	0.900	**0.5 ‰**	0.250	**0.5 ‰**	**4.0 e-4**	10 ‰	50	20	195 yr (5 ‰)
Age = 90 ky									
Ex. 2A	0.900	1 ‰	0.500	1 ‰	8.0 e-4	10 ‰	50	20	575 yr (5 ‰)
Ex. 2B	0.900	**0.5 ‰**	0.500	1 ‰	8.0 e-4	10 ‰	50	20	500 yr (5 ‰)
Ex. 2C	0.900	1 ‰	0.500	**0.5 ‰**	8.0 e-4	10 ‰	50	20	515 yr (5 ‰)
Ex. 2D	0.900	**0.5 ‰**	0.500	**0.5 ‰**	8.0 e-4	10 ‰	50	20	430 yr (5 ‰)
Ex. 2E	0.900	1 ‰	0.500	1 ‰	**4.0 e-4**	10 ‰	50	20	470 yr (5 ‰)
Ex. 2F	0.900	1 ‰	0.500	1 ‰	8.0 e-4	10 ‰	50	**5**	445 yr (5 ‰)
Ex. 2G	0.900	1 ‰	0.500	1 ‰	**4.0 e-4**	10 ‰	50	**5**	435 yr (5 ‰)
Ex. 2H	0.900	**0.5 ‰**	0.500	**0.5 ‰**	**4.0 e-4**	10 ‰	50	20	275 yr (3 ‰)

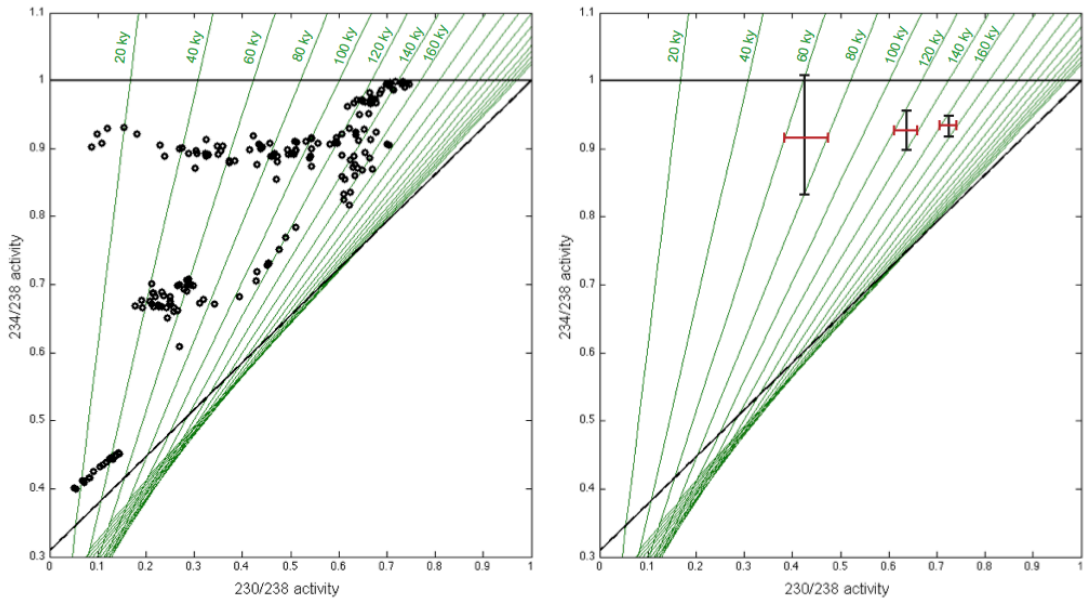

Figure A-S1. Variation of ($^{234}U/^{238}U$) and ($^{230}Th/^{238}U$) with time in a closed system assuming initial $^{230}Th = 0$. Green lines are isochrons, lines of constant age over various ($^{234}U/^{238}U$) activity ratios. The solid diagonal black line is the infinite age line, and the solid horizontal black line is ($^{234}U/^{238}U$) = 1, secular equilibrium. Measured sample ratios are plotted in the left plot. Visual error bars between isochrons in the x- and y-direction are shown in the right plot.

If uranium concentration is low, drilled sample size can have a significant effect on analytical errors due to counting statistics. In this thesis, the uranium content of the nine stalagmites ranges from 35 – 1,490 ppb, resulting in a large range in individual sample weight requirements. Smaller sample size is ideal, as it allows for targeting the "purest" calcite while avoiding areas with visually evident detrital contamination. Additionally, smaller calcite samples average over fewer layers of precipitated calcite, an important advantage when sampling slower growing stalagmites. Table A-S2 shows a rough approximation of the internal error ($1/\sqrt{N}$) associated with ($^{234}U/^{238}U$) and ($^{230}Th/^{238}U$) isotope ratios given 3 stalagmite uranium concentrations: 500 ppb, 100 ppb, and 50 ppb in a 200 mg sample. The average recovery rate used is based on column

elution chemistry that has been refined and perfected using hand-made PTFE heat-shrink tubing columns, and U and Th fraction analysis carried out on a Finnigan Neptune ICP-MS with an Aridus II Desolvating Nebulizer injection system. ^{234}U is measured with a Secondary Electron Multiplier (SEM) and ^{230}Th with a Multi Ion Counter (MIC).

Table A-S2. Internal error ($1/\sqrt{N}$) associated with ($^{234}U/^{238}U$) and ($^{230}Th/^{238}U$) isotope ratios given 3 stalagmite uranium concentrations: 500 ppb, 100 ppb, and 50 ppb in a 200 mg sample.

Isotope	Conc.	Weight	Counter	Total Atoms	Recovery	N	$1/\sqrt{N}$
238-U = 500 ppb							
234-U	25 ppt	200 mg	SEM	1.3 e10	3.0‰	3.9 e7	0.2 ‰
230-Th	5 ppt	200 mg	MIC	2.5 e9	3.5‰	9.2 e5	0.3 ‰
238-U = 100 ppb							
234-U	5 ppt	200 mg	SEM	2.5 e9	3.0‰	7.7 e5	0.4 ‰
230-Th	1 ppt	200 mg	MIC	5.2 e8	3.5‰	1.8 e5	0.7 ‰
238-U = 50 ppb							
234-U	2.5 ppt	200 mg	SEM	1.3 e9	3.0‰	3.8 e7	0.5 ‰
230-Th	0.5 ppt	200 mg	MIC	2.5 e8	3.5‰	9.2 e5	1.0 ‰

Under ideal conditions, the target intensity loading onto an SEM is 35,000 cps (1.5e7 counts over 420 sec, $1/\sqrt{N} = 0.3‰$), while the maximum intensity loading onto an MIC is 25,000 cps (1.0e7 counts over 420 sec, $1/\sqrt{N} = 0.3‰$). Thus, for example, as shown in Table A-S2, samples with [U] greater than 500 ppb should not be drilled for more than 200 mg of calcite, as any weight greater would not lower counting statistic errors on the SEM or MICs based on the maximum intensity limit. For stalagmites with lower concentrations, each sampling spot must be analyzed individually to determine the sample size that will result in the least risk of detrital contamination while also minimizing counting statistic errors.

Finally, the added spike amount can also significantly effect sample size due to possible dilution necessity. For this thesis, the lab's internal $^{236}U/^{229}Th$ mixed spike has $[^{236}U] \approx 8$ ppm and $[^{229}Th] \approx 40$ ppt, with the uranium fraction measured on a faraday cup and the thorium fraction measured on a second MIC. Caution must be taken when spiking the sample so that the thorium fraction is not overloaded with ^{229}Th, forcing unnecessary dilution before sample loading and loss of critical ^{230}Th counts. Analysis of individual stalagmite uranium concentrations at depths along the growth axis assists greatly in determining best-case spike amount with the given sample size.

APPENDIX B:

SUPPLEMENTARY MATERIALS FOR

"VARIED RESPONSE OF WESTERN PACIFIC HYDROLOGY TO CLIMATE FORCINGS OVER THE LAST GLACIAL PERIOD"

Methods and Materials

I. General Description of Stalagmites

The four stalagmites were collected from Gunung Mulu and Gunung Buda National Parks (4°N, 115°E) (Fig. B-S1). SCO2 and SC03 were recovered from Secret Cave at Gunung Mulu in 2006, SCH02 from Snail Shell Cave at Gunung Buda in 2003, and BA02 from Bukit Assam Cave at Gunung Buda in 2003. Borneo stalagmites are particularly difficult to date because they have relatively low ^{238}U concentrations, negative $\delta^{234}U$ values, and contain appreciable levels of detrital thorium. For this reason, we overlap four $\delta^{18}O$ records from separate stalagmites with different growth rates from caves 20 km apart in order to confirm reproducibility and robustness of the resulting composite oxygen isotopic record. 101 dates were measured across 4 stalagmites, of which 5 fell out of chronological order. 95 of the 101 dates have relative 2σ age errors less than 2.0%, and 77 dates have relative 2σ age errors less than 1.0%. The new Borneo $\delta^{18}O$ record is unique in that of the 85ky-period covered by the reconstruction, over 50ky are covered by 2 separate overlapping stalagmite records, 30ky by 3 overlapping stalagmite records, and 8ky by all 4 overlapping stalagmite records. As expected, comparing multiple $\delta^{18}O$ records for a given time period allows for a clear visual identification of age model errors associated with dating uncertainties. This is evident by comparing the timing of five major $\delta^{18}O$ excursions that are shared across all of the stalagmite $d^{18}O$. To correct for small offsets in the timing of such events between the individual stalagmite $d^{18}O$ records, we align these events across the four records within the 2σ age errors associated with each stalagmite age model. We also plot the original age model in Figure 1 of the main paper, which differs only slightly from the corrected age

model (see Table B-S4). Our main conclusions are not dependent on the choice of raw versus aligned age models.

II. U-Series Age Model Construction

Age models were constructed for each stalagmite using U-series disequilibrium (^{238}U-^{234}U-^{230}Th) measurements with the isotopic compositions of the U and Th fractions determined with a Finnigan Neptune MC-ICPMS at Caltech (see Methods from Partin et al., 2007). We report measured [^{238}U], [^{232}Th], $\delta^{234}U$, and $(^{230}Th/^{238}U)_A$ in Table B-S1 for all samples. The Secret Cave samples (SC03 and SC02) have the lowest ^{238}U and detrital Th concentrations, and the measured $\delta^{234}U$ ratios are negative and close to zero ($^{234}U/^{238}U$ activity closer to secular equilibrium). The Snail Shell Cave (SCH02) and Bukit Assam Cave (BA02) samples have greater ^{238}U and detrital Th concentrations, with more depleted measured $\delta^{234}U$ ratios. A triple isotope plot (Figure B-S10), which graphically displays the range of $\delta^{234}U$ and $^{230}Th/^{238}U$ values for each stalagmite, shows that sample BA02 is particularly difficult to date as its initial $\delta^{234}U$ values place it close to the infinite age line.

A. Calculating Detrital $^{230}Th/^{232}Th$ Contamination

We analyzed seven isochrons for this study, which are added to the 4 isochrons previously published for stalagmites from Bukit Assam cave and 3 isochrons previously published for stalagmites from Snail Shell cave (see Partin et al., 2007). The isotopic ratios used to create Osmond Type-II isochrons, $(^{232}Th/^{238}U)_A$, $(^{230}Th/^{238}U)_A$, and $(^{234}U/^{238}U)_A$, and their associated analytical 2σ errors are provided in Table S2. Osmond Type-II diagrams were used to determine detrital $^{230}Th/^{232}Th$ concentrations because normalizing to ^{238}U makes deviation from a linear fit much more evident than

normalizing to ^{232}Th (Ludwig and Titterington, 1994). We implemented ISOPLOT 3.72 (*37*) to calculate the detrital ^{230}Th/^{232}Th concentration, which utilizes a maximum-likelihood estimation (MLE) XY-XZ isochron algorithm and a simple ^{232}Th correction algorithm (Ludwig and Titterington, 1994). These algorithms simultaneously determine the best fit to a set of XY (^{230}Th/^{238}U-^{232}Th/^{238}U) points and a set of XZ (^{234}Th/^{238}U-^{232}Th/^{238}U) points. Error ellipses in the XY-XZ isochron diagrams are dominated by ^{234}U, ^{230}Th, and ^{232}Th measurement uncertainties. However, it is almost always the degree of scatter of points about a line, coupled to the spread of the data points along the axes (rather than the analytical error bars), that determines the uncertainty in the initial ^{230}Th/^{232}Th ratio. All isochrons for each cave system are plotted on the same Osmond Type-II plot in Figure B-S11. The age, planar intercepts, and detrital ^{230}Th/^{232}Th concentrations for each isochron calculated using the ISOPLOT 3.72 program are provided in Table B-S3, along with uncertainties.

The large scatter of ^{230}Th/^{232}Th values from the individual isochrons (Table B-S3) is an indication that more than one source of initial ^{230}Th exists in our system and motivates us to take a conservative approach (i.e. larger error bars) to estimating a detrital ^{230}Th/^{232}Th ratio that is representative of our cave system. The weighted means and standard deviations for the detrital ^{230}Th/^{232}Th concentration are calculated for each stalagmite using the inverse of the 1σ errors from each isochron as the weighting factor (Table B-S3). The weighted standard deviation is equal to the inverse of the sum of the weights for each cave system. Un-weighted means and standard deviations (for the population of isochron results from the same stalagmite) are also calculated for comparison. There is a large difference between the weighted standard deviation and the

spread of the initial values from each line (the "un-weighted standard deviation"). For the final estimate of the detrital $^{230}Th/^{232}Th$ ratio we use the calculated weighted means and an uncertainty that lies between the simple population spread and the weighted uncertainty (Fig. B-S12). The final 2σ uncertainty was chosen so that (a) it overlaps the mean $^{230}Th/^{232}Th$ calculated from isochrons with 2σ error bars less than 10 ppm and (b) it overlaps the 2σ uncertainty of the mean $^{230}Th/^{232}Th$ calculated from isochrons with 2σ error bars greater than 10 ppm. We assign detrital atomic $^{230}Th/^{232}Th$ ratios as follows: BA02 = 56 ± 11 ppm; SCH02 = 59 ± 13 ppm; SC03 and SC02 = 111 ± 41 ppm (2σ errors; Fig. S12). These ratios are greater than the typical detrital bulk earth ratio (4 ± 2 ppm 2σ) frequently used in other stalagmite U-series dating applications. The greater detrital atomic $^{230}Th/^{232}Th$ ratio is likely due to the lack of other source rocks besides the Melinau Limestone in the Buda and Mulu cave. Our sampling site is essentially a rainforest draped over limestone with no other mineral sources of U or Th.

B. Final U-series Age Models

Table B-S1 lists the measured ^{238}U and ^{232}Th concentrations, the initial $\delta^{234}U$ ratios, and the $^{230}Th/^{238}U$ activity ratios for all 101 samples drilled for U-series dating. The reported ages and their 2σ uncertainties were estimated using a Monte Carlo technique that accounts for the errors in all isotope ratios and the uncertainty in the initial $^{230}Th/^{232}Th$ ratio. Analytical error contributions from $(^{230}Th/^{238}U)_A$ and $\delta^{234}U$ measurements are typically much smaller than error contributions due to uncertainty in the calculated detrital $^{230}Th/^{232}Th$. If the relative age error is greater than 2% of the calculated age, the date is not used in constructing a stalagmite age model. Also, if a repeat dating sample was drilled directly above or below a previously analyzed sample,

the date with the lower age error is used in the construction of a preliminary age model. Finally, the StalAge algorithm (Scholz and Hoffman, 2011) is used to determine if any additional U-series dates should be discarded as outliers. If a U-series date falls outside the StalAge model's 95% confidence interval, it is withheld from the final age model. The dates that are withheld from the final age model construction (as well as all isochron samples excluding the sample from each isochrons line with the smallest age error) are listed in Table B-S1 in red (blue for an isochron's data point). An age model was then constructed by linearly interpolating between consecutive ages. Our linearly interpolated model falls within the StalAge 95% confidence intervals for most of the record (Figure B-S3 through B-S6).

1. Hiatus detection

A high-resolution scanned image of each stalagmite and the corresponding backlit image reveal intervals of clear calcite (light) interrupted by detrital-contaminated calcite (dark) (Figures S3-S6). The beginning and ending of inferred hiatuses are indicated with colored arrows on the age-depth plots. Most potential hiatuses are identified in the stalagmite slab from optical evidence of a cessation of the carbonate accumulation (dark or white layer), and by U-series ages drilled immediately above and below such layers. Additional hiatuses were inferred wherever growth rates dropped below 10 μm/yr in Bukat Assam or Snail Shell stalagmites (average growth rate ~17 μm/yr) or 3 μm/yr in Secret Cave stalagmites (average growth rate ~5 μm/yr). Any $\delta^{18}O$ samples that fall on a potential hiatus were removed from the final oxygen isotope time series, as they are associated with large dating uncertainties. In the cases where hiatuses are inferred from dramatic changes in growth rate between two U-series dates, and where the culprit hiatus

is visible as a narrow band visible in the stalagmite images, growth rates from adjacent dates were linearly interpolated to the hiatus layer from both sides (see Partin et al., 2007; see Fig. B-S3 through B-S6).

2. Alignment of major features in the stalagmite $d^{18}O$ records

Because all four stalagmite samples were collected from caves within 20 km of each other we assume that large millennial-scale $\delta^{18}O$ excursions that are shared between the overlapping $\delta^{18}O$ records reflect contemporaneous climate events. We have thus adjusted the ages of those samples that have greater detrital contamination to the best-constrained age model in a given interval, to within 2σ dating errors, so that in the five major millennial-scale $d^{18}O$ excursions that are shared among the four records are aligned. The final "wiggle-matched" age model depths and ages for each stalagmite are provided in Table B-S4, which shows that the "wiggle-matched" dates fall within the 2σ age errors of the U-series dates.

As evident in Figure 4.1 and B-S8, the $\delta^{18}O$ maximum in SCH02 at ~40kybp occurs roughly 1000 years earlier than the corresponding $\delta^{18}O$ maxima in the other three stalagmites, even after shifting the SCH02 age tie points to the extent allowed by the 2σ dating errors. In general, SCH02 contains more detrital material and a larger number of visible hiatuses (some resolved by U/Th dates and some that are likely too small to be detected) than the other stalagmites (Figure B-S5). As such, we feel more confident in the age assignments from the other three stalagmites at the ~40kybp interval, as they agree remarkably well.

III. Stable isotope measurements

Oxygen isotopic analyses were conducted on powders drilled every 0.5mm or 1mm along the central growth axis of the stalagmites with a 1.6 mm drill bit. The $\delta^{18}O$ were analyzed on a Finnigan 253 equipped with a Kiel device at Georgia Tech (long-term reproducibility of less than ±0.07‰ (1σ)). All $\delta^{18}O$ data are reported with respect to VPDB.

IV. Generation of a temperature-corrected sea level curve

Waelbroeck et al.'s (2002) mean ocean $\delta^{18}O$ record derived from a temperature-corrected benthic $d^{18}O$ stack was used to adjust the Borneo $d^{18}O$ record to account for change in the mean $d^{18}O$ of seawater due to changes in ice volume. The derived mean ocean $\delta^{18}O$ record is plotted in Figure B-S7b. The individual stalagmite $d^{18}O$ records adjusted to account for the change in the $d^{18}O$ of the global ocean over the study interval are plotted in Figure B-S7c.

V. Calculation of Sunda Shelf areal exposure

An index tracking changes in the areal extent of the Sunda Shelf over the last glacial period was derived to determine how shelf exposure influenced hydroclimate variability in northern Borneo. Sunda shelf areal exposure was determined by converting the Waelbroeck et al.'s (Waelbroeck et al., 2002) derived sea level curve to relative areal shelf exposure using the NOAA ETOPO1 dataset of modern regional ocean bathymetry (http://www.ngdc.noaa.gov/mgg/global/ global.html). In deriving our index of Sunda shelf area, we counted the number of 1x1 arc-minute grid boxes (1 minute of latitude = 1.853 km at the equator) exposed in an area defined as 95°E-120°E and 10°S-10°N with every 1m lowering of global sea level down to -130m. We then calculated the fraction of

maximum Sunda shelf area exposure at each 1m interval. For example, if sea level is at -60m, then 452,048 grid boxes out of 611,208 Sunda shelf grid boxes are exposed, i.e. 74% of the Sunda shelf is above sea level. The resulting timeseries is plotted in brown in Figure B-S7d.

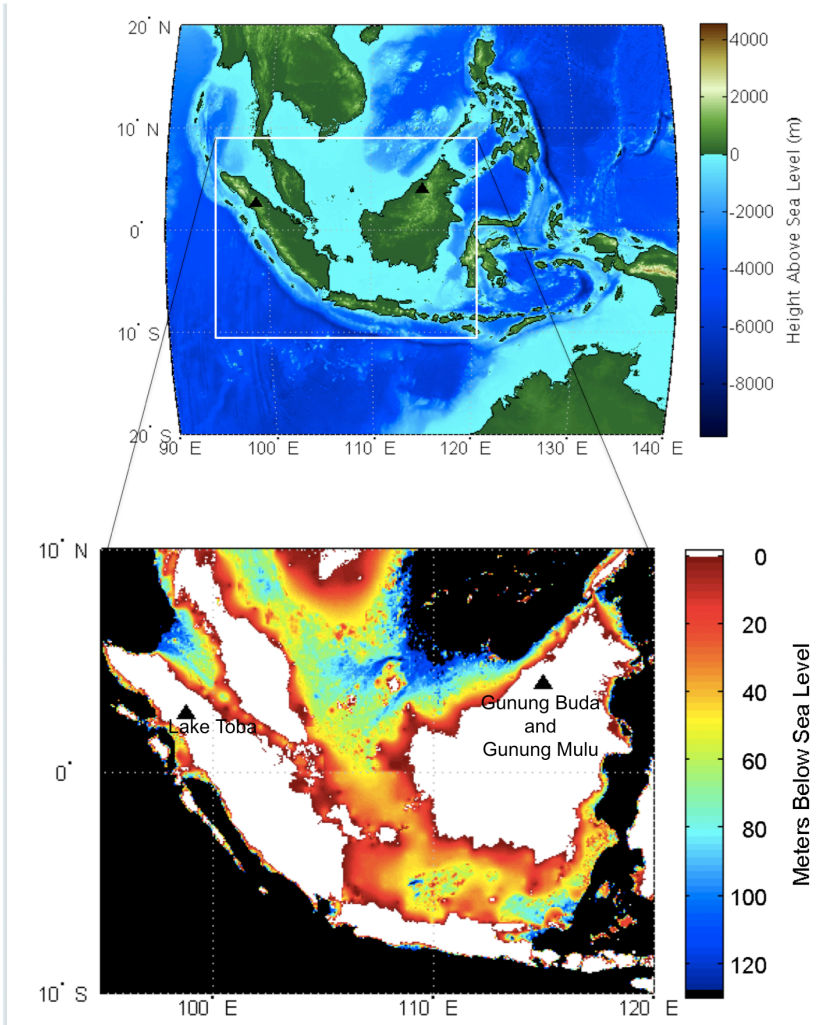

Figure B-S1. The location of Gunung Buda and Gunung Mulu National Parks relative to modern (top) and LGM (bottom) land/sea configurations. Topography and bathymetry provided in NOAA ETOPO1 dataset (http://www.ngdc.noaa.gov/mgg/global/global.html).

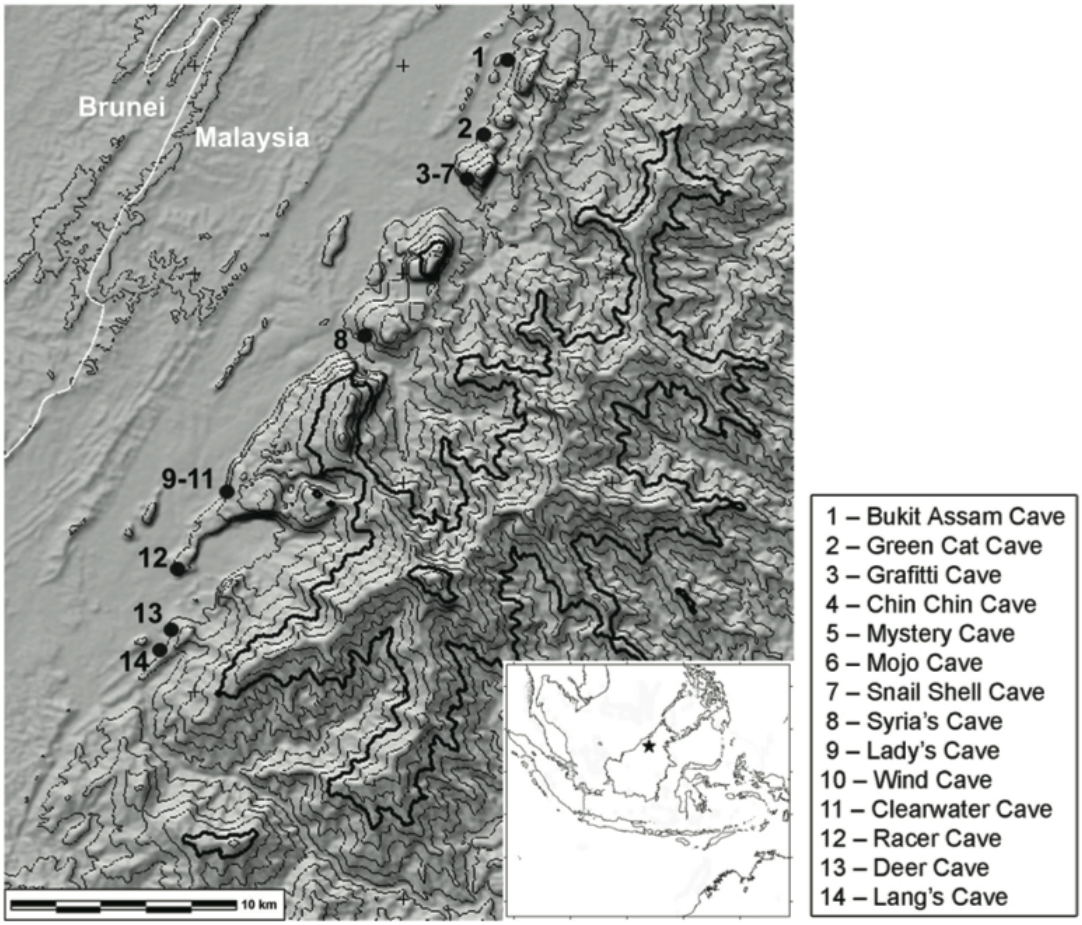

Figure B-S2: *From Partin, 2008*. Topographic map of Gunung Mulu and Gunung Buda National Parks, Malaysia, showing cave locations (contour interval is 200m). Our new records come from Bukit Assam Cave (BA02), Snail Shell Cave (SCH02), and Secret Cave (SC02 and SC03; Secret is a chamber located inside Clearwater Cave). Topological data provided in SRTM30 (http://www2.jpl.n•asa.gov/srtm/).

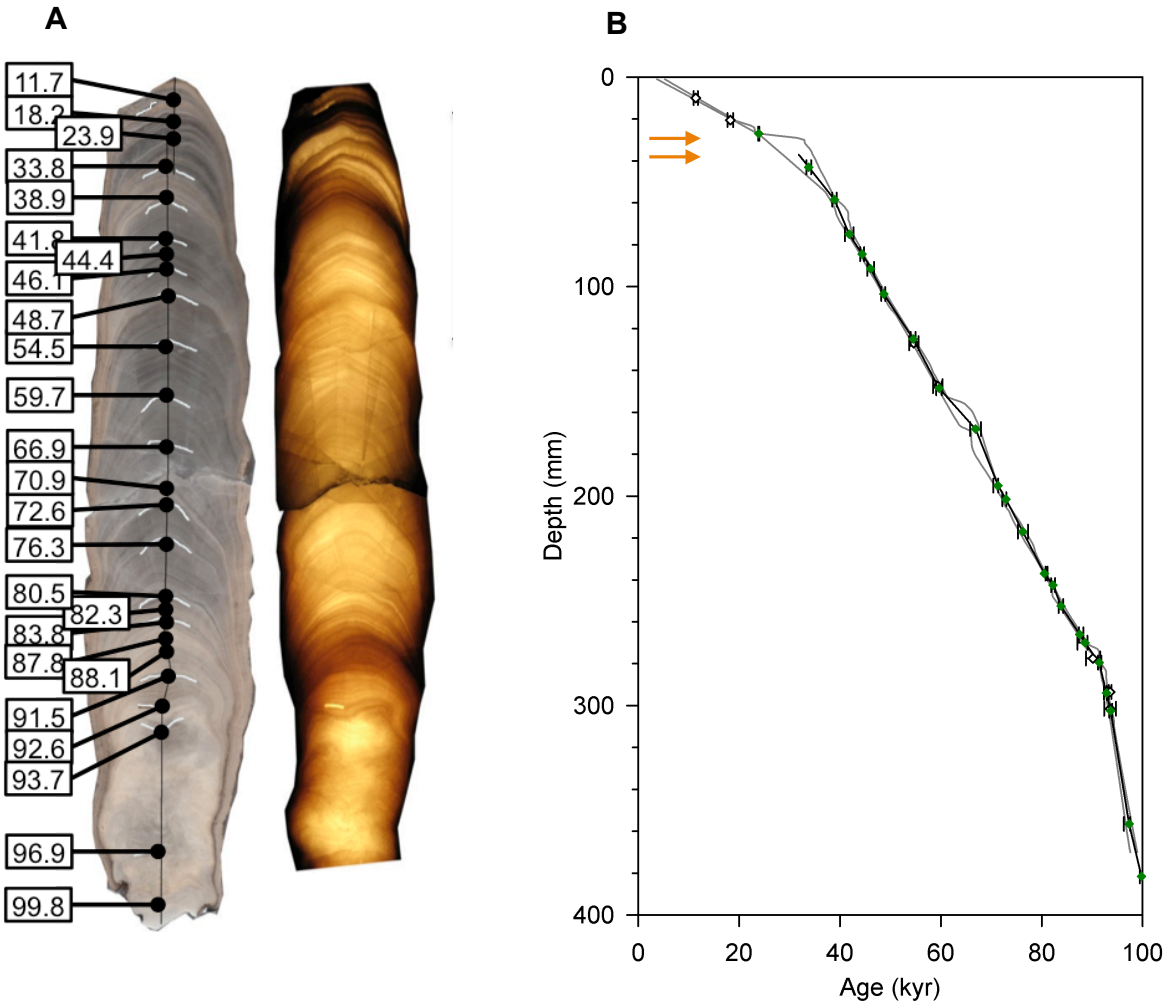

Figure S3. Reflected and backlit images for SC03 with its age versus depth plot. (A) High-resolution images of SC03, showing original U-series dates reported in kyr. Scale of photo matches y-axis scale used in age-depth plot in (B). (B) Age-depth plot for SC03. Data points in white are not included in age model (see Table S1). Data points in color are final ages used in age model (Table S4). Error bars represent 2σ dating uncertainties. Black line indicates our $\delta^{18}O$-aligned age-depth model for SC03. Grey outer curves indicate 95% confidence interval endpoints for an ensemble of age models produced using StalAge *(9).* The duration of an identified hiatus is indicated by colored arrows.

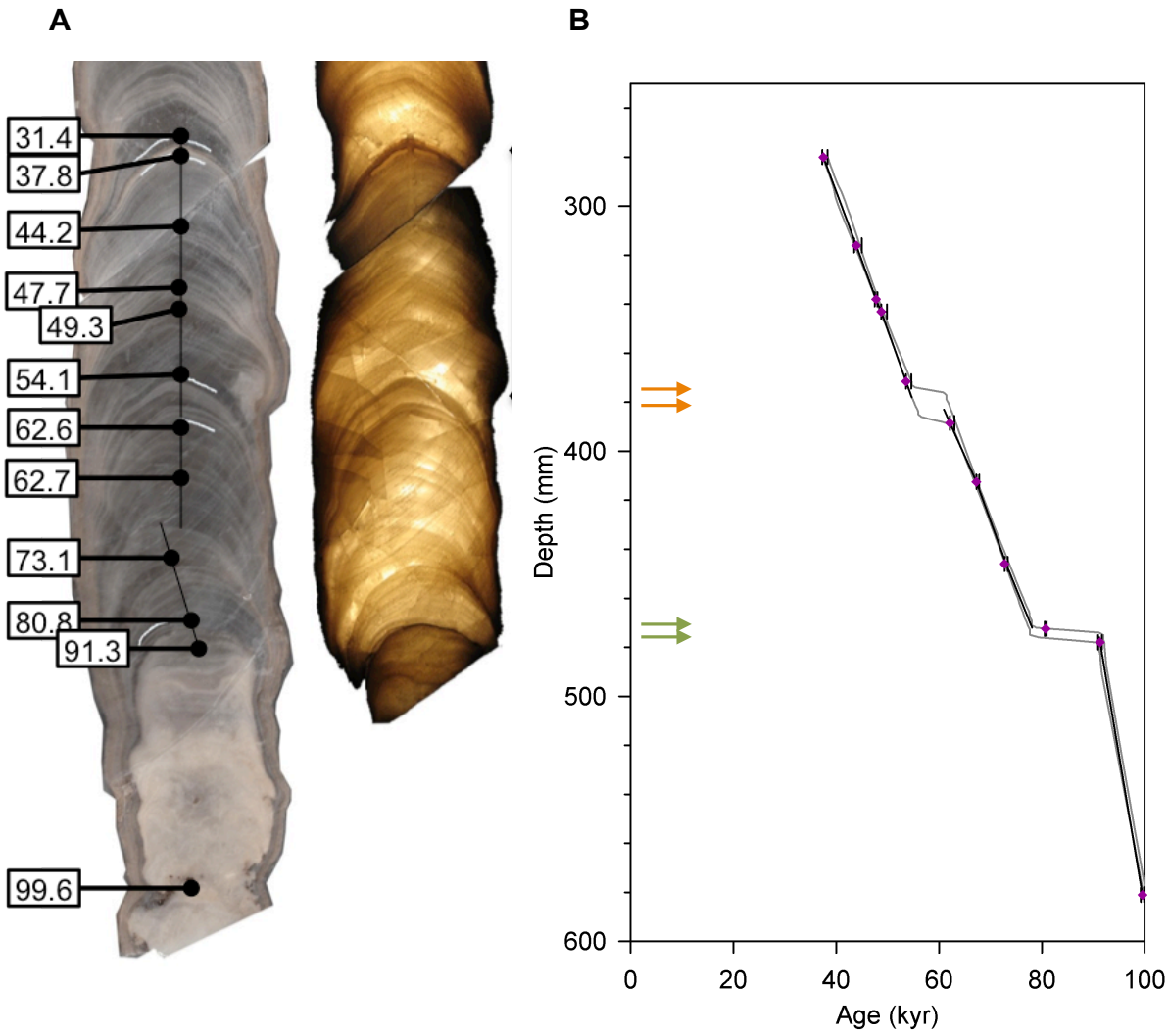

Figure S4. Same as Fig. S3 but for SC02. Two hiatuses are indicated.

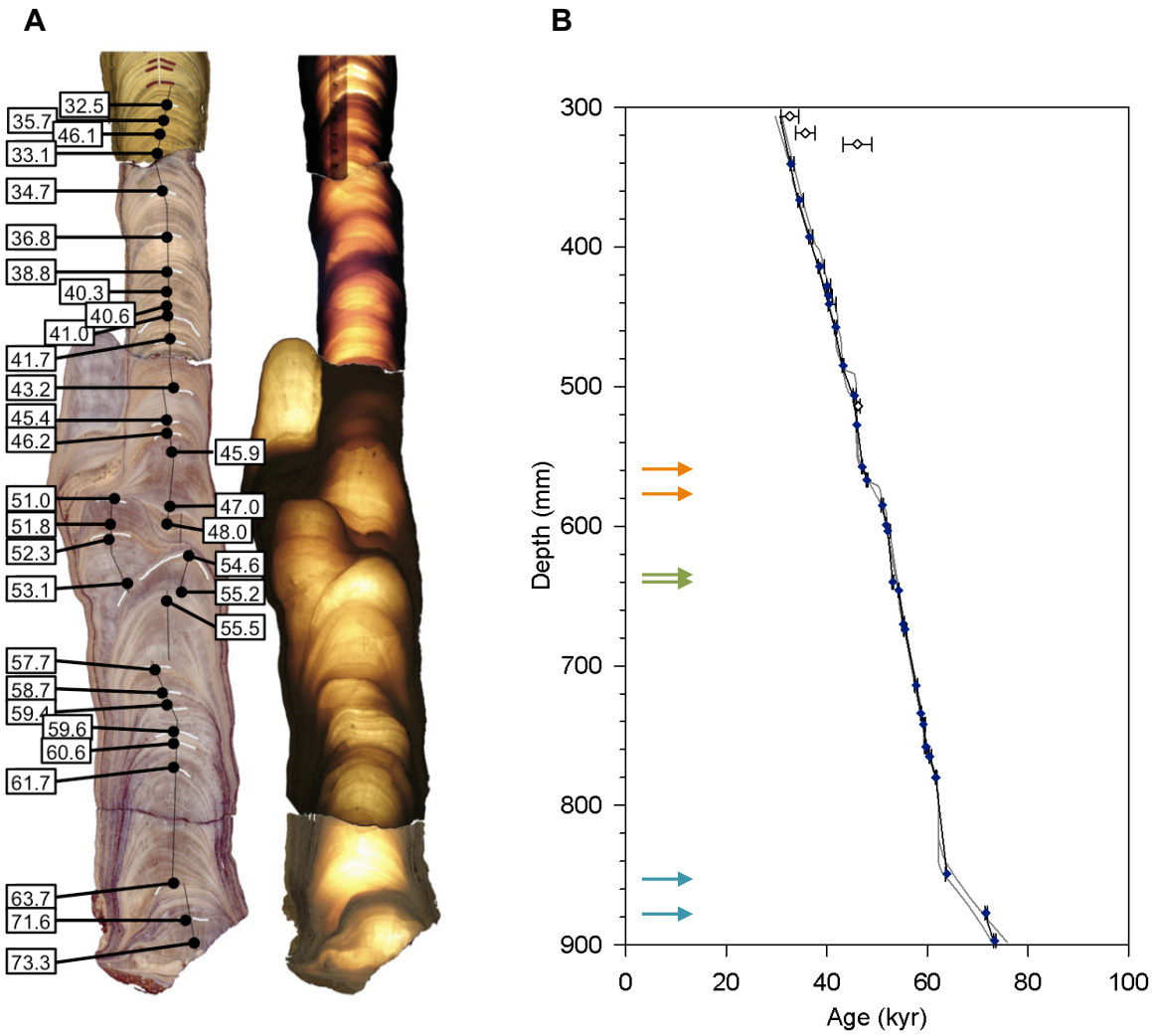

Figure S5. Same as Fig. S3 but for SCH02. U-series dates from 0-30kyrp are previously published (Partin et al., 2007). Three hiatuses are indicated.

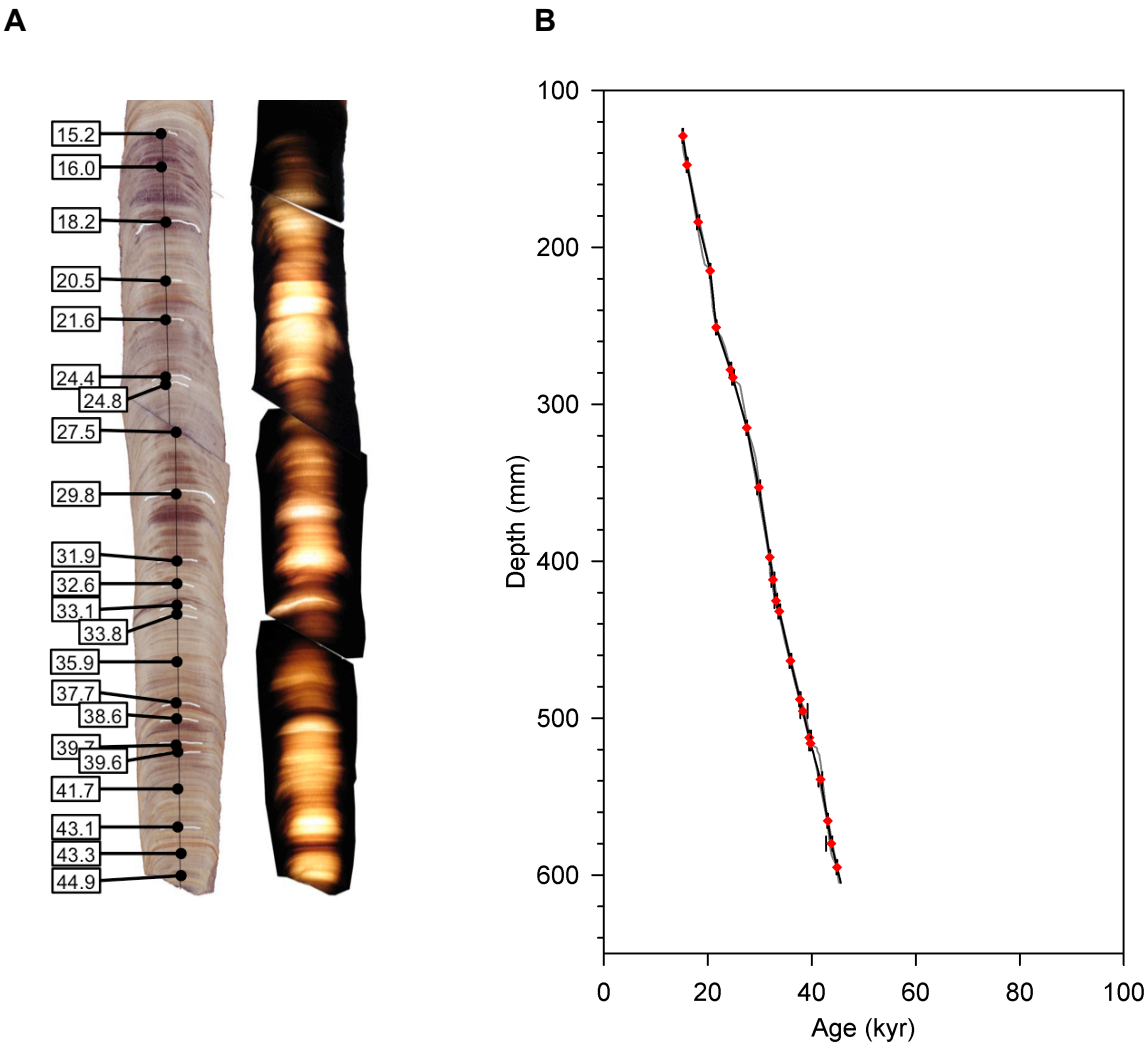

Figure S6. Same as Fig. S3 but for BA02. No hiatuses were found.

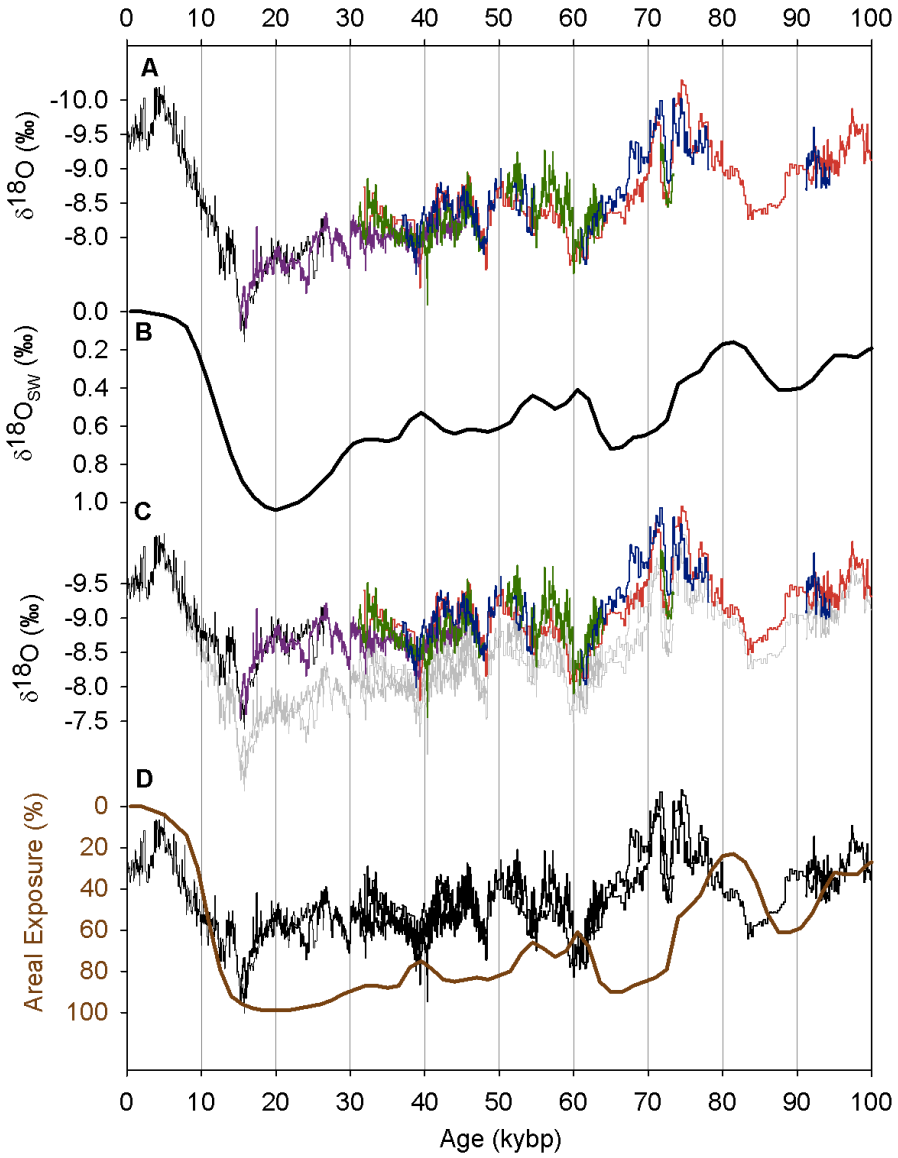

Figure S7. Timeseries of sea level and Sunda shelf areal exposure. **(A)** Borneo stalagmite d^{18}O records. **(B)** Derived mean ocean d^{18}O from temperature-adjusted benthic foraminifera stack (Waelbroeck et al., 2002) **(C)** The Borneo stalagmite d^{18}O records after removing the influence of mean ocean d^{18}O change due to ice volume (colors), plotted with the uncorrected Borneo stalagmite d^{18}O records (grey). See Supplemental text for details. **(D)** Areal Sunda Shelf exposure extrapolated non-linearly from calculated sea level variability (brown), plotted with ice volume-corrected Borneo stalagmite d^{18}O records from panel (C).

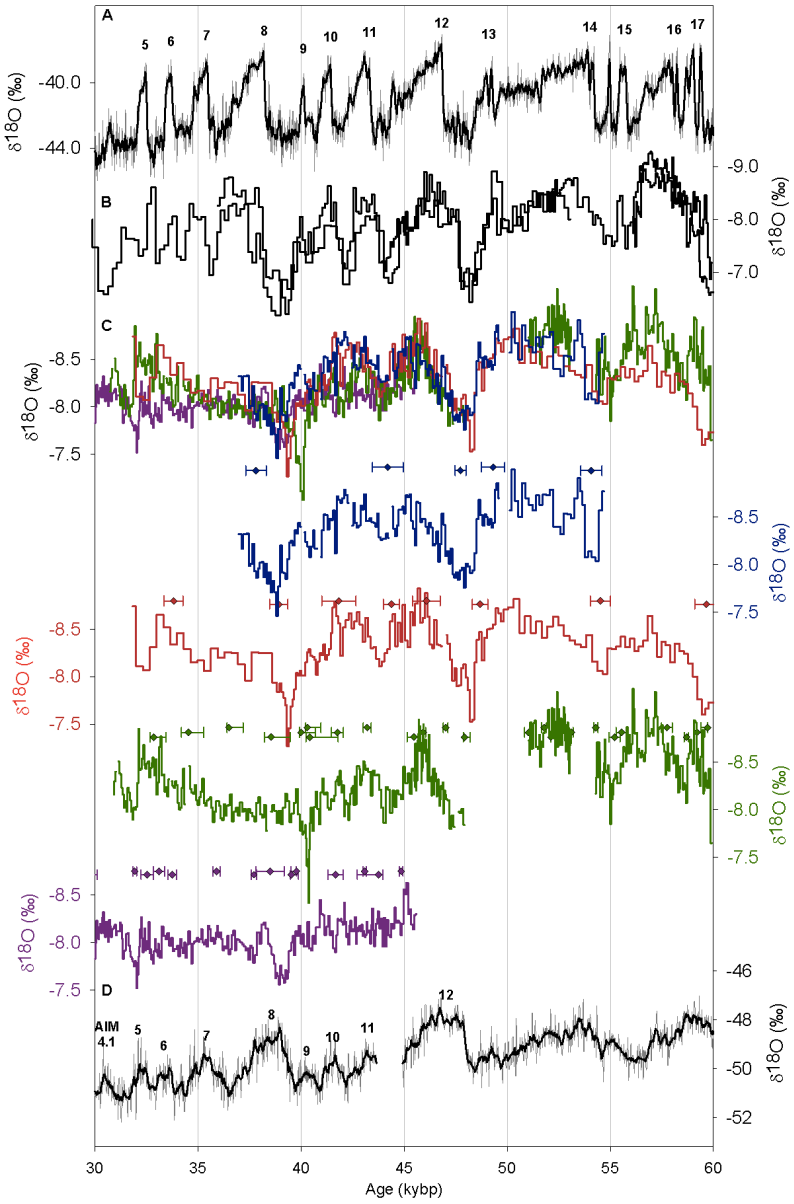

Figure S8. A detailed view of Stage 3 abrupt climate events as recorded in polar ice cores and in Chinese and Borneo stalagmite d^{18}O records. **(A)** Greenland NGRIP ice core $\delta^{18}O$ (grey; NGRIP members, 2004) with 100yr averages (black), plotted using the GICC05modelext age model (Wolff et al., 2010). Numbered D/O events are indicated. **(B)** Hulu/Sanbao cave stalagmite $\delta^{18}O$ records from China (Wang et al., 2001; 2008); The Sanbao $\delta^{18}O$ record has been offset by +1.6‰ for comparison. **(C)** The Borneo stalagmite $\delta^{18}O$ composite records and individual separated records: SC02 (navy), SC03 (red), SCH02 (green), BA02 (purple). U–Th dates used to construct age model used for the aligned composite record plotted in corresponding colors; error bars represent 2σ error (*8*). Raw U-Th dates are the midpoint of the plotted 2σ error bars, and are not shown. **(D)** EPICA Dronning Maud Land (EDML) ice core $\delta^{18}O$ (grey; EPICA members, 2006) with 7-year averages (black). Antarctica Isotope Maxima (AIM) are indicated.

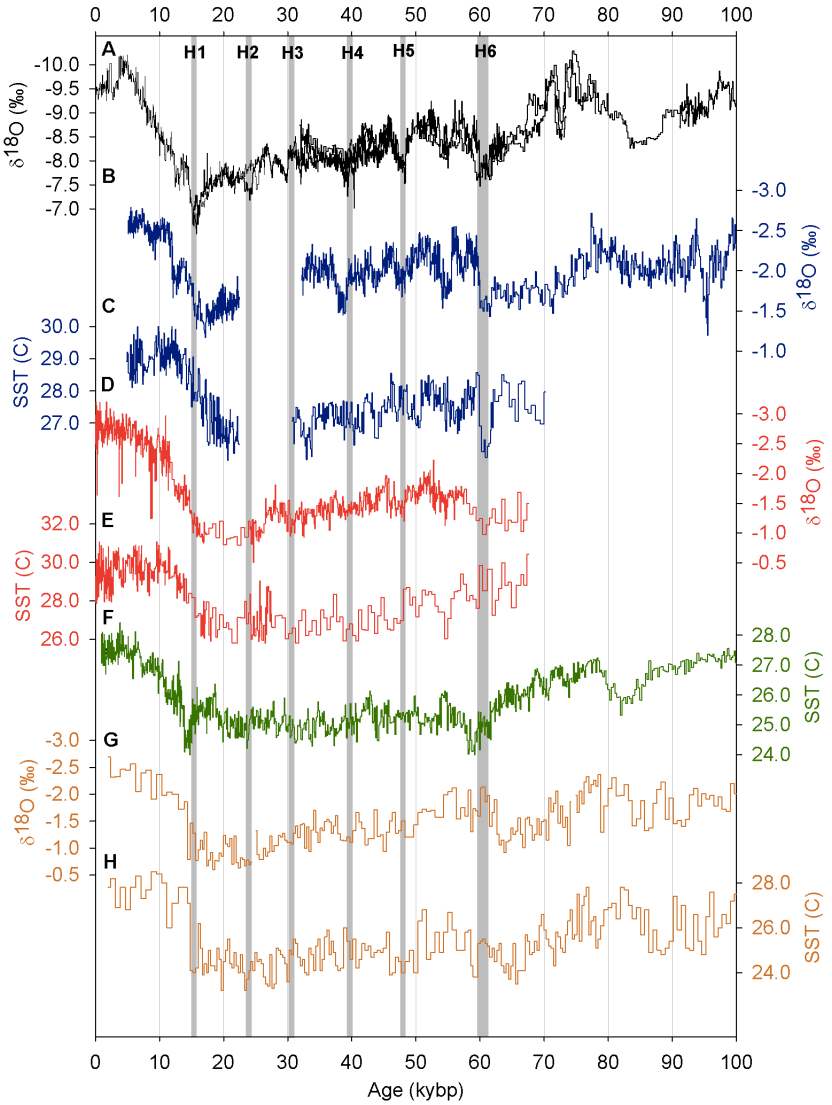

Figure S9. The Borneo stalagmite d^{18}O records plotted with a variety of western tropical Pacific sediment core δ^{18}O and SST records. (**A**) Borneo stalagmite d^{18}O records (uncorrected for ice volume). (**B**) Sulu Sea planktonic foraminifera δ^{18}O (Dannenmann et al., 2003), plotted using an updated age model using IntCal09 calibration curve 41kybp-modern and aligning 60kybp d^{18}O excursion to the Hulu/Sanbao stalagmite d^{18}O records. **(C)** Sulu Sea planktonic foraminiferal Mg/Ca SST record (Dannenmann et al., 2003), plotted using same updated age model as (B) **(D)** Site MD98-2181 planktonic foraminiferal δ^{18}O (Stott et al., 2002). **(E)** Site MD98-2181 planktonic foraminiferal Mg/Ca SST record (Stott et al., 2002). **(F)** South China Sea Site MD97-2151 UK'_{37} SST (Zhao et al., 2006). **(G)** South China Sea ODP Site 1145 planktonic foraminifera δ^{18}O (*17*). (**H**) ODP Site 1145 planktonic foraminifera Mg/Ca SST record (Oppo and Sun, 2005). Grey vertical bars reflect the timing of Heinrich events H1-H6 (Hemming et al., 2004) as recorded in the well-dated Chinese stalagmite δ^{18}O age models (Wang et al., 2001; 2008).

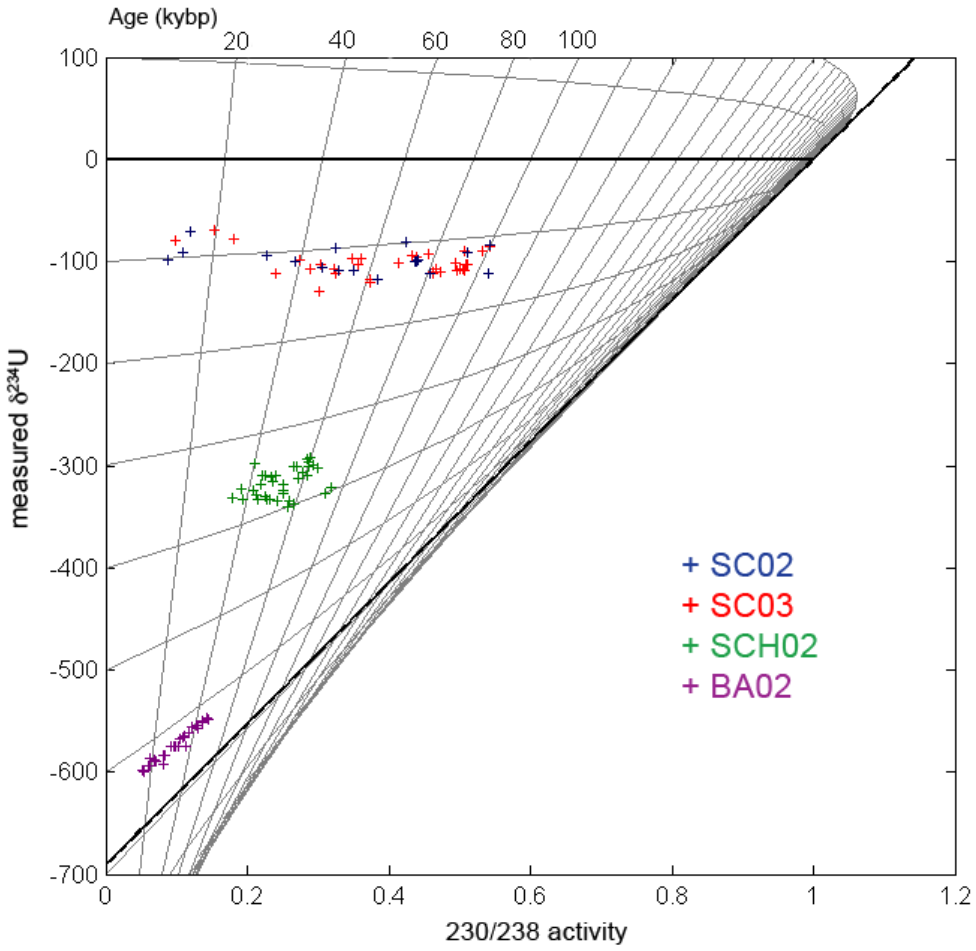

Figure B-S10. Diagram of the ^{238}U-^{234}U-^{230}Th age equation, assuming zero initial ^{230}Th. Horizontal gray contours are lines of constant initial $d^{234}U$, and vertical gray lines are lines of constant time, at 20kyr intervals. The black diagonal line is the infinite age line. Measured isotopic data from all age samples (see Table B-S1) are plotted as '+' data points – SC02 (navy), SC03 (red), SCH02 (green), and BA02 (purple).

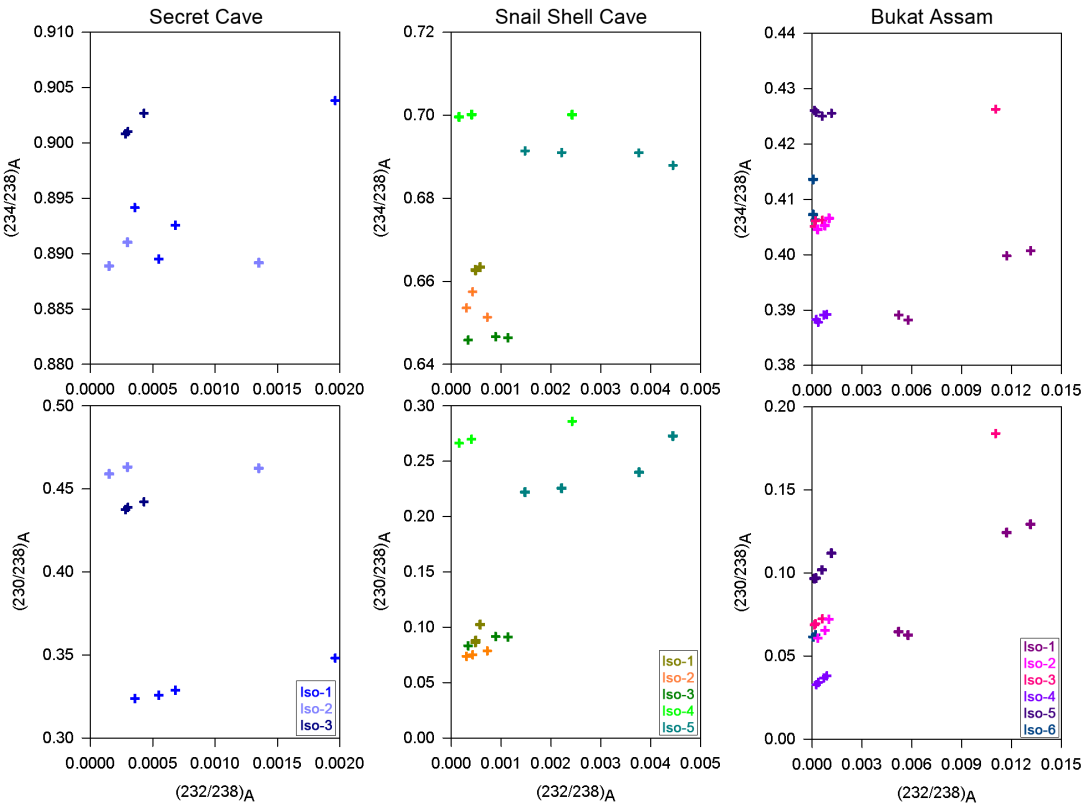

Figure B-S11. Osmond type isochrons for **(left)** Secret Cave at Gunung Mulu, **(middle)** Snail Shell Cave at Gunung Buda, and **(right)** Bukit Assam Cave at Gunung Buda. Colors distinguish measured isochrons at different depths (values for each listed in Table B-S2). Error ellipses are not shown because they are too small to be seen on this plot (see Table B-S2). The initial $^{230}Th/^{232}Th$ concentration is calculated using a maximum-likelihood estimation (MLE) XY-XZ isochron algorithm that finds the best line of fit to the set of XY ($^{230}Th/^{238}U$-$^{232}Th/^{238}U$) and XZ ($^{234}Th/^{238}U$-$^{232}Th/^{238}U$) points.

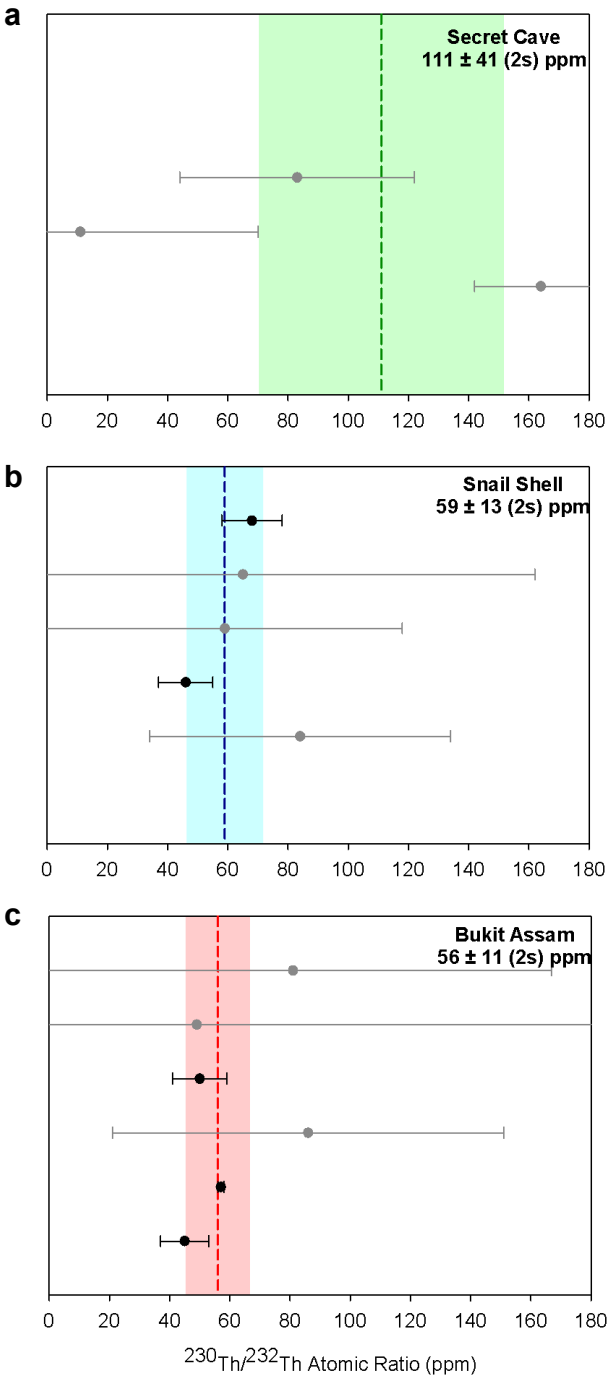

Figure B-S12. Plot of calculated initial $^{230}Th/^{232}Th$ concentration with 2σ error determined from each isochron, separated by cave: (a) Secret Cave (3 total), (b) Snail Shell Cave (5 total), and (c) Bukit Assam Cave (6 total). Black data points have 2σ error less than 10 ppm, gray data points have 2σ error greater than 10 ppm. Mean initial $^{230}Th/^{232}Th$ concentration plotted as colored dash line, with 2σ error shown as shaded rectangle. Note the colored 2σ error touches all black data

Table B-S1. Original U-Series calculated ages. Shading indicates isochrons. Data in red have been excluded from final age model (see Supp. Info.).

			MC-ICP-MS Measured Values								Uncorr	Calculated Age[b]		
Stal ID	Batch ID[a]	Core Depth (mm)	$[^{238}U]$ (ppb)	$[^{238}U]$ error (ppb)	$[^{232}Th]$ (pptr)	$[^{232}Th]$ error (pptr)	$\delta^{234}U_{(T)}$ (‰)	$\delta^{234}U_{(T)}$ error (‰)	$(^{230}Th/^{238}U)_A$	$(^{230}Th/^{238}U)_A$ error	Age (kybp)	Age (kybp)	2σ Error (-) (kyr)	2σ Error (+) (kyr)
SC03	ce10	10	114.3	0.1	150	9.2	-79.2	0.6	0.0992	0.0008	12.47	11.41	0.41	0.41
SC03	ck15	20.5	150.6	0.1	288	2.0	-69.0	0.6	0.1539	0.0005	19.77	18.25	0.57	0.56
SC03	ck09	27	117.7	0.1	29	2.4	-78.3	0.7	0.1819	0.0007	24.09	23.89	0.13	0.13
SC03	ci09	43	167.2	0.4	147	3.3	-111.9	3.0	0.2395	0.0020	34.55	33.81	0.47	0.46
SC03	cc19	58.5	174.4	0.1	239	5.8	-99.0	0.4	0.2749	0.0008	40.05	38.91	0.45	0.45
SC03	ci19	75	107.1	0.4	158	3.5	-107.2	5.1	0.2889	0.0034	43.06	41.83	0.82	0.83
SC03	cl11	84.5	115.2	0.1	141	4.1	-103.4	0.7	0.3028	0.0004	45.41	44.38	0.39	0.39
SC03	ci01	91.5	133.6	0.4	153	3.3	-128.6	3.8	0.3022	0.0026	47.06	46.07	0.67	0.67
SC03	cc15	103.5	128.8	0.1	140	5.0	-106.6	0.5	0.3235	0.0009	49.59	48.68	0.39	0.38
SC03	cc06	103.5	143.3	0.1	239	5.5	-111.2	0.7	0.3256	0.0008	50.37	48.95	0.56	0.55
SC03	cc08	103.5	158.8	0.1	330	4.9	-108.2	1.3	0.3285	0.0007	50.72	48.96	0.67	0.69
SC03	cc04	103.5	131.7	0.1	790	5.5	-96.9	0.7	0.3478	0.0009	53.65	48.58	1.98	1.93
SC03	ck23	125	157.6	0.1	234	1.8	-102.9	0.6	0.3556	0.0005	55.76	54.52	0.49	0.48
SC03	ci06	127	119.6	0.4	216	3.5	-96.9	4.5	0.3601	0.0031	56.15	54.64	0.92	0.94
SC03	ci17	147.5	133.9	0.4	241	3.4	-118.0	4.0	0.3730	0.0028	60.94	59.39	0.95	0.95
SC03	ck07	148.5	131.5	0.1	221	2.1	-120.0	0.6	0.3728	0.0006	61.11	59.66	0.57	0.54
SC03	ci12	168	131.4	0.5	254	3.8	-101.2	4.5	0.4146	0.0032	68.53	66.90	1.10	1.08
SC03	ck03	195	140.4	0.1	203	1.9	-93.7	0.6	0.4336	0.0006	72.10	70.89	0.48	0.47
SC03	cc14	201.5	211.0	0.1	245	4.9	-95.8	0.3	0.4386	0.0006	73.57	72.60	0.39	0.39
SC03	ci16	217	130.6	0.4	188	3.3	-92.4	4.0	0.4563	0.0029	77.47	76.26	1.01	1.01
SC03	ck11	237	191.4	0.1	87	1.9	-111.8	0.5	0.4586	0.0005	80.93	80.54	0.21	0.21
SC03	ck06	237	199.5	0.1	822	2.1	-111.6	0.5	0.4622	0.0005	81.86	78.29	1.37	1.34
SC03	ck01	237	215.3	0.1	194	2.1	-109.7	0.6	0.4628	0.0005	81.73	80.96	0.32	0.33
SC03	cd22	242.5	147.0	0.1	40	29.1	-107.3	0.6	0.4670	0.0012	82.49	82.26	0.40	0.39
SC03	cd12	252.5	147.2	0.1	99	30.6	-110.8	0.5	0.4720	0.0013	84.41	83.84	0.46	0.44
SC03	ck24	266	140.7	0.1	176	1.8	-101.5	0.6	0.4937	0.0005	88.88	87.82	0.42	0.44
SC03	ck04	270	139.2	0.1	428	1.9	-89.1	0.5	0.5078	0.0006	90.67	88.09	0.98	0.97
SC03	ci14	277.5	113.4	0.4	69	3.6	-109.0	4.9	0.4953	0.0036	90.69	90.16	1.41	1.41
SC03	ck21	279.5	116.4	0.1	69	2.0	-107.1	0.6	0.5009	0.0007	92.00	91.49	0.30	0.31
SC03	ce07	293.5	163.4	0.1	83	8.0	-108.1	0.5	0.5071	0.0006	94.00	93.57	0.27	0.27
SC03	ck20	294	141.0	0.1	75	1.9	-107.7	0.6	0.5043	0.0006	93.09	92.64	0.27	0.27
SC03	ci04	301.5	159.5	0.5	38	4.1	-102.4	4.0	0.5099	0.0029	93.75	93.55	1.17	1.18
SC03	ck18	302.5	150.1	0.1	83	2.1	-102.8	0.6	0.5110	0.0007	94.14	93.67	0.28	0.28
SC03	cd11	356.5	144.9	0.1	185	32.2	-89.6	0.5	0.5325	0.0014	97.99	96.93	0.63	0.62
SC03	ck10	381.5	119.3	0.1	65	1.9	-85.7	0.6	0.5424	0.0007	100.23	99.78	0.29	0.29

[a] Batch ID identifies Multi-Collector ICP-MS batch (2 letters) and sample run order within batch (1-24)

[b] 2σ errors are Monte Carlo derived, with the following initial 230/232 ratios: SCH02 = 59 ± 13 ppm; BA02 = 56 ± 11 ppm; SC03 and SC02 = 111 ± 41 ppm

Table B-S1. (cont'd)

			MC-ICP-MS Measured Values								Uncorr	Calculated Age[b]		
Stal ID	Batch ID[a]	Core Depth (mm)	$[^{238}U]$ (ppb)	$[^{238}U]$ error (ppb)	$[^{232}Th]$ (pptr)	$[^{232}Th]$ error (pptr)	$\delta^{234}U_{(T)}$ (‰)	$\delta^{234}U_{(T)}$ error (‰)	$(^{230}Th/^{238}U)_A$	$(^{230}Th/^{238}U)_A$ error	Age (kybp)	Age (kybp)	2σ Error (-) (kyr)	2σ Error (+) (kyr)
SC02	cd19	274	161.2	0.1	100	30.0	-94.8	0.6	0.2283	0.0011	**31.91**	**31.40**	**0.31**	**0.29**
SC02	cd03	280	169.3	0.1	238	30.0	-99.8	0.5	0.2686	0.0010	**38.97**	**37.80**	**0.51**	**0.47**
SC02	ck13	316	153.9	0.1	354	2.1	-106.5	0.5	0.3056	0.0005	**46.14**	**44.20**	**0.75**	**0.72**
SC02	ck02	338	111.2	0.1	86	1.9	-87.3	0.6	0.3245	0.0007	**48.36**	**47.73**	**0.27**	**0.27**
SC02	ck08	343	145.0	0.1	256	2.1	-109.2	0.5	0.3286	0.0005	**50.80**	**49.31**	**0.57**	**0.56**
SC02	cd01	371.5	127.4	0.1	137	32.3	-108.6	0.6	0.3494	0.0015	**54.98**	**54.07**	**0.52**	**0.49**
SC02	cd10	388.5	162.2	0.1	154	29.0	-118.2	0.5	0.3838	0.0011	**63.37**	**62.55**	**0.43**	**0.42**
SC02	ck16	412.5	130.6	0.1	98	2.1	-80.9	1.0	0.4233	0.0007	**68.17**	**67.55**	**0.30**	**0.30**
SC02	cj15	446	205.7	0.1	174	5.0	-100.0	0.5	0.4371	0.0004	**73.76**	**73.05**	**0.29**	**0.28**
SC02	cj23	446	208.5	0.1	194	6.2	-99.7	0.6	0.4384	0.0004	**74.04**	**73.25**	**0.32**	**0.32**
SC02	cj09	446	212.7	0.1	277	5.1	-98.0	0.5	0.4418	0.0004	**74.65**	**73.55**	**0.42**	**0.43**
SC02	ce04	472.5	176.4	0.1	54	8.1	-111.6	0.5	0.4590	0.0006	**81.02**	**80.76**	**0.21**	**0.19**
SC02	cl03	478	98.4	0.1	99	4.4	-91.4	1.0	0.5116	0.0006	**92.16**	**91.32**	**0.39**	**0.39**
SC02	cl14	581	105.2	0.1	67	5.2	-84.4	0.8	0.5428	0.0006	**100.10**	**99.57**	**0.31**	**0.32**
SC02	cl05	639	148.2	0.1	14	4.6	-111.5	0.6	0.5406	0.0005	**105.41**	**105.33**	**0.22**	**0.22**

[a] Batch ID identifies Multi-Collector ICP-MS batch (2 letters) and sample run order within batch (1-24)

[b] 2σ errors are Monte Carlo derived, with the following initial 230/232 ratios: SCH02 = 59 ± 13 ppm; BA02 = 56 ± 11 ppm; SC03 and SC02 = 111 ± 41 ppm

Table B-S1. (cont'd)

			MC-ICP-MS Measured Values								Uncorr	Calculated Age[b]		
Stal ID	Batch ID[a]	Core Depth (mm)	$[^{238}U]$ (ppb)	$[^{238}U]$ error (ppb)	$[^{232}Th]$ (pptr)	$[^{232}Th]$ error (pptr)	$\delta^{234}U_{(T)}$ (‰)	$\delta^{234}U_{(T)}$ error (‰)	$(^{230}Th/^{238}U)_A$	$(^{230}Th/^{238}U)_A$ error	Age (kybp)	Age (kybp)	2σ Error (-) (kyr)	2σ Error (+) (kyr)
SCH02	ca03	306.5	492.2	0.2	6174	3.8	-298.4	0.2	0.2109	0.0002	**40.19**	**32.62**	**1.73**	**1.72**
SCH02	cj04	318.5	598.1	0.3	7850	7.3	-317.8	0.3	0.2197	0.0002	**43.96**	**35.71**	**1.87**	**1.87**
SCH02	cj17	326.5	534.7	0.2	10510	7.4	-306.5	0.3	0.2781	0.0002	**58.66**	**46.06**	**2.88**	**2.90**
SCH02	cj14	340.5	694.5	0.3	1962	5.2	-331.3	0.3	0.1781	0.0001	**34.80**	**33.05**	**0.39**	**0.39**
SCH02	ca23	366.5	495.0	0.2	1956	11.5	-322.6	0.2	0.1906	0.0003	**37.15**	**34.73**	**0.54**	**0.54**
SCH02	ca09	393	688.9	0.3	1891	3.4	-333.6	0.2	0.1928	0.0002	**38.51**	**36.80**	**0.39**	**0.39**
SCH02	ca11	414	603.6	0.2	2758	3.2	-323.9	0.2	0.2086	0.0002	**41.67**	**38.84**	**0.61**	**0.62**
SCH02	cr04	428	603.6	0.2	1263	3.2	-312.5	0.3	0.2136	0.0004	**41.97**	**40.30**	**0.38**	**0.38**
SCH02	cr03	435	603.6	0.2	1409	2.7	-312.6	0.4	0.2147	0.0003	**42.25**	**40.59**	**0.37**	**0.37**
SCH02	ch15	441	545.5	0.2	2456	5.2	-309.1	0.3	0.2219	0.0019	**43.75**	**41.02**	**0.78**	**0.78**
SCH02	ch06	441	526.4	0.2	3551	5.6	-309.5	0.3	0.2254	0.0021	**44.64**	**40.52**	**1.06**	**1.07**
SCH02	ch19	441	510.6	0.2	6929	5.9	-312.6	0.2	0.2725	0.0019	**57.84**	**49.18**	**2.09**	**2.02**
SCH02	ch02	441	491.9	0.2	5650	6.2	-309.6	0.3	0.2398	0.0023	**48.39**	**41.25**	**1.74**	**1.68**
SCH02	ca20	457.5	640.0	0.3	1297	3.2	-328.1	0.2	0.2125	0.0002	**43.02**	**41.76**	**0.29**	**0.28**
SCH02	ca17	485	570.5	0.2	770	3.2	-332.4	0.2	0.2149	0.0002	**44.05**	**43.20**	**0.20**	**0.20**
SCH02	ca13	506.5	582.5	0.2	1382	3.4	-311.5	0.2	0.2335	0.0003	**46.92**	**45.47**	**0.33**	**0.33**
SCH02	ca24	514	590.1	0.3	1796	8.1	-316.1	0.8	0.2361	0.0004	**48.07**	**46.19**	**0.44**	**0.43**
SCH02	cj08	527.5	595.9	0.3	460	5.8	-329.5	0.3	0.2248	0.0002	**46.40**	**45.91**	**0.12**	**0.12**
SCH02	cj13	557.5	686.6	0.3	464	5.4	-332.7	0.2	0.2275	0.0002	**47.43**	**47.00**	**0.11**	**0.11**
SCH02	cj24	567	738.0	0.3	824	5.4	-332.4	0.3	0.2324	0.0001	**48.73**	**48.03**	**0.16**	**0.16**
SCH02	ca06	585	1053.7	0.4	1447	3.0	-334.6	0.2	0.2428	0.0002	**51.91**	**51.03**	**0.20**	**0.20**
SCH02	cj02	599	716.6	0.3	547	4.9	-318.3	0.3	0.2506	0.0002	**52.26**	**51.78**	**0.12**	**0.12**
SCH02	ci03	603.5	774.1	0.6	875	4.1	-324.6	0.8	0.2509	0.0005	**53.05**	**52.34**	**0.24**	**0.24**
SCH02	ca15	640	913.0	0.3	454	3.0	-327.6	0.2	0.2509	0.0002	**53.41**	**53.10**	**0.09**	**0.09**
SCH02	ca05	646	597.2	0.2	4414	4.1	-300.4	0.2	0.2857	0.0003	**60.10**	**55.54**	**1.03**	**1.03**
SCH02	ca22	646	546.5	0.2	676	3.3	-300.4	0.2	0.2693	0.0003	**55.39**	**54.65**	**0.18**	**0.18**
SCH02	ca04	646	595.3	0.2	279	3.2	-301.0	0.2	0.2661	0.0003	**54.58**	**54.29**	**0.10**	**0.10**
SCH02	cj10	670	800.0	0.3	1448	5.1	-334.0	0.2	0.2582	0.0002	**56.37**	**55.20**	**0.26**	**0.26**
SCH02	cj16	674	656.9	0.3	1186	5.0	-339.7	0.3	0.2569	0.0002	**56.72**	**55.55**	**0.27**	**0.27**
SCH02	cb07	714	991.3	0.5	1708	3.4	-337.4	0.3	0.2649	0.0003	**58.87**	**57.74**	**0.27**	**0.26**
SCH02	cb05	734	866.8	0.5	404	3.6	-293.1	0.4	0.2852	0.0002	**58.97**	**58.69**	**0.11**	**0.11**
SCH02	cb13	742	745.8	0.4	654	3.4	-292.0	0.4	0.2890	0.0005	**59.91**	**59.39**	**0.19**	**0.19**
SCH02	ci07	758	883.2	0.6	331	3.7	-295.8	0.6	0.2868	0.0004	**59.78**	**59.56**	**0.16**	**0.16**
SCH02	ci13	765	788.9	0.6	569	4.2	-310.0	0.8	0.2847	0.0006	**61.10**	**60.65**	**0.22**	**0.23**
SCH02	cb16	780	780.1	0.5	217	3.5	-299.9	0.5	0.2921	0.0002	**61.91**	**61.74**	**0.10**	**0.11**
SCH02	cb02	849	717.9	0.5	433	3.9	-301.7	0.5	0.2985	0.0003	**64.11**	**63.74**	**0.15**	**0.14**
SCH02	cb08	877	700.1	0.4	814	3.4	-327.7	0.4	0.3104	0.0004	**72.41**	**71.65**	**0.24**	**0.23**
SCH02	cb12	897	792.0	0.4	818	3.3	-321.6	0.4	0.3183	0.0005	**74.03**	**73.36**	**0.23**	**0.24**

[a] Batch ID identifies Multi-Collector ICP-MS batch (2 letters) and sample run order within batch (1-24)

[b] 2σ errors are Monte Carlo derived, with the following initial 230/232 ratios: SCH02 = 59 ± 13 ppm; BA02 = 56 ± 11 ppm; SC03 and SC02 = 111 ± 41 ppm

Table B-S1. (cont'd)

			MC-ICP-MS Measured Values								Uncorr	Calculated Age[b]		
Stal ID	Batch ID[a]	Core Depth (mm)	$[^{238}U]$ (ppb)	$[^{238}U]$ error (ppb)	$[^{232}Th]$ (pptr)	$[^{232}Th]$ error (pptr)	$\delta^{234}U_{(T)}$ (‰)	$\delta^{234}U_{(T)}$ error (‰)	$(^{230}Th/^{238}U)_A$	$(^{230}Th/^{238}U)_A$ error	Age (kybp)	Age (kybp)	2σ Error (-) (kyr)	2σ Error (+) (kyr)
BA02	cb17	129	984.1	0.5	296	3.4	-598.4	0.2	0.0514	0.0001	**15.50**	**15.20**	**0.07**	**0.07**
BA02	cj19	147.5	1112.3	0.5	592	5.2	-600.3	0.2	0.0543	0.0001	**16.55**	**16.02**	**0.11**	**0.11**
BA02	ch10	184	1295.5	0.5	183	4.7	-586.7	0.1	0.0614	0.0008	**18.29**	**18.15**	**0.25**	**0.26**
BA02	ch18	184	1280.1	0.5	272	5.0	-593.1	0.1	0.0612	0.0008	**18.57**	**18.36**	**0.29**	**0.29**
BA02	ch16	184	1220.7	0.5	752	4.8	-594.1	0.1	0.0628	0.0008	**19.16**	**18.55**	**0.31**	**0.31**
BA02	ch03	184	1167.9	0.5	2075	5.3	-592.8	0.2	0.0811	0.0009	**25.75**	**23.93**	**0.50**	**0.50**
BA02	cb10	215	1173.6	0.6	432	3.5	-587.5	0.2	0.0686	0.0001	**20.81**	**20.45**	**0.09**	**0.09**
BA02	cb15	251	1099.6	0.5	496	3.4	-590.0	0.2	0.0717	0.0001	**22.07**	**21.62**	**0.10**	**0.10**
BA02	cb18	278	942.0	0.5	767	5.8	-583.6	0.3	0.0815	0.0001	**25.16**	**24.36**	**0.17**	**0.17**
BA02	cb01	283	943.2	0.5	779	3.5	-583.7	0.2	0.0828	0.0001	**25.66**	**24.83**	**0.17**	**0.17**
BA02	cj21	315	1249.8	0.5	552	4.7	-574.4	0.2	0.0911	0.0001	**27.94**	**27.51**	**0.09**	**0.09**
BA02	cg03	353	1192.8	0.5	492	5.8	-574.3	0.2	0.0970	0.0008	**30.20**	**29.79**	**0.31**	**0.31**
BA02	cg20	353	1194.5	0.6	817	6.7	-574.6	0.3	0.0975	0.0009	**30.39**	**29.72**	**0.36**	**0.37**
BA02	cg21	353	1272.2	0.6	2342	6.6	-575.3	0.3	0.1023	0.0008	**32.35**	**30.50**	**0.48**	**0.49**
BA02	cg09	353	1197.1	0.6	4238	7.2	-574.8	0.3	0.1124	0.0009	**36.44**	**32.80**	**0.81**	**0.81**
BA02	cb04	397.5	1228.4	0.6	446	3.6	-567.4	0.2	0.1042	0.0001	**32.28**	**31.92**	**0.09**	**0.09**
BA02	cc03	411.8	998.6	0.4	1520	5.6	-565.3	0.1	0.1093	0.0001	**34.03**	**32.53**	**0.30**	**0.30**
BA02	cc07	425.3	1092.8	0.4	1510	5.4	-564.3	0.1	0.1106	0.0001	**34.46**	**33.10**	**0.27**	**0.27**
BA02	cc13	432	986.5	0.4	840	5.5	-564.4	0.1	0.1109	0.0003	**34.58**	**33.74**	**0.20**	**0.20**
BA02	cj06	463.5	1002.0	0.5	915	5.6	-560.9	0.2	0.1175	0.0001	**36.79**	**35.89**	**0.18**	**0.18**
BA02	cc18	488	989.9	0.4	644	5.3	-556.1	0.1	0.1227	0.0001	**38.34**	**37.70**	**0.13**	**0.14**
BA02	cc10	495.5	1045.2	0.4	3593	5.4	-557.0	0.1	0.1310	0.0001	**41.93**	**38.49**	**0.68**	**0.68**
BA02	cc01	512.5	1077.2	0.4	1014	5.2	-554.9	0.1	0.1286	0.0001	**40.60**	**39.68**	**0.19**	**0.19**
BA02	cc11	516	1041.0	0.4	670	5.3	-554.6	0.1	0.1279	0.0001	**40.26**	**39.63**	**0.14**	**0.14**
BA02	cj11	539	1078.8	0.4	2014	5.0	-551.0	0.2	0.1368	0.0001	**43.52**	**41.68**	**0.37**	**0.36**
BA02	cb20	565.5	1487.8	0.7	360	4.6	-550.1	0.3	0.1366	0.0001	**43.31**	**43.07**	**0.08**	**0.08**
BA02	cj20	580	1036.6	0.4	3226	5.3	-548.3	0.2	0.1444	0.0001	**46.45**	**43.35**	**0.63**	**0.61**
BA02	cj07	595	1275.8	0.5	463	4.8	-547.4	0.1	0.1419	0.0001	**45.21**	**44.85**	**0.09**	**0.08**

[a] Batch ID identifies Multi-Collector ICP-MS batch (2 letters) and sample run order within batch (1-24)

[b] 2σ errors are Monte Carlo derived, with the following initial 230/232 ratios: SCH02 = 59 ± 13 ppm; BA02 = 56 ± 11 ppm; SC03 and SC02 = 111 ± 41 ppm

Table B-S2. Osmond-type activity ratios used in isochron calculations. Plotted in Figure S12 by cave type.

Cave	Stal ID	Isochron No.	Batch ID	$(232/238)_A$	2σ error	$(230/238)_A$	2σ error	$(234/238)_A$	2σ error
Bukat	BA04	Iso-1	sc02	5.21E-03	6.12E-06	6.47E-02	4.02E-04	3.89E-01	3.26E-04
Assam	BA04		sc03	5.77E-03	8.21E-06	6.25E-02	3.23E-04	3.88E-01	2.80E-04
	BA04		sc04	1.17E-02	1.46E-05	1.24E-01	3.25E-04	4.00E-01	2.60E-04
	BA04		sc05	1.32E-02	1.87E-05	1.29E-01	4.79E-04	4.01E-01	2.17E-04
	BA04	Iso-2	sd06	3.38E-04	1.09E-07	6.06E-02	1.33E-04	4.05E-01	8.22E-04
	BA04		sd07	7.66E-04	3.10E-07	6.54E-02	1.66E-04	4.05E-01	8.79E-04
	BA04		sd08	1.01E-03	3.08E-07	7.21E-02	1.57E-04	4.07E-01	8.59E-04
	BA04	Iso-3	sc09	1.10E-02	8.48E-06	1.84E-01	2.48E-04	4.26E-01	1.85E-04
	BA04		sc10	6.18E-04	6.37E-07	7.23E-02	2.17E-04	4.06E-01	2.06E-04
	BA04		sc11	1.39E-04	3.20E-07	6.88E-02	2.23E-04	4.05E-01	2.24E-04
	BA04		sc12	1.91E-04	4.25E-07	6.94E-02	2.68E-04	4.06E-01	2.07E-04
	BA04	Iso-4	sg20	6.92E-04	8.46E-07	3.68E-02	7.05E-05	3.89E-01	1.47E-04
	BA04		sg23	2.51E-04	8.19E-07	3.27E-02	7.01E-05	3.88E-01	1.54E-04
	BA04		sg36	3.59E-04	7.70E-07	3.39E-02	6.47E-05	3.88E-01	1.58E-04
	BA04		sg15	8.89E-04	1.15E-06	3.80E-02	8.85E-05	3.89E-01	1.65E-04
	BA02	Iso-5	cg03*	1.35E-04	2.02E-06	9.65E-02	3.51E-03	4.26E-01	2.48E-04
	BA02		cg20*	2.24E-04	2.30E-06	9.69E-02	3.99E-03	4.26E-01	2.71E-04
	BA02		cg21*	6.03E-04	2.14E-06	1.02E-01	3.69E-03	4.25E-01	2.63E-04
	BA02	Iso-6	ch10*	4.62E-05	1.18E-06	6.15E-02	7.55E-04	4.14E-01	1.46E-04
	BA02		ch18*	6.95E-05	1.28E-06	6.13E-02	8.18E-04	4.07E-01	1.43E-04
	BA02		ch16*	2.02E-04	1.28E-06	6.28E-02	8.21E-04	4.06E-01	1.39E-04
Snail	SCH02	Iso-1	se17	1.81E-04	7.14E-07	8.79E-02	1.20E-04	6.63E-01	2.07E-04
Shell	SCH02		se18	1.24E-04	6.55E-07	8.63E-02	1.07E-04	6.63E-01	1.95E-04
	SCH02		se19	1.40E-03	8.83E-07	1.03E-01	1.16E-04	6.63E-01	2.35E-04
	SCH02	Iso-2	se20	7.19E-04	8.67E-07	7.87E-02	1.38E-04	6.51E-01	2.68E-04
	SCH02		se21	3.05E-04	7.19E-07	7.39E-02	9.99E-05	6.54E-01	2.25E-04
	SCH02		se22	4.30E-04	7.48E-07	7.53E-02	1.08E-04	6.58E-01	2.67E-04
	SCH02	Iso-3	se23	1.14E-03	5.59E-07	9.13E-02	8.77E-05	6.46E-01	1.97E-04
	SCH02		se24	3.38E-04	4.44E-07	8.32E-02	8.46E-05	6.46E-01	2.20E-04
	SCH02		se25	8.89E-04	4.81E-07	9.15E-02	8.58E-05	6.47E-01	2.34E-04
	SCH02	Iso-4	ca05*	2.42E-03	2.03E-06	2.86E-01	3.28E-04	7.00E-01	2.30E-04
	SCH02		ca22*	4.05E-04	1.96E-06	2.70E-01	3.19E-04	7.00E-01	2.02E-04
	SCH02		ca04*	1.54E-04	1.76E-06	2.66E-01	3.14E-04	7.00E-01	2.38E-04
	SCH02	Iso-5	ch15*	1.48E-03	3.05E-06	2.22E-01	1.92E-03	6.91E-01	2.78E-04
	SCH02		ch06*	2.21E-03	3.34E-06	2.26E-01	2.07E-03	6.91E-01	2.59E-04
	SCH02		ch19*	4.45E-03	1.01E-05	2.73E-01	2.03E-03	6.88E-01	2.71E-03
	SCH02		ch02*	3.76E-03	3.78E-06	2.40E-01	2.29E-03	6.91E-01	3.12E-04
Secret	SC03	Iso-1	cc15*	3.56E-04	1.27E-05	3.24E-01	8.55E-04	8.94E-01	5.36E-04
	SC03		cc06*	5.48E-04	1.27E-05	3.26E-01	8.49E-04	8.90E-01	6.51E-04
	SC03		cc08*	6.81E-04	1.01E-05	3.29E-01	7.19E-04	8.93E-01	1.27E-03
	SC03		cc04*	1.96E-03	1.38E-05	3.48E-01	9.18E-04	9.04E-01	6.66E-04
	SC03	Iso-2	cc15*	1.49E-04	3.31E-06	4.59E-01	4.83E-04	8.89E-01	4.86E-04
	SC03		cc06*	1.35E-03	3.39E-06	4.62E-01	5.05E-04	8.89E-01	4.81E-04
	SC03		cc08*	2.96E-04	3.18E-06	4.63E-01	4.50E-04	8.91E-01	5.78E-04
	SC02	Iso-3	cc15*	2.77E-04	7.95E-06	4.37E-01	3.94E-04	9.01E-01	5.41E-04
	SC02		cc06*	3.04E-04	9.72E-06	4.39E-01	4.14E-04	9.01E-01	5.98E-04
	SC02		cc08*	4.27E-04	7.83E-06	4.42E-01	3.90E-04	9.03E-01	5.31E-04

(*) indicates new isochrons not previously published.

Table B-S3. Calculation of detrital 230/232 concentration for each cave system (BA02 and BA04; SCH02; SSC01; and SC03). Final detrital 230/232 concentration used for each stalagmite is: BA02 = 56 ± 11 ppm; SCH02 = 59 ± 13 ppm; SC03 and SC02 = 111 ± 41 ppm (see Supp. Info.).

		Osmond Type[b]									Detrital 230/232 (ppm)			
Stal ID	Isochron[a]	Age (kyr)	2σ error (kyr)	$(230/238)_A$ Intercept	2σ error	$(234/238)_A$ Intercept	2σ error	Detrital 230/232 (ppm)	2σ error (ppm)	Weight[c]	Wtd Mean	Wtd 2σ[d]	Un-wtd Mean	Un-wtd 2σ[e]
BA04	Iso-1	3.6	4.5	0.0120	0.0150	0.3800	0.0110	50	9	0.2313	**56**	1	**62**	35
	Iso-2	16.5	3.7	0.0547	0.0083	0.4040	0.0510	86	65	0.0308				
	Iso-3	20.5	0.5	0.0667	0.0013	0.4052	0.0011	57	1	1.4800				
	Iso-4	9.2	0.3	0.0308	0.0008	0.3875	0.0017	45	8	0.2643				
BA02	Iso-5*	28.8	4.1	0.0940	0.0110	0.4258	0.0008	81	86	0.0231				
	Iso-6*	18.0	23.0	0.0610	0.0670	0.4130	0.0130	49	2973	0.0007				
SCH02	Iso-1	15.1	0.3	0.0852	0.0015	0.6626	0.0027	68	10	0.1947	**59**	4	**64**	27
	Iso-2	12.4	1.7	0.0703	0.0085	0.6570	0.0180	65	97	0.0206				
	Iso-3	14.6	2.0	0.0800	0.0095	0.6460	0.0240	59	59	0.0336				
	Iso-4*	54.1	0.7	0.2656	0.0024	0.6999	0.0017	46	9	0.2313				
	Iso-5*	37.0	6.8	0.1950	0.0290	0.6917	0.0050	84	50	0.0398				
SC03	Iso-1*	48.7	1.5	0.3181	0.0074	0.8892	0.0056	83	39	0.0507	**111**	11	**86**	153
	Iso-2*	80.9	2.6	0.4607	0.0084	0.8898	0.0092	11	59	0.0336				
SC02	Iso-3*	71.9	0.4	0.4293	0.0014	0.8970	0.0017	164	22	0.0925				

[a] (*) indicates new isochrons not previously published.

[b] Age, intercepts, and detrital 230/232 calculated using ISOPLOT 3.72 (Ludwig, 1993). The 230/238 and 234/238 intercepts are the Y-Z plane intercepts of the linear 3-D isochron used to calculate an age and initial 234/238 using X = 232/238, Y = 230/238, Z = 234/238 (Ludwig and Titterington, 1994).

[c] Weights calculated as inverse of 1 standard deviation of the detrital 230/232 for each isochron.

[d] Weighted standard deviation is the inverse of the sum of the weights for each cave system.

[e] Un-weighted standard deviation is the standard deviation of the *n*-isochron 230/232 for each cave system.

Table B-S4. Adjusted age model for SC03, SC02, SCH02, and BA02 used in Figure 4.2. Adjusted age is within limits in all cases.

Stal ID	Batch ID	Core Depth (mm)	Lower Age (2s)[a] (ybp)	Original Age[a] (ybp)	Adjusted Age (ybp)	Upper Age (2s)[a] (ybp)	Growth Rate[b] (year/mm)
SC03	ck09	27	23,758	23,889	23,889	24,017	
SC03	ci09	43	33,343	33,811	33,811	34,267	--hiatus--
SC03	cc19	58.5	38,462	38,910	38,910	39,356	329
SC03	ci19	75	41,007	41,828	41,828	42,656	177
SC03	cl11	84.5	43,992	44,381	44,381	44,773	269
SC03	ci01	91.5	45,406	46,075	46,075	46,749	242
SC03	cc15	103.5	48,294	48,679	48,679	49,058	217
SC03	ck23	125	54,030	54,515	54,515	55,000	271
SC03	ck07	148.5	59,092	59,657	59,657	60,200	219
SC03	ci12	168	65,803	66,898	66,898	67,976	371
SC03	ck03	195	70,417	70,893	71,353	71,359	165
SC03	cc14	201.5	72,213	72,602	72,902	72,988	238
SC03	ci16	217	75,258	76,265	76,265	77,271	217
SC03	ck11	237	80,338	80,543	80,543	80,749	214
SC03	cd22	242.5	81,863	82,261	82,261	82,651	312
SC03	cd12	252.5	83,375	83,835	83,835	84,275	157
SC03	ck24	266	87,404	87,823	87,523	88,261	273
SC03	ck04	270	87,113	88,092	88,592	89,059	267
SC03	ck21	279.5	91,188	91,491	91,391	91,803	295
SC03	ck20	294	92,368	92,637	92,837	92,907	100
SC03	ck18	302.5	93,389	93,673	93,673	93,957	98
SC03	cd11	356.5	96,300	96,926	97,326	97,542	68
SC03	ck10	381.5	99,482	99,776	99,776	100,069	98
SC02	cd03	280	37,290	37,799	37,799	38,274	
SC02	ck13	316	43,451	44,198	44,198	44,916	178
SC02	ck02	338	47,461	47,731	47,731	47,997	161
SC02	ck08	343	48,741	49,309	49,309	49,868	316
SC02	cd01	371.5	53,544	54,068	54,068	54,554	167
SC02	cd10	388.5	62,119	62,552	62,552	62,972	169/ hiatus/ 214
SC02	ck16	412.5	67,256	67,554	67,554	67,851	208
SC02	cj15	446	72,760	73,054	73,054	73,339	164
SC02	ce04	472.5	80,549	80,758	80,758	80,951	194 / hiatus
SC02	cl03	478	90,935	91,322	91,322	91,709	hiatus / 80
SC02	cl14	581	99,257	99,569	99,569	99,887	80
SC02	cl05	639	105,115	105,333	105,333	105,551	99

[a] Original calculated age with upper and lower limits (95% confidence interval calculated using Monte Carlo simulation)

[b] Linear growth rates for each interval between 2 consecutive U-series dates that do not include a hiatus. If a hiatus exists between two U-series dates, growth rate was assigned the same growth rate as adjacent age models either above or below (use of linear extrapolation)

Table B-S4. (cont'd)

Stal ID	Batch ID	Core Depth (mm)	Lower Age (2s)[a] (ybp)	Original Age[a] (ybp)	Adjusted Age (ybp)	Upper Age (2s)[a] (ybp)	Growth Rate[b] (year/mm)
SCH02	cj14	340.5	32,666	33,052	32,852	33,440	
SCH02	ca23	366.5	34,185	34,729	34,529	35,268	64
SCH02	ca09	393	36,408	36,797	36,497	37,182	74
SCH02	ca11	414	38,226	38,837	38,537	39,455	97
SCH02	cr04	428	39,923	40,298	39,998	40,681	104
SCH03	cr03	435	40,226	40,591	40,291	40,958	42
SCH02	ch15	441	40,234	41,017	40,417	41,794	21
SCH02	ca20	457.5	41,466	41,759	41,759	42,042	81
SCH02	ca17	485	43,008	43,205	43,205	43,401	53
SCH02	ca13	506.5	45,143	45,471	45,471	45,797	105
SCH02	cj08	527.5	45,790	45,913	45,913	46,036	21
SCH02	cj13	557.5	46,891	47,004	47,004	47,112	36
SCH02	cj24	567	47,863	48,026	47,926	48,190	97
SCH02	ca06	585	50,838	51,034	51,034	51,235	--hiatus--
SCH02	cj02	599	51,664	51,782	51,782	51,901	53
SCH02	ci03	603.5	52,105	52,343	52,113	52,579	74
SCH02	ca15	640	53,007	53,098	53,098	53,187	27
SCH02	ca04	646	54,193	54,293	54,293	54,391	--hiatus--
SCH02	cj10	670	54,940	55,204	55,204	55,465	38
SCH02	cj16	674	55,281	55,547	55,547	55,818	86
SCH02	cb07	714	57,476	57,743	57,743	58,004	55
SCH02	cb05	734	58,581	58,691	58,691	58,798	47
SCH02	cb13	742	59,201	59,388	59,208	59,574	65
SCH02	ci07	758	59,393	59,556	59,716	59,718	32
SCH02	ci13	765	60,428	60,652	60,432	60,880	102
SCH02	cb16	780	61,635	61,740	61,640	61,845	81
SCH02	cb02	849	63,597	63,742	63,887	63,887	33
SCH02	cb08	877	71,412	71,649	71,649	71,879	--hiatus--
SCH02	cb12	897	73,127	73,359	73,359	73,594	86
BA02	cb17	129	15,135	15,200	15,200	15,268	
BA02	cj19	147.5	15,912	16,020	16,020	16,126	44
BA02	ch10	184	17,900	18,153	18,153	18,411	58
BA02	cb10	215	20,364	20,450	20,450	20,537	74
BA02	cb15	251	21,524	21,622	21,622	21,718	33
BA02	cb18	278	24,189	24,355	24,355	24,525	101
BA02	cb01	283	24,668	24,833	24,833	25,005	96
BA02	cj21	315	27,422	27,511	27,511	27,600	84
BA02	cg03	353	29,478	29,792	29,792	30,101	60
BA02	cb04	397.5	31,836	31,925	31,925	32,013	48
BA02	cc03	411.8	32,233	32,533	32,533	32,833	43
BA02	cc07	425.3	32,833	33,104	33,104	33,377	42
BA02	cc13	432	33,539	33,742	33,742	33,942	95
BA02	cj06	463.5	35,710	35,894	35,894	36,074	68
BA02	cc18	488	37,571	37,704	37,704	37,842	74
BA02	cc10	495.5	37,812	38,492	38,492	39,171	105
BA02	cc01	512.5	39,484	39,677	39,527	39,870	61
BA02	cc11	516	39,495	39,631	39,761	39,771	67
BA02	cj11	539	41,307	41,679	41,679	42,040	83
BA02	cb20	565.5	42,997	43,075	43,075	43,152	53
BA02	cj20	580	42,723	43,348	43,748	43,954	46
BA02	cj07	595	44,768	44,853	44,853	44,936	74

[a] Original calculated age with upper and lower limits (95% confidence interval calculated using Monte Carlo simulation)

[b] Linear growth rates for each interval between 2 consecutive U-series dates that do not include a hiatus. If a hiatus exists between two U-series dates, growth rate was assigned the same growth rate as adjacent age models either above or below (use of linear extrapolation)

APPENDIX C:

SUPPLEMENTARY MATERIALS FOR

"0-160KYBP MULTI-STALAGMITE $\delta^{18}O$ RECORD FROM NORTHERN BORNEO "

1. Gunung Mulu National Park hydroclimate and karst

SC03, WR12-01, WR12-12, FC12-12, FC12-14, and FC12-15 were collected from Gunung Mulu and Gunung Buda National Parks (4°N, 115°E) (Fig. C-S1). An outcrop of Melanau limestone, covered with dense tropical rainforest, forms a band of hills on the eastern shale and sandstone slopes of 2375 m high Gunung Mulu (Figure C-S1), and receives over 5 m of rainfall per year percolating into the rock and throughout the vast cave chambers (295 km explored).

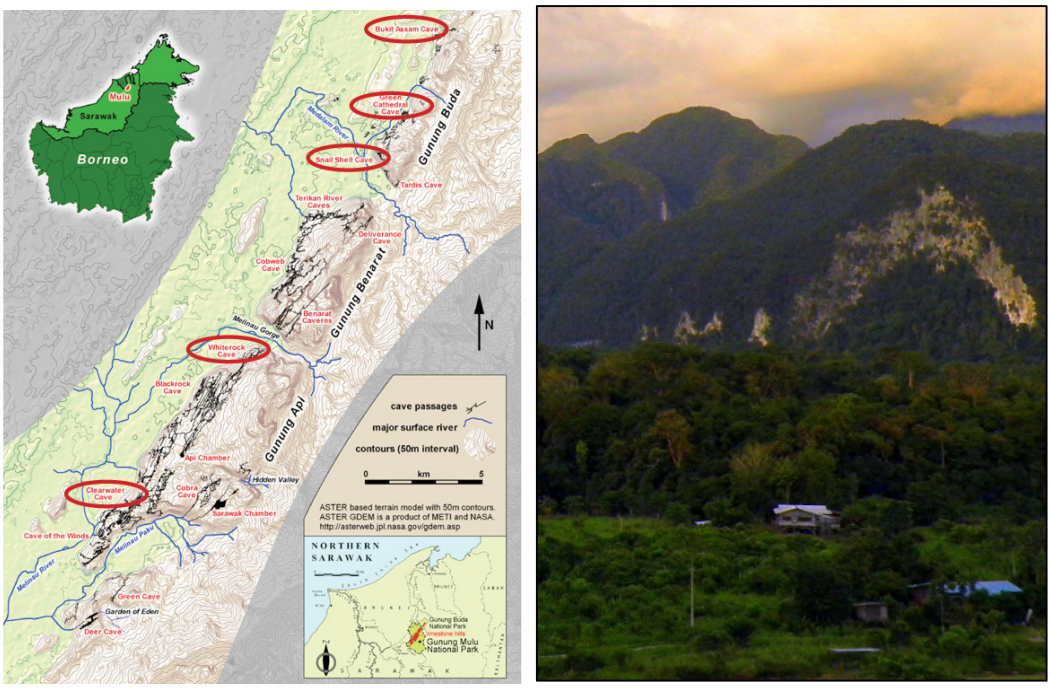

Fig. C-S1. (left) Caves of Gunung Mulu National Park with cave study sites indicated. From *J. Wooldridge and T. Waltham, in Encyclopedia of Caves 2nd Ed. (2012)* (right) View looking eastward toward Gunung Api *(Credit: Syria Lejau)*

2. U/Th ICP-MS measurements

Measured $[^{238}U]$, $[^{232}Th]$, $\delta^{234}U$, $(^{230}Th/^{238}U)_A$, and $(^{230}Th/^{232}U)_A$ are reported in Table S1 for all samples in this study.

Table C-S1. Original U-Series calculated ages used in this study. Shading indicates isochrons. (*) indicates ages included in final age model.

Stal	sample	Distance mm	U238 conc ppb	U238 conc error	232Th pmol/g	232Th error	d234U(T) ‰	d234U(T) error ‰	230Th/238U activity	230Th/238U activity error	232Th/238U activity	232Th/238U activity error	Uncorr	Monte Carlo Cor Age (years)	Error Minus	Error Plus		init d234U
SC03	ck10	381.5	119.3	0.1	0.28	0.01	-87.1	0.6	0.5432	6.54E-04	1.78E-04	5.21E-06	100604	100151	530	521	*	-115.5
SC03	ct02	397.5	130.0	0.1	0.40	0.02	-101.7	0.7	0.5446	4.75E-04	2.34E-04	8.87E-06	104297	103687	498	500	*	-136.3
SC03	cl10	430	147.9	0.1	0.11	0.02	-115.2	0.7	0.5404	5.70E-04	5.48E-05	1.01E-05	106078	105932	522	502	*	-155.4
SC03	ct03	454	143.5	0.1	0.84	0.02	-127.3	0.7	0.5434	5.38E-04	4.44E-04	8.73E-06	110190	108977	683	694	*	-173.2
SC03	cs01	476	102.7	0.1	0.31	0.01	-95.1	1.3	0.5823	9.22E-04	2.26E-04	6.83E-06	115655	115070	1007	1038	*	-131.6
SC03	cs02	505	88.5	0.1	0.14	0.01	-93.5	1.6	0.5917	1.11E-03	1.18E-04	8.41E-06	118679	118376	1196	1265	*	-130.6
SC03	cs03	522	122.3	0.1	0.18	0.01	-91.0	1.2	0.5960	8.26E-04	1.11E-04	5.98E-06	119570	119283	935	921		-127.4
SC03	ct04	533.5	127.2	0.1	0.09	0.02	-85.1	0.8	0.5956	6.20E-04	5.59E-05	1.07E-05	117732	117590	620	628		-118.6
SC03	cs04	541	109.4	0.1	0.21	0.01	-76.9	1.3	0.6368	9.69E-04	1.49E-04	6.57E-06	131110	130733	1206	1169		-111.2
SC03	ct05	556.5	101.3	0.1	0.05	0.01	-80.4	0.8	0.6077	5.89E-04	3.79E-05	1.02E-05	120895	120799	629	632		-113.1
SC03	cr05	576	107.6	0.1	0.05	0.01	-93.7	1.4	0.5974	1.36E-03	3.77E-05	7.93E-06	120872	120775	1283	1334		-131.7
SC03	cr01	594	95.2	0.1	0.03	0.01	-71.6	1.4	0.6232	1.61E-03	2.53E-05	9.89E-06	124105	124042	1447	1535		-101.6
SC03	cl18	642.5	90.3	0.1	0.08	0.02	-51.4	0.9	0.6432	6.84E-04	6.32E-05	1.77E-05	125624	125470	728	724		-73.3
FC12-14	co13	19	190.7	0.1	1.25	0.08	-124.7	0.7	0.4303	3.46E-04	4.97E-04	3.12E-05	75327	74397	581	562	*	-153.9
FC12-14	cp18	166	70.9	0.1	1.19	0.02	-146.4	0.9	0.4708	7.86E-04	1.27E-03	2.18E-05	90269	87774	1476	1437	*	-187.5
FC12-14	cs21	207	54.3	0.1	1.69	0.01	-73.2	3.1	0.6526	1.98E-03	2.36E-03	1.67E-05	136439	132195	3537	3677		-106.3
FC12-14	cp19	216.5	64.1	0.1	0.29	0.03	-111.0	1.3	0.6071	1.27E-03	3.48E-04	3.33E-05	130301	129645	1455	1466	*	-160.0
FC12-14	cx01	227.75	51.2	0.1	2.48	0.00	-88.2	3.2	0.6414	1.02E-03	3.68E-03	6.35E-06	137033	130164	4624	4374	*	-127.3
FC12-14	cx02	239.5	51.4	0.1	2.06	0.00	-111.7	2.7	0.6319	1.33E-03	3.05E-03	7.19E-06	141826	135918	4112	4031	*	-163.9
FC12-14	ct08	247	57.5	0.1	1.27	0.01	-142.9	1.2	0.6062	8.14E-04	1.68E-03	1.71E-05	142402	138988	2298	2265	*	-211.6
FC12-14	ct09	261	58.6	0.1	1.79	0.01	-146.3	1.3	0.6133	9.45E-04	2.32E-03	1.91E-05	147680	142895	3079	3043	*	-219.0
FC12-14	cs22	270.75	36.6	0.1	1.44	0.01	-106.5	4.6	0.6560	2.80E-03	2.99E-03	2.41E-05	151616	145848	5833	6281	*	-160.7
FC12-14	ct10	275.5	44.0	0.1	4.15	0.01	-95.5	1.6	0.7019	1.09E-03	7.16E-03	2.40E-05	172059	157860	8745	8083		-149.1
FC12-14	cx03	294.5	53.4	0.0	1.65	0.00	-113.5	0.6	0.6642	6.59E-04	2.35E-03	5.62E-06	159657	155061	2730	2652		-175.9
FC12-14	ct11	311.5	82.9	0.1	1.50	0.01	-141.3	0.8	0.6337	6.70E-04	1.37E-03	1.20E-05	156660	153852	2005	1901	*	-218.1
FC12-14	cx05	324.5	86.5	0.0	0.80	0.00	-131.7	0.5	0.6480	6.04E-04	6.98E-04	3.90E-06	159939	158543	1161	1142	*	-206.0
FC12-14	cn19	332.25	79.3	0.2	1.26	0.02	-165.9	2.4	0.6252	1.58E-03	1.21E-03	1.95E-05	165691	163068	3900	4187	*	-262.9
FC12-12	co07	14.8	368.0	0.2	2.94	0.08	-349.3	0.4	0.2443	1.59E-04	6.07E-04	1.74E-05	54041	52418	879	881		-405.0
FC12-12	cs14		329.2	0.2	2.34	0.01	-392.4	0.6	0.2687	3.20E-04	5.40E-04	2.69E-06	69321	67685	950	923		-474.9
FC12-12	cp01	124.9	294.7	0.1	0.79	0.02	-330.1	0.3	0.3430	2.61E-04	2.03E-04	5.07E-06	85217	84663	392	387		-419.2
FC12-12	cp20	153.8	183.4	0.1	0.96	0.02	-319.1	0.4	0.3948	3.77E-04	3.98E-04	8.57E-06	105410	104307	770	743		-428.3
FC12-12	cu14	223.8	277.3	0.2	1.60	0.00	-282.5	0.6	0.4304	3.33E-04	4.38E-04	9.04E-07	110076	108948	817	810	*	-384.2
FC12-12	cx10	240.8	196.3	0.1	0.66	0.00	-294.5	0.2	0.4285	2.84E-04	2.55E-04	1.28E-06	113558	112879	504	490	*	-405.0
FC12-12	cx06	258.3	134.6	0.1	0.29	0.00	-271.7	0.3	0.4512	3.38E-04	1.65E-04	2.07E-06	116434	116016	461	475	*	-376.9
FC12-12	cx07	258.3	225.2	0.1	0.42	0.00	-268.7	0.2	0.4532	3.02E-04	1.42E-04	1.46E-06	116334	115975	397	400		-372.7
FC12-12	cx09	258.3	142.4	0.1	0.55	0.00	-268.2	0.3	0.4555	3.99E-04	2.96E-04	2.22E-06	117295	116548	619	607		-372.6
FC12-12	cu15	275.8	104.3	0.2	0.55	0.00	-249.6	1.7	0.4762	8.38E-04	3.97E-04	2.67E-06	120542	119574	1658	1695	*	-349.7
FC12-12	cu16	330.8	142.6	0.2	0.10	0.00	-231.6	1.3	0.4895	6.32E-04	5.44E-05	1.74E-06	120296	120168	1155	1181	*	-325.1
FC12-12	cn15	380.8	92.5	0.1	0.24	0.02	-217.0	1.6	0.5111	9.68E-04	1.95E-04	1.30E-05	125332	124887	1603	1615	*	-308.7

Stal	sample	Distance mm	U238 conc ppb	U238 conc error	232Th pmol/g	232Th error	d234U(T) ‰	d234U(T) error ‰	230Th/238U activity	230Th/238U activity error	232Th/238U activity	232Th/238U activity error	Uncorr	Monte Carlo Cor Age (years)	Error Minus	Error Plus		init d234U
FC12-15	co04		71.8	0.1	0.22	0.09	-80.8	1.7	0.6365	9.54E-04	2.37E-04	9.11E-05	132310	131886	1459	1466		-117.2
FC12-15	cp12		64.0	0.1	0.27	0.03	-50.0	1.3	0.6632	1.28E-03	3.20E-04	3.44E-05	132905	132358	1355	1388		-72.7
FC12-15	cp09	18	54.7	0.1	0.36	0.03	-118.3	1.6	0.6236	1.43E-03	5.01E-04	3.68E-05	140596	139633	1987	2018	*	-175.5
FC12-15	cx11	40	48.7	0.0	1.03	0.00	-123.8	0.6	0.6325	6.06E-04	1.61E-03	4.90E-06	147363	144200	1908	1847	*	-185.9
FC12-15	cx13	64	41.7	0.0	0.63	0.00	-86.7	0.7	0.6660	7.82E-04	1.14E-03	6.61E-06	147844	145759	1492	1505	*	-130.8
FC12-15	cx14	64	46.6	0.0	1.07	0.01	-76.2	0.8	0.6771	8.53E-04	1.73E-03	8.25E-06	148754	145617	2014	2022		-114.9
FC12-15	cx15	64	49.3	0.0	4.11	0.01	-95.0	0.6	0.7036	7.86E-04	6.33E-03	7.88E-06	172808	160358	7279	7090		-149.4
FC12-15	cx17	99.5	59.8	0.0	0.44	0.00	-127.9	0.6	0.6287	6.24E-04	5.61E-04	5.00E-06	147265	146163	1042	1060	*	-193.2
FC12-15	cx18	176.5	50.1	0.0	0.41	0.00	-129.4	0.5	0.6391	8.13E-04	6.23E-04	4.66E-06	153591	152358	1196	1231	*	-198.9
FC12-15	cx19	217	52.3	0.0	0.66	0.00	-166.2	0.5	0.6104	6.50E-04	9.60E-04	5.53E-06	156330	154272	1475	1509	*	-256.9
FC12-15	cp07	289.8	68.1	0.1	0.17	0.03	-175.8	1.1	0.6117	1.13E-03	1.88E-04	2.98E-05	162788	162375	2000	2078	*	-277.9
FC12-15	cp06		66.1	0.1	1.23	0.03	-184.3	1.1	0.6229	1.19E-03	1.41E-03	3.12E-05	176932	173687	3080	3214		-301.0
FC12-15	cn18		81.5	0.2	0.45	0.02	-131.9	2.3	0.6708	1.58E-03	4.17E-04	1.82E-05	174719	173877	3701	3964		-215.5
WR12-01	co11	6.4	491.1	0.2	0.98	0.08	-33.7	0.5	0.6320	2.74E-04	1.51E-04	1.23E-05	116822	116630	466	463	*	-46.8
WR12-01	cp08	26	230.6	0.1	1.32	0.03	-29.2	0.5	0.6492	5.80E-04	4.36E-04	8.76E-06	121519	120967	640	622	*	-41.1
WR12-01	cy01	38.3	523.5	0.2	4.12	0.00	-17.1	0.4	0.6634	3.25E-04	5.98E-04	2.83E-07	123176	122430	551	555	*	-24.2
WR12-01	cs18	42	483.1	0.2	7.87	0.01	-26.5	0.4	0.6685	4.47E-04	1.24E-03	1.70E-06	127649	126079	772	763	*	-37.9
WR12-01	cs19	47.3	379.0	0.2	1.63	0.01	-31.2	0.6	0.6678	5.56E-04	3.27E-04	2.25E-06	128744	128329	670	671	*	-44.8
WR12-01	cp04	54	336.6	0.1	0.15	0.03	-29.0	0.4	0.6694	4.80E-04	3.30E-05	5.96E-06	128705	128664	566	573	*	-41.7
WR12-01	cy03	54	372.1	0.2	0.45	0.00	-29.3	0.4	0.6696	4.07E-04	9.20E-05	3.98E-07	128859	128742	550	554		-42.1
WR12-01	cy05	54	421.0	0.3	0.29	0.00	-30.2	0.5	0.6656	3.70E-04	5.17E-05	3.15E-07	127657	127592	558	567		-43.3
WR12-01	ct13	68.5	343.0	0.1	0.48	0.02	-29.4	0.4	0.6712	4.39E-04	1.06E-04	3.41E-06	129505	129371	540	561	*	-42.4
WR12-01	cs17	90	363.7	0.2	0.15	0.01	-34.3	0.6	0.6781	5.43E-04	3.17E-05	2.21E-06	133655		688	704		-34.3
WR12-01	ct14	92	362.6	0.1	1.20	0.02	-27.9	0.4	0.6763	4.26E-04	2.51E-04	3.23E-06	130944	130626	566	574	*	-40.3
WR12-01	ct15	129	386.3	0.1	0.30	0.02	-20.7	0.3	0.6851	4.19E-04	5.96E-05	3.16E-06	132018	131943	538	545	*	-30.0
WR12-01	cp03	131	389.5	0.2	0.38	0.03	-20.4	0.3	0.6865	4.63E-04	7.40E-05	5.30E-06	132490	132398	576	562	*	-29.6
WR12-01	cs16	134	265.3	0.2	3.19	0.01	-13.2	0.8	0.7125	6.72E-04	9.12E-04	3.03E-06	140282	139148	944	971	*	-19.5
WR12-01	cy02	146	250.1	0.1	0.17	0.00	-13.3	0.4	0.7138	4.78E-04	5.10E-05	4.43E-07	140858	140795	627	634	*	-19.8
WR12-01	cy06	180	333.6	0.2	0.30	0.00	-5.2	0.4	0.7299	4.22E-04	6.82E-05	4.26E-07	144591	144507	631	633	*	-7.8
WR12-01	cp15	197	258.7	0.1	2.27	0.02	-10.3	0.4	0.7376	4.25E-04	6.67E-04	6.61E-06	149774	148949	701	706	*	-15.8
WR12-01	cy07	219	287.1	0.1	0.39	0.00	-3.8	0.4	0.7406	3.77E-04	1.02E-04	3.21E-07	148576	148452	628	625	*	-5.8
WR12-01	cn10	281.5	319.6	0.2	0.23	0.01	-6.9	0.6	0.7479	4.97E-04	5.39E-05	3.49E-06	152966	152900	828	826	*	-10.6
WR12-12	cs06	4.5	383.9	0.2	0.72	0.01	-40.0	0.6	0.6189	6.02E-04	1.43E-04	2.40E-06	114057	113873	589	588	*	-55.2
WR12-12	cu11	26.75	421.4	0.2	0.36	0.00	-30.3	0.5	0.6382	3.59E-04	6.40E-05	5.81E-07	118072	117991	517	506	*	-42.3
WR12-12	ct21	44.5	370.7	0.1	0.18	0.02	-30.0	0.4	0.6478	4.09E-04	3.60E-05	3.55E-06	121233	121188	499	493	*	-42.2
WR12-12	cu10	50	365.1	0.2	0.11	0.00	-30.7	0.6	0.6488	4.31E-04	2.34E-05	7.45E-07	121771	121741	588	574	*	-43.3
WR12-12	cu09	58.5	435.4	0.2	3.51	0.00	-32.6	0.5	0.6558	3.91E-04	6.11E-04	6.58E-07	124792	124012	609	616	*	-46.3
WR12-12	cy09	60.75	391.8	0.2	7.32	0.00	-34.3	0.4	0.6653	3.14E-04	1.42E-03	5.53E-07	128763	126939	807	791	*	-49.0
WR12-12	cu07	64.75	254.0	0.2	3.70	0.00	-14.9	0.8	0.6899	5.13E-04	1.11E-03	1.13E-06	132059	130678	850	874	*	-21.6
WR12-12	ct22	71.75	272.0	0.1	0.48	0.02	-7.3	0.4	0.6997	4.04E-04	1.34E-04	4.56E-06	133392	133227	566	561	*	-10.7
WR12-12	cu13	85.75	238.0	0.2	0.80	0.00	-4.6	0.8	0.7062	5.36E-04	2.55E-04	9.82E-07	134966	134654	757	799	*	-6.7
WR12-12	cy10	85.75	301.4	0.2	0.33	0.00	-3.6	0.4	0.7067	4.48E-04	8.37E-05	5.31E-07	134881	134779	578	592		-5.2
WR12-12	cy11	85.75	271.4	0.2	0.80	0.00	-7.0	0.4	0.7012	4.37E-04	2.25E-04	5.42E-07	133849	133574	600	585		-10.2
WR12-12	cs07	103.25	252.5	0.2	0.54	0.01	-2.6	0.7	0.7182	6.95E-04	1.62E-04	3.26E-06	138950	138753	838	856	*	-3.9
WR12-12	cy13	120.75	238.8	0.2	0.61	0.00	-1.7	0.5	0.7318	4.66E-04	1.93E-04	6.46E-07	144139	143905	687	666	*	-2.6

Notes:
^Sample ID identifies Multi-Collector ICP-MS batch (2 letters) and sample run order within batch (1-24)
^All activity ratios and ages are calculated using the U-series half-lives provided in Cheng et al., 2013
^2σ errors are Monte Carlo derived, with the following initial 230/232 ratios: SCH02 = 59 ± 13 ppm; BA02 = 56 ± 11 ppm; SC03 and SC02 = 111 ± 41 ppm; FC12 all = 78 ± 42 ppm; WR12 all = 60 ± 20 ppm

2. Isochrons

Three or more co-precipitated samples with variable ($^{238}U/^{232}Th$) were analyzed on multiple stalagmites from multiple cave chambers for a total of 25 isochron-derived initial ($^{230}Th/^{232}Th$) ratios. Figure S2. shows an example of isochron sampling locations on a slabbed stalagmite. The idea is that samples drilled further from the central growth axis will have greater detrital contamination than the "cleaner" central samples.

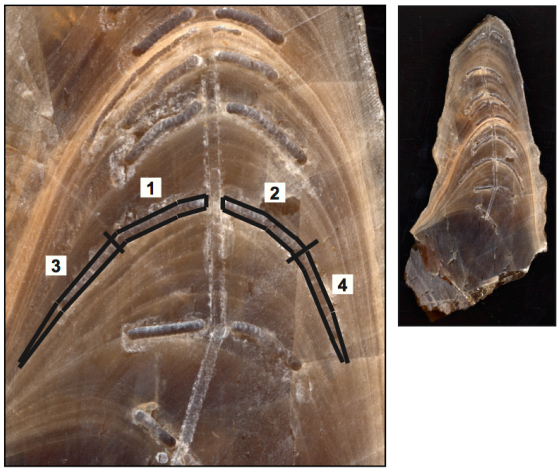

Figure C-S2. Mapped isochron drill spots along a single growth layer within a stalagmite collected from Whiterock (WR12-12).

Drilling multiple stalagmite samples that were all precipitated at the same geologic time but with variable ($^{238}U/^{232}Th$) is challenging in Mulu stalagmites that have already low [U] and require larger sample size. Because growth layers pinch together away from the central growth axis, it becomes more likely that drilling near the edges will clip other growth layers and add additional scatter to the isochron plots.

Figure C-S3. shows one of the XY pairs of the Osmond Type-II isochron diagram (($^{230}Th/^{238}U$) v. ($^{232}Th/^{238}U$)) for each of the 25 sampling spots along with the isochron's computed $(^{230}Th/^{232}Th)_{init}$ value and the square √(MSWD), computed using ISOPLOT 3.72 (Ludwig and Titterington, 1993).

Bukit Assam Cave (Buda)
BA02 & BA04

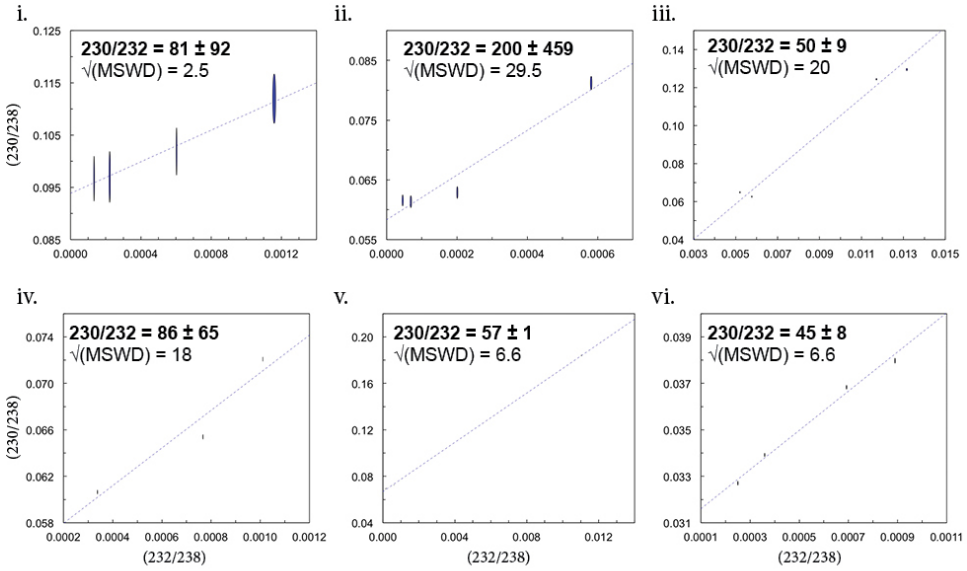

Snail Shell Cave (Buda)
SCH02 & SSC01

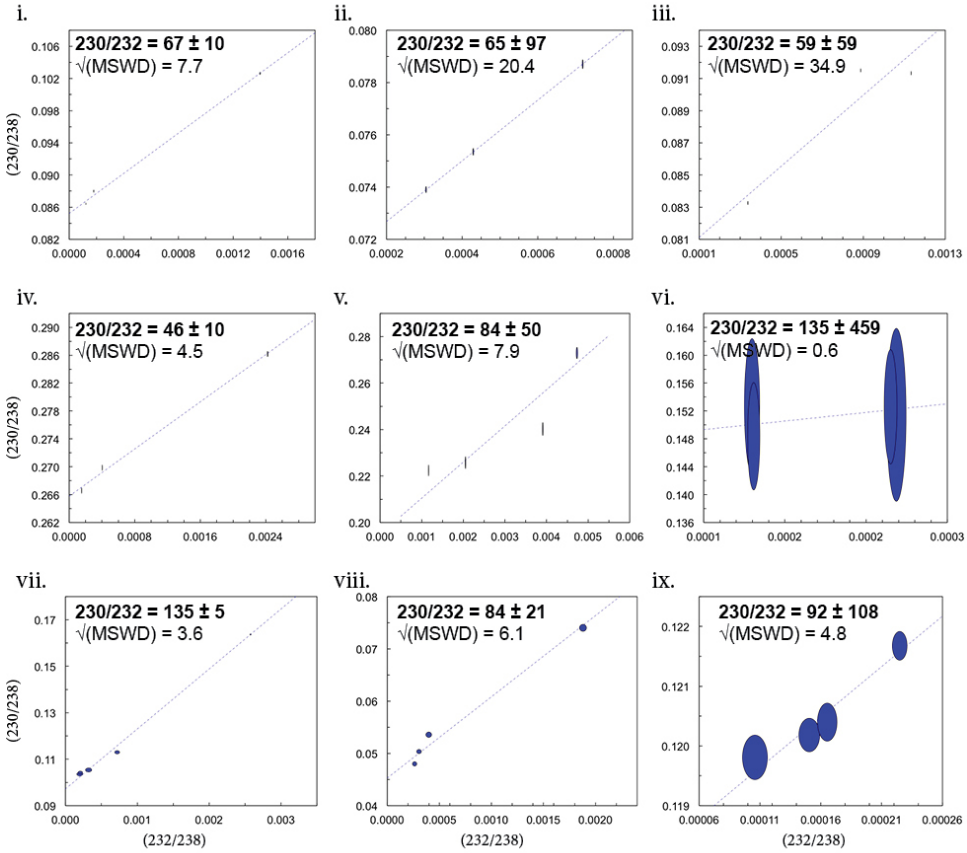

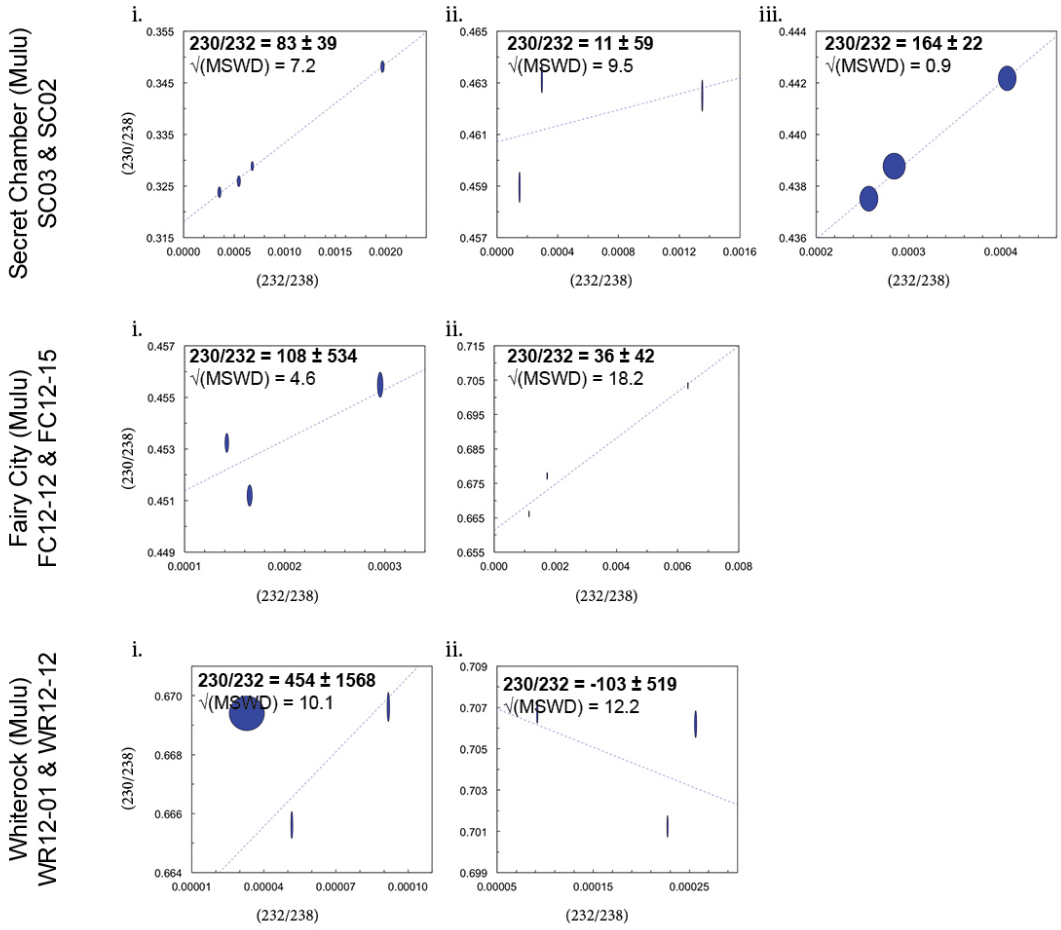

Figure C-S3. ($^{230Th}/^{238}U$) v. ($^{232}Th/^{238}U$) Osmond Type-II isochron diagrams for each sampling spot, with best line of fit and analytical elliptical error bars shown. Isochron's calculated $(^{230Th}/^{232}Th)_{init}$ value and the square √(MSWD), computed using ISOPLOT 3.72 (Ludwig and Titterington, 1993), is listed in each scatter plot. Isochron diagrams organized by cave chamber.

Error ellipses capture analytical uncertainties, but the degree of scatter about the best-fit line, coupled to the spread of the data points along the axes, determines the uncertainty in the initial $^{230Th}/^{232}Th$ ratio. The large scatter of $^{230}Th/^{232}Th$ values from the individual isochrons (Figure 3.3) is an indication that more than one source of initial ^{230}Th exists in our system and motivates us to take a conservative approach (i.e. larger error bars) to estimating a detrital $^{230}Th/^{232}Th$ ratio that is representative of our cave system. The weighted means and standard deviations for the detrital $^{230}Th/^{232}Th$

concentration are calculated for each stalagmite using the inverse of the 1σ errors from each isochron as the weighting factor. The weighted standard deviation is equal to the inverse of the sum of the weights for each cave system. Un-weighted means and standard deviations (for the population of isochron results from the same stalagmite) are also calculated for comparison. There is a large difference between the weighted standard deviation and the spread of the initial values from each line (the "un-weighted standard deviation"). For the final estimate of the detrital $^{230}Th/^{232}Th$ ratio we use the calculated weighted means and an uncertainty that lies between the simple population spread and the weighted uncertainty. We assign detrital atomic $^{230}Th/^{232}Th$ ratios as follows: BA02 = 55 ± 11 ppm; SCH02 = 59 ± 13 ppm; SC03 and SC02 = 111 ± 41 ppm; Fairy City = 78 ± 42 ppm (2σ errors; Fig. S12). These ratios are greater than the typical detrital bulk earth ratio (4 ± 2 ppm 2σ) frequently used in other stalagmite U-series dating applications. The greater detrital atomic $^{230}Th/^{232}Th$ ratio is likely due to a lack of other source rocks besides the Melinau Limestone in the Buda and Mulu cave.

3. Age Models and growth hiatuses

The age models for the stalagmites in this study were constructed using the StalAge algorithm (Scholz and Hoffman, 2011). One exception is FC12-14's upper younger section, which is separated from the rest of the record by a 40-ky hiatus, and only contains two U-series ages of 74.4 and 87.8 kybp, making it unfit for a StalAge Monte Carlo simulation. This portion of the record overlapped with two other previously published stalagmite records (SCO3 and SC02 (Carolin et al., 2013)), and a linear interpolation between chosen ages within the original ages' calculated 2σ age error (73.8 and 87.3 kybp) produced a well-fit overlapping record.

Original U-series ages with 2σ age error are plotted on top of the calculated Stalage model with 95% confidence intervals shown. For all records, if a repeat dating sample was drilled directly above or below a previously analyzed sample, the date with the smaller age error was used in constructing the age model.

Following Carolin et al. (2013), most potential hiatuses were identified in the stalagmite slab from optical evidence of a cessation of the carbonate accumulation (dark or white layer), and by U-series ages drilled immediately above and below such layers. Additional hiatuses were inferred wherever growth rates fell below 0.5 μm/yr in Whiterock and Fairy City stalagmites, as calculated from the StalAge model. Any $\delta^{18}O$ samples that fell on a potential hiatus were removed from the final oxygen isotope time series, as they are associated with large dating uncertainties. In the cases where hiatuses are inferred from dramatic changes in growth rate between two U-series dates, and where the hiatus is visible as a narrow band in the stalagmite images, growth rates from adjacent dates were linearly interpolated to the hiatus layer from both sides.

The age-depth plots for SC03, WR12-01, WR12-12, FC12-12, FC12-14, and FC12-15 are provided in Figure C-S4 through C-S9.

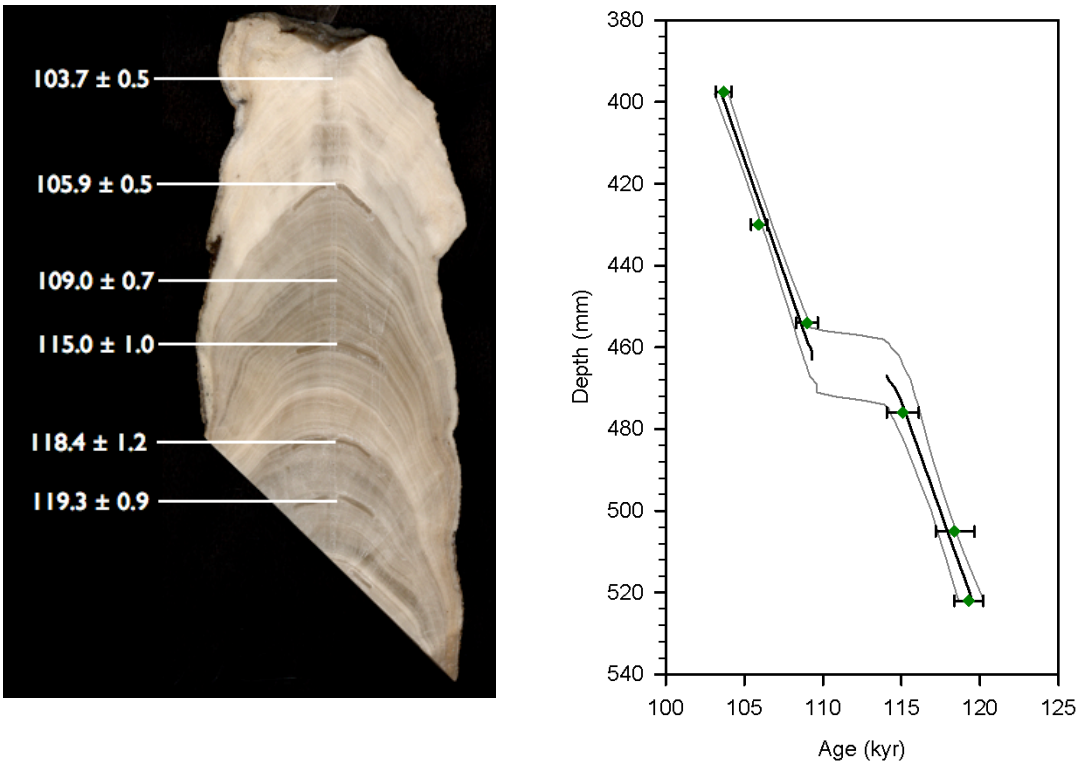

Figure C-S4. (A) High-resolution scan image of lower SC03, showing original U-series dates reported in kyr. (B) Age-depth plot. Data points not included in age model are in red in panel A and not shown in panel B (see Table C-S1). Error bars represent 2σ dating uncertainties. Black line indicates the StalAge age-depth model. Grey outer curves indicate 95% confidence interval endpoints for an ensemble of age models produced using StalAge (Scholz and Hoffman, 2011).

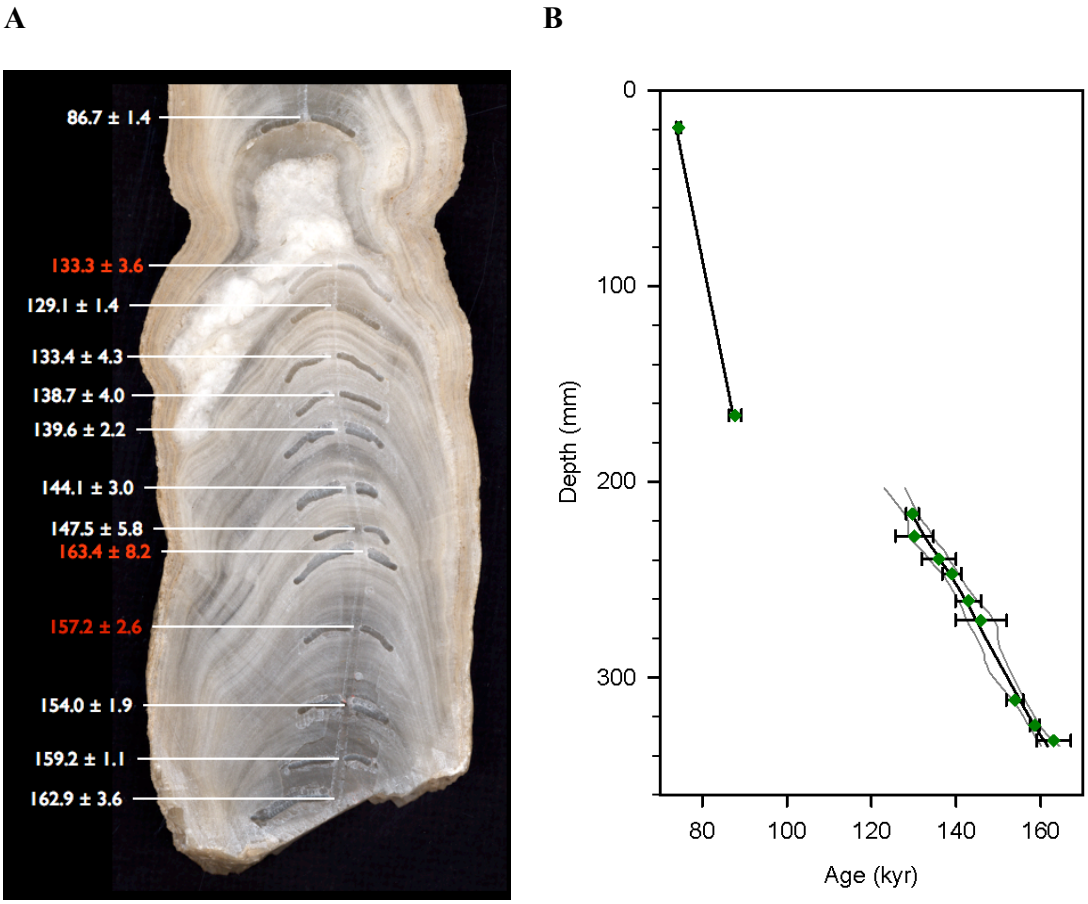

Figure C-S5. (A) High-resolution scan image of FC12-14, showing original U-series dates reported in kyr. (B) Age-depth plot. Data points not included in age model are in red in panel A and not shown in panel B (see Table C-S1). Error bars represent 2σ dating uncertainties. Black line indicates the StalAge age-depth model. Grey outer curves indicate 95% confidence interval endpoints for an ensemble of age models produced using StalAge (Scholz and Hoffman, 2011).

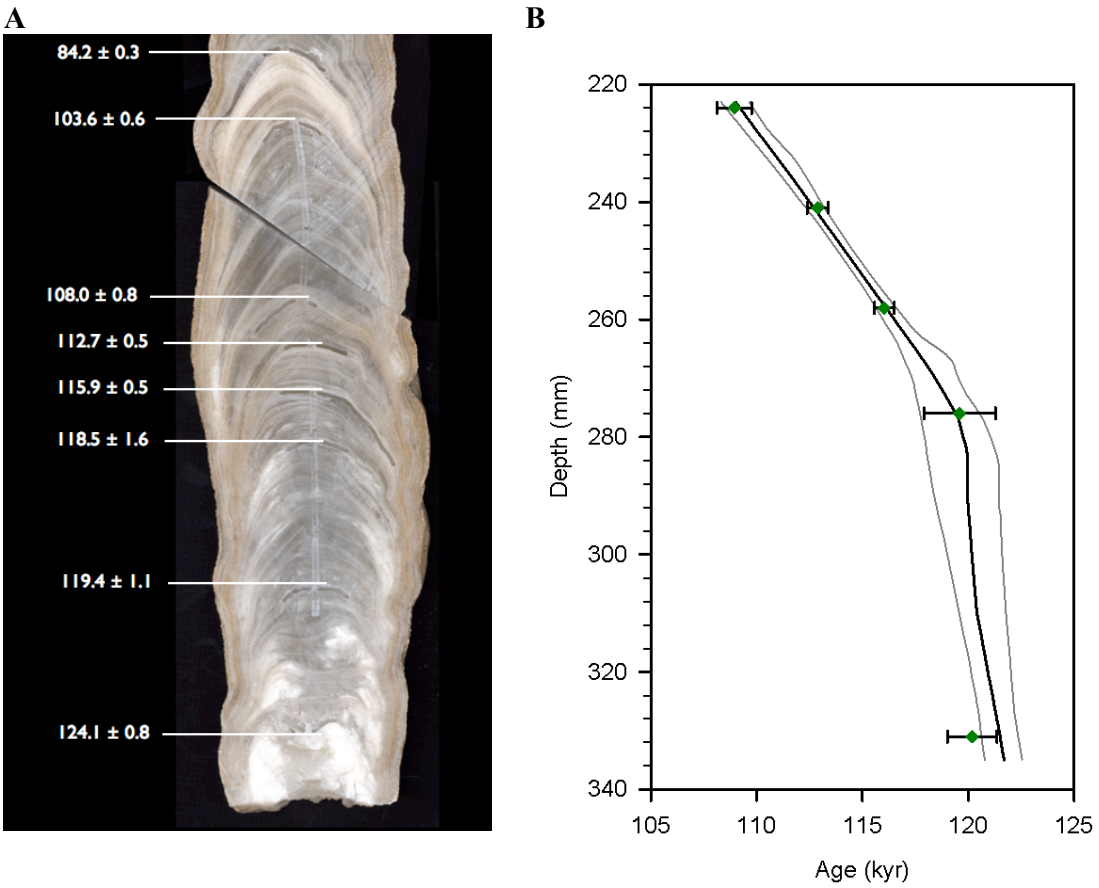

Figure C-S6. (A) High-resolution scan image of FC12-12, showing original U-series dates reported in kyr. (B) Age-depth plot. Data points not included in age model are in red in panel A and not shown in panel B (see Table C-S1). Error bars represent 2σ dating uncertainties. Black line indicates the StalAge age-depth model. Grey outer curves indicate 95% confidence interval endpoints for an ensemble of age models produced using StalAge (Scholz and Hoffman, 2011).

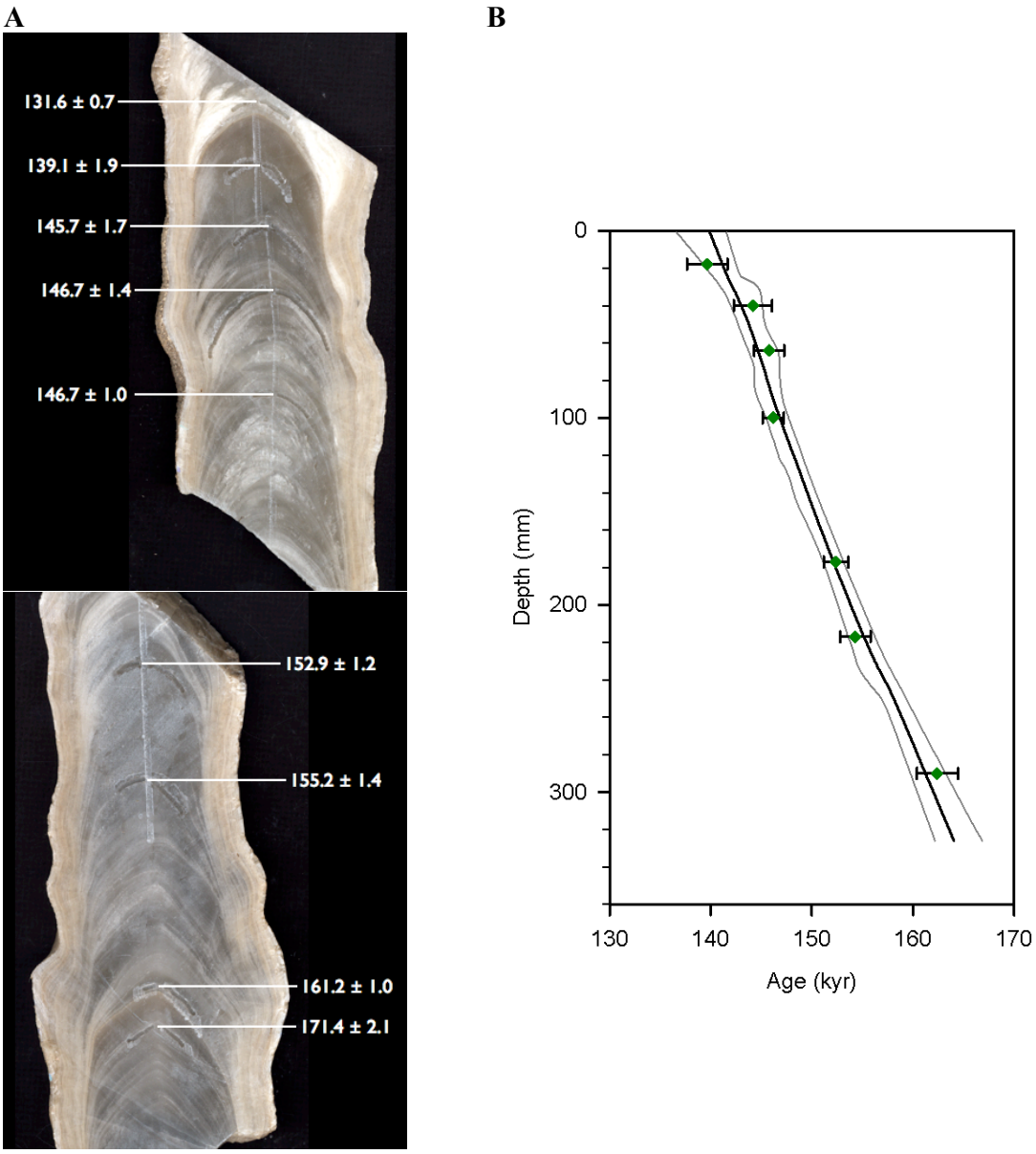

Figure C-S7. (A) High-resolution scan image of FC12-15, showing original U-series dates reported in kyr. (B) Age-depth plot. Data points not included in age model are in red in panel A and not shown in panel B (see Table C-S1). Error bars represent 2σ dating uncertainties. Black line indicates the StalAge age-depth model. Grey outer curves indicate 95% confidence interval endpoints for an ensemble of age models produced using StalAge (Scholz and Hoffman, 2011).

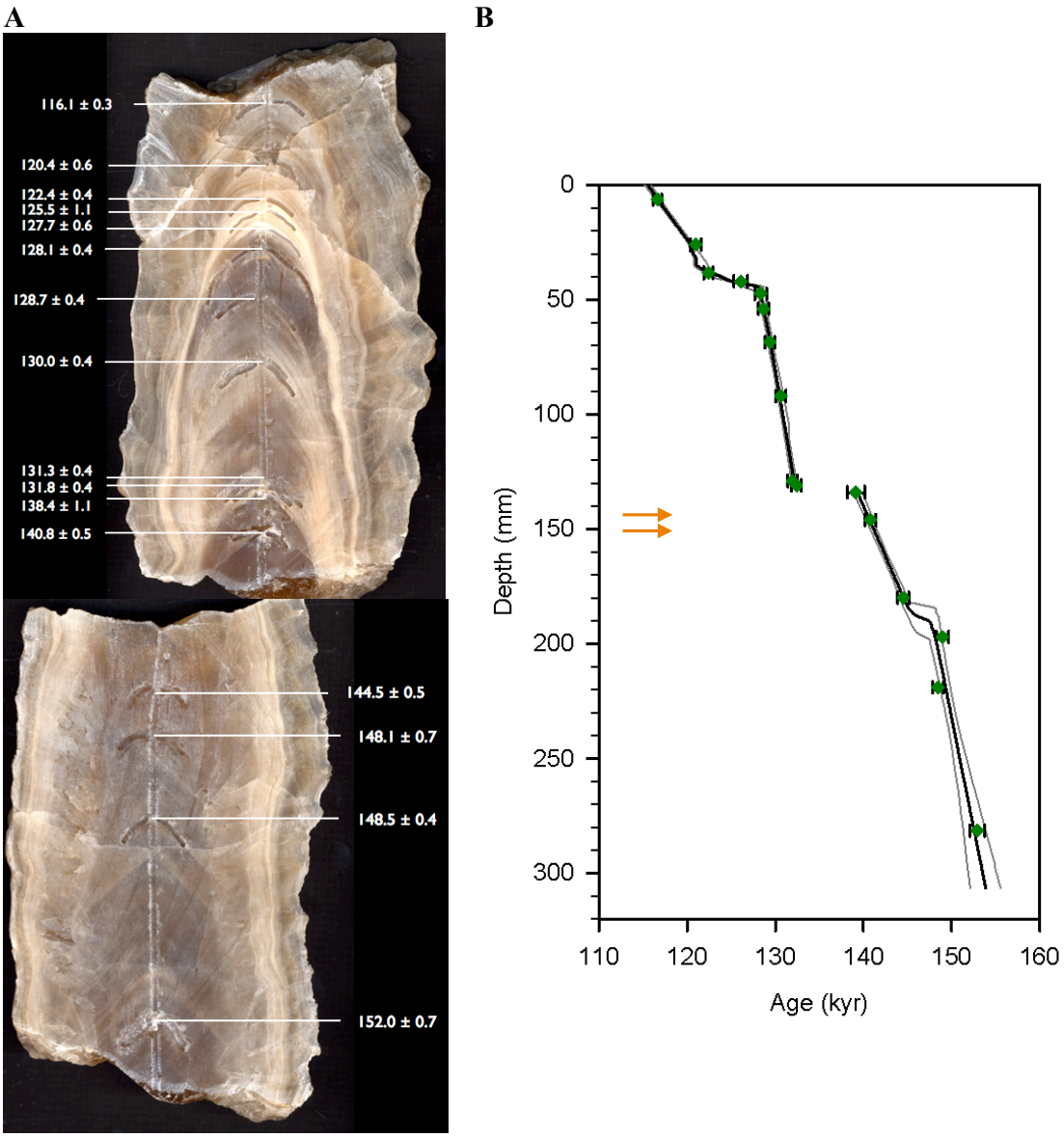

Figure C-S8. (A) High-resolution scan image of WR12-01, showing original U-series dates reported in kyr. (B) Age-depth plot. Data points not included in age model are in red in panel A and not shown in panel B (see Table C-S1). Error bars represent 2σ dating uncertainties. Black line indicates the StalAge age-depth model. Grey outer curves indicate 95% confidence interval endpoints for an ensemble of age models produced using StalAge (Scholz and Hoffman, 2011).

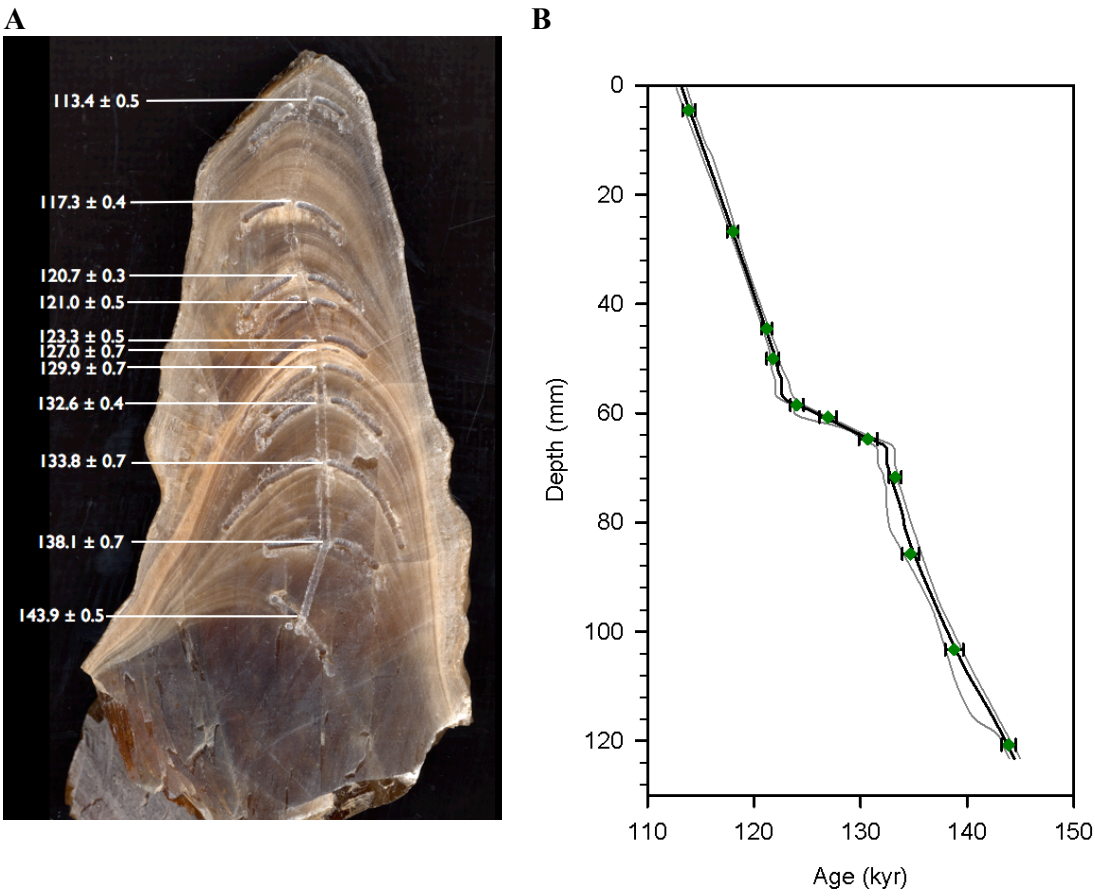

Figure C-S9. (A) High-resolution scan image of lower SC03, showing original U-series dates reported in kyr. (B) Age-depth plot. Data points not included in age model are in red in panel A and not shown in panel B (see Table C-S1). Error bars represent 2σ dating uncertainties. Black line indicates the StalAge age-depth model. Grey outer curves indicate 95% confidence interval endpoints for an ensemble of age models produced using StalAge (Scholz and Hoffman, 2011).

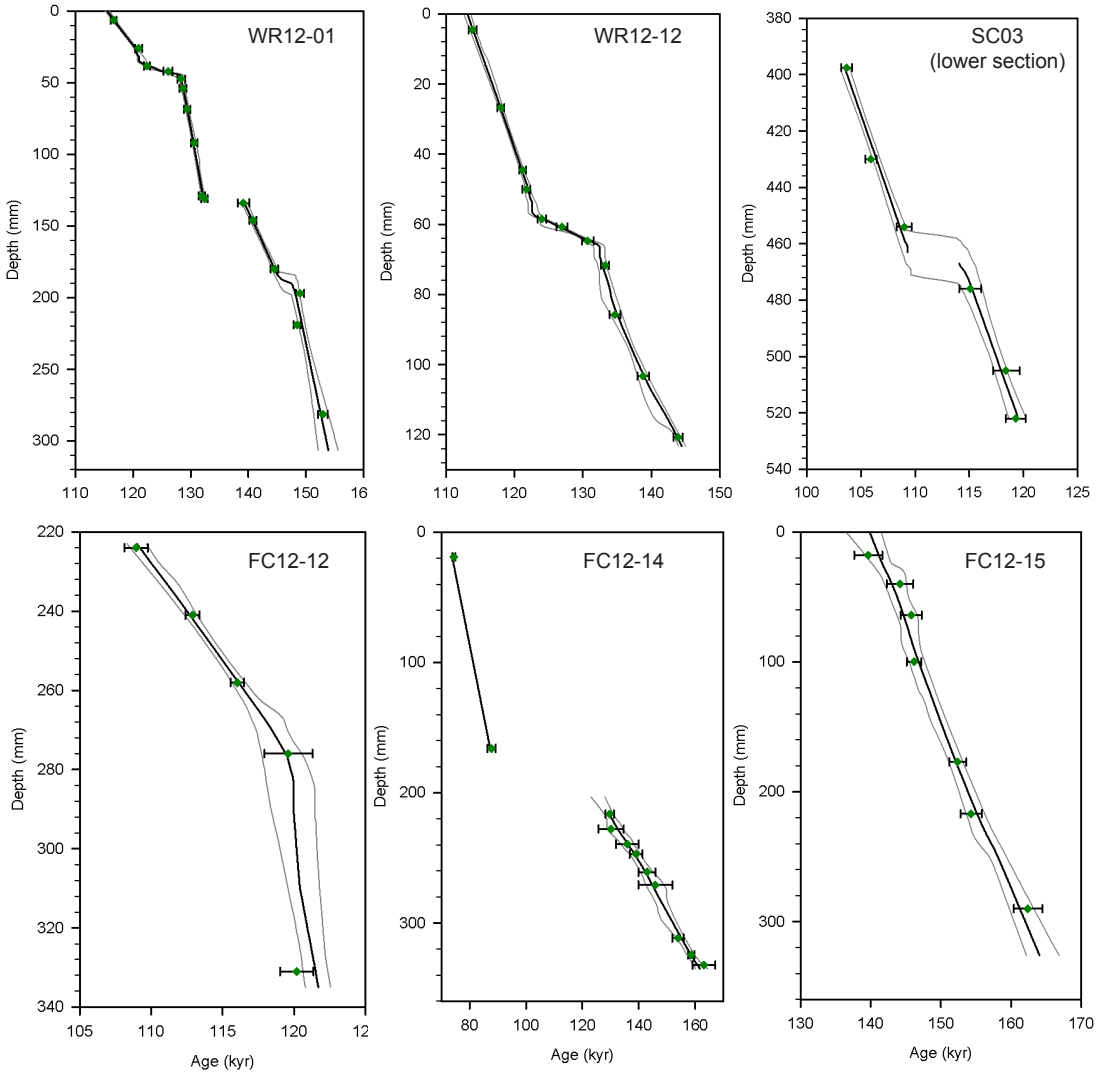

Figure C-S10. Summary of age-depth plots, provided in Figures C-S4 through C-S9.

4. Evidence of Mulu $\delta^{18}O$ equilibrium calcite precipitation

Dorale and Liu (2009) argue that the only method that can be used to ensure that isotopic equilibrium is maintained during calcite formation is to replicate oxygen isotopic values in two or more stalagmites. If the isotopic profiles are the same then it can be concluded that the calcite was formed under equilibrium conditions. A modern-day study at Gunung Buda and Gunung Mulu measures present-day rainwater $\delta^{18}O$ equal to -6.8 ± 1.1‰SMOW and fast and slow dripwaters to be -6.6 ± 1.0‰SMOW and -7.0 ± 1.1‰SMOW, respectively, which agree within error. Modern calcite from one of the stalagmites used for this project is approximately -9.1‰PDB, which is in good agreement with the calculated $\delta^{18}O_{calcite}$ (-8.6‰PDB) at equilibrium with T = 26°C (299K) as measured in Cobb et al. (2007). Further evidence of calcite precipitation under equilibrium conditions at Mulu is provided in Partin et al. (2007). Here it was demonstrated that all three Borneo stalagmites analyzed passed the "Hendy test", meaning that $\delta^{18}O$ did not vary significantly across a single growth layer. Further, the millennial scale $\delta^{18}O$ variability between the nine stalagmites in the 160ky composite record (extracted from caves spanning over 20 km) s also well aligned (Carolin et al., 2013; this study), indicating that the variability is due to regional climate changes associated with rainfall $\delta^{18}O$ variability and not a result of calcite precipitation at disequilibrium states.

5. Spectral Analysis

Spectral analysis (Thomson, 1982; Percival and Walden, 1993) was performed on 100-yr average composite Mulu stalagmite record from 0-160kybp using a single discrete prolate spheroidal sequences (DPSS) taper method (Matlab script provided by Prof. Peter

Huybers, phuyber@mit.edu). The 95% confidence interval was computed by multiplying the power spectrum of a sequence of red noise samples of length N by the chi-squared value at the 95% confidence level with 2 degrees of freedom. The results of the spectral analysis are shown in Figure 5.4. A similar analysis performed on 15 overlapping Chinese stalagmite records averaged in 801 200-year boxcar bins (N = 801) is shown in Figure 4 in comparison.

The spectral analysis confirms a strong precessional signal in the Mulu record, with a muted peak at the obliquity period, 41ky, though it is not greater than red noise power density equivalent. Multi-taper method coherence using adaptive weighting and corrections for inherent bias to coherence estimates was performed between the Mulu 160ky record and the equatorial insolation time series (Berger, 1978) daily across all four seasons (Matlab script provided by Prof. Peter Huybers, phuyber@mit.edu; number of windows = 1.5). The calculated coherence-squared estimates at 23ky period did not significantly vary between the 12 months, as expected, though the coherence-squared value did move closer to 1.0 when using the ice-volume $\delta^{18}O$-corrected record. The best

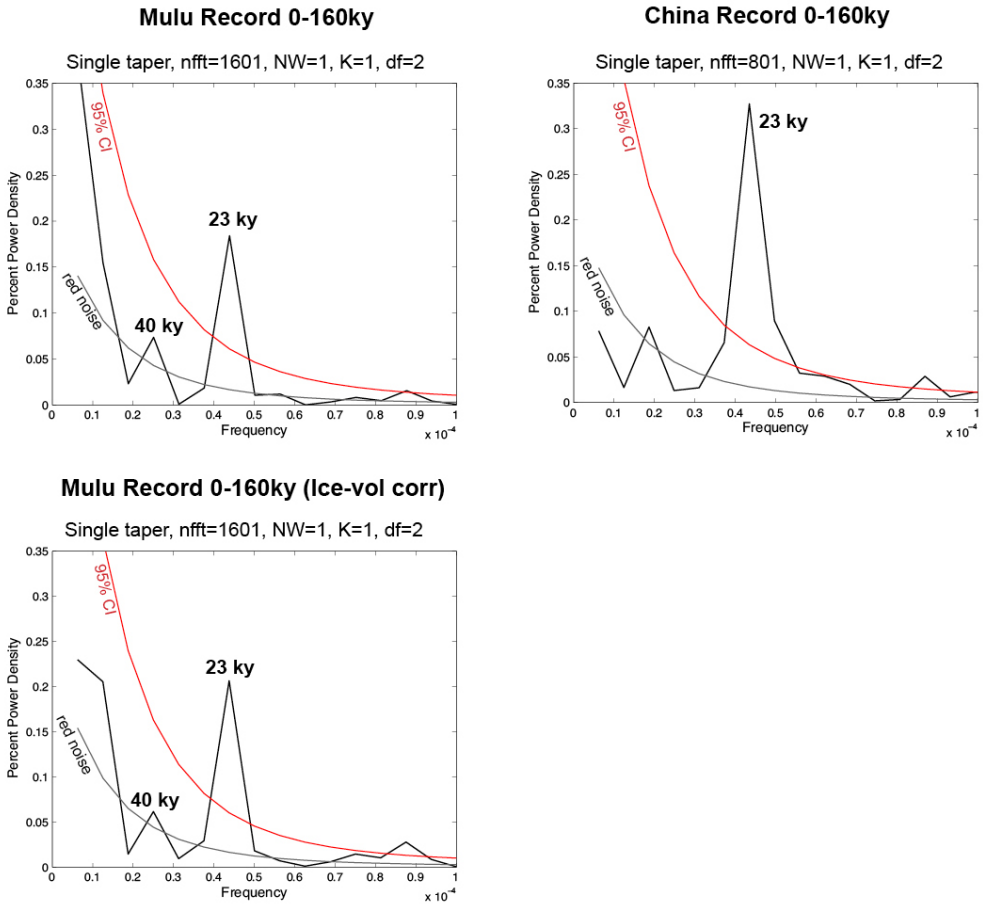

Figure C-S11. Percent power density from single-taper method spectral analysis on Mulu $\delta^{18}O$ composite stalagmite 160 ky record (100yr sampling resolution) (upper left), ice-volume corrected Mulu $\delta^{18}O$ composite stalagmite 160 ky record (100yr sampling resolution) (lower), and Chinese $\delta^{18}O$ composite stalagmite 160 ky record (200yr sampling resolution). Citations provided in Figure 5.6.

precessional fit (based on smallest phase lag) for the uncorrected record is 1 month following fall equinox (mid-October) while the best precessional fit for the ice volume corrected record is later in early November.

REFERENCES

Adkins, J.F., J.W. Partin, D.P. Fernandez, K.M. Cobb, L.F. Robinson, U-Series Dating of Stalagmites from Northern Borneo, in prep.

Altabet, M. A., M. J. Higginson, and D. W. Murray (2002), The effect of millennial-scale changes in Arabian Sea denitrification on atmospheric CO2, *Nature*, *415*(5858), 159-152.

Andersen, K. K., et al. (2004), High-resolution record of Northern Hemisphere climate extending into the last interglacial period, *Nature*, *431*(7005), 147-151.

Ayliffe, L. K., et al. (2013), Rapid interhemispheric climate links via the Australasian monsoon during the last deglaciation, *Nat. Commun.*, *4*.

Barbante, C., et al. (2005), One-to-one coupling of glacial climate variability in Greenland and Antarctica, *Nature*, *444*(7115), 195-198.

Bard, E., B. Hamelin, and R. G. Fairbanks (1990), U-Th ages obtained by mass-spectrometry in corals from Barbados - sea-level during the past 130,000 years, *Nature*, *345*(5283), 455-458.

Bard, E., B. Hamelin, and D. Delanghe-Sabatier (2010), Deglacial Meltwater Pulse 1B and Younger Dryas Sea Levels Revisited with Boreholes at Tahiti, *Science*, *327*(5970), 1235-1237.

Bereiter, B., D. Luthi, M. Siegrist, S. Schupbach, T. F. Stocker, and H. Fischer (2012), Mode change of millennial CO2 variability during the last glacial cycle associated with a bipolar marine carbon seesaw, *Proceedings of the National Academy of Sciences of the United States of America*, *109*(25), 9755-9750.

Berger, A. L. (1978), Long-term variations of daily insolation and quaternary climatic changes, *Journal of the Atmospheric Sciences*, *35*(12), 2352-2357.

Berger, A., Loutre, M.F., 1991. INSOLATION VALUES FOR THE CLIMATE OF THE LAST 10000000 YEARS. Quaternary Science Reviews 10, 297-317.

Bush, A. B. G., and R. G. Fairbanks (2003), Exposing the Sunda shelf: Tropical responses to eustatic sea level change, *Journal of Geophysical Research-Atmospheres*, *108*(D15).

Cane, M., and A. C. Clement (1999), A role for the tropical Pacific coupled ocean-atmosphere system on Milankovich and millennial timescales. *Geophys. Monogr. Ser. 112*, 373.

Carolin, S. A., K. M. Cobb, J. F. Adkins, B. Clark, J. L. Conroy, S. Lejau, J. Malang, and A. A. Tuen (2013), Varied Response of Western Pacific Hydrology to Climate Forcings over the Last Glacial Period, *Science*, *340*(5140), 1554-1555.

Carolin, S. A., J. F. Adkins, K. M. Cobb, J. Lynch-Steiglitz, J.W. Moerman, S. Lejau, J. Malang, and A. A. Tuen, 150ky multi-stalagmite $\delta^{18}O$ record from northern Borneo, in prep.

Cheng, H., R. L. Edwards, W. S. Broecker, G. H. Denton, X. G. Kong, Y. J. Wang, R. Zhang, and X. F. Wang (2009), Ice Age Terminations, *Science*, *325*(5950), 248-252.

Cheng, H., et al. (2013a), Improvements in Th-230 dating, Th-230 and U-234 half-life values, and U-Th isotopic measurements by multi-collector inductively coupled plasma mass spectrometry, *Earth Planet. Sci. Lett.*, *371*, 82-91.

Cheng, H., A. Sinha, F. W. Cruz, X. F. Wang, R. L. A. Edwards, F. M. d'Horta, C. C. Ribas, M. Vuille, L. D. Stott, and A. S. Auler (2013b), Climate change patterns in Amazonia and biodiversity, *Nat. Commun.*, *4*.

Chesner, C. A., W. I. Rose, A. Deino, R. Drake, and J. A. Westgate (1991), Eruptive history of earths largest quaternary caldera (Toba, Indonesia) clarified, *Geology*, *19*(3), 200-203.

Chesner, C. A. (2012), The Toba Caldera Complex, *Quaternary International*, *258*, 5-18.

Chiang, J. C. H., and C. M. Bitz (2005), Influence of high latitude ice cover on the marine Intertropical Convergence Zone, *Climate Dynamics*, *25*(5), 477-495.

Clement, A. C., R. Seager, and M. A. Cane (1999), Orbital controls on the El Niño/Southern Oscillation and the tropical climate, *Paleoceanography*, *14*(4), 441-455.

Clement, A. C., A. Hall, and A. J. Broccoli (2004), The importance of precessional signals in the tropical climate, *Climate Dynamics*, *22*(4), 327-341.

Cobb, K. M., J. F. Adkins, J. W. Partin, and B. Clark (2007), Regional-scale climate influences on temporal variations of rainwater and cave dripwater oxygen isotopes in northern Borneo, *Earth Planet. Sci. Lett.*, *253*(3-4), 207-220.

Cutler, K. B., R. L. Edwards, F. W. Taylor, H. Cheng, J. Adkins, C. D. Gallup, P. M. Cutler, G. S. Burr, and A. L. Bloom (2003), Rapid sea-level fall and deep-ocean temperature change since the last interglacial period, *Earth Planet. Sci. Lett.*, *205*(3-4), 253-271.

Dannenmann, S., B. K. Linsley, D. W. Oppo, Y. Rosenthal, and L. Beaufort (2003), East Asian monsoon forcing of suborbital variability in the Sulu Sea during Marine Isotope Stage 3: Link to Northern Hemisphere climate, *Geochemistry Geophysics Geosystems*, *4*.

Dansgaard, W. (1964), Stable isotopes in precipitation, *Tellus*, *15*(4), 435-458.

Dansgaard, W., et al. (1993), Evidence for general instability of past climate from a 250-kyr ice-core record, *Nature*, *354*(5434), 218-220.

De Deckker, P., Tapper, N.J., van der Kaars, S., 2003. The status of the Indo-Pacific Warm Pool and adjacent land at the Last Glacial Maximum. Global and Planetary Change 35, 25-35.

Denniston, R. F., K. H. Wyrwoll, Y. Asmerom, V. J. Polyak, W. F. Humphreys, J. Cugley, D. Woods, Z. LaPointe, J. Peota, and E. Greaves (2013a), North Atlantic forcing of millennial-scale Indo-Australian monsoon dynamics during the Last Glacial period, *Quaternary Science Reviews*, *72*, 159-158.

Denniston, R. F., Y. Asmerom, M. Lachniet, V. J. Polyak, P. Hope, N. An, K. Rodzinyak, and W. F. Humphreys (2013b), A Last Glacial Maximum through middle Holocene stalagmite record of coastal Western Australia climate, *Quaternary Science Reviews*, *77*, 101-112.

Denniston, R. F., et al. (2013c), A Stalagmite record of Holocene Indonesian-Australian summer monsoon variability from the Australian tropics, *Quaternary Science Reviews*, *78*, 155-158.

Denton, G. H., R. F. Anderson, J. R. Toggweiler, R. L. Edwards, J. M. Schaefer, and A. E. Putnam (2010), The Last Glacial Termination, *Science*, *328*(5985), 1552-1555.

DiNezio, P. N., A. Clement, G. A. Vecchi, B. Soden, A. J. Broccoli, B. L. Otto-Bliesner, and P. Braconnot (2011), The response of the Walker circulation to Last Glacial Maximum forcing: Implications for detection in proxies, *Paleoceanography*, *25*.

DiNezio, P. N., and J. E. Tierney (2013), The effect of sea level on glacial Indo-Pacific climate, *Nature Geoscience*, *5*(5), 485-491.

Dorale, J. A., and Z. H. Liu (2009), Limitations of hendy test criteria in judging the paleoclimatic suitability of speleothems and the need for replication, *Journal of Cave and Karst Studies*, *71*(1), 73-80.

Dykoski, C. A., R. L. Edwards, H. Cheng, D. X. Yuan, Y. J. Cai, M. L. Zhang, Y. S. Lin, J. M. Qing, Z. S. An, and J. Revenaugh (2005), A high-resolution, absolute-dated Holocene and deglacial Asian monsoon record from Dongge Cave, China, *Earth Planet. Sci. Lett.*, *233*(1-2), 71-85.

Edwards, R. L., J. W. Beck, G. S. Burr, D. J. Donahue, J. M. A. Chappell, A. L. Bloom, E. R. M. Druffel, and F. W. Taylor (1993), A large drop in atmospheric C-14/C-12 and reduced melting in the Younger Dryas, documented with Th-230 ages of corals, *Science*,

250(5110), 952-958.

Epstein, S., R. Buchsbaum, H. A. Lowenstam, and H. C. Urey (1953), Revised carbonate-water isotopic temperature scale, *Geological Society of America Bulletin*, *54*(11), 1315-1325.

Esat, T. M., M. T. McCulloch, J. Chappell, B. Pillans, and A. Omura (1999), Rapid fluctuations in sea level recorded at Huon Peninsula during the penultimate deglaciation, *Science*, *283*(5399), 197-201.

Fleming, K., P. Johnston, D. Zwartz, Y. Yokoyama, K. Lambeck, and J. Chappell (1998), Refining the eustatic sea-level curve since the Last Glacial Maximum using far- and intermediate-field sites, *Earth Planet. Sci. Lett.*, *153*(1-4), 327-342.

Gallup, C. D., H. Cheng, F. W. Taylor, and R. L. Edwards (2002), Direct determination of the timing of sea level change during termination II, *Science*, *295*(5553), 310-313.

Gascoyne, M., Geochemistry of the actinides and their daughters, in: M. Ivanovich, R.S. Harmon (Eds.), Uranium Series Disequilibrium : Applications to Environmental Problems, Clarendon Press, Oxford, 1982, pp. 33-55.

Gibbons, F. T., D. W. Oppo, M. Mohtadi, Y. Rosenthal, J. Cheng, Z. Y. Liu, and B. K. Linsley (2014), Deglacial delta O-18 and hydrologic variability in the tropical Pacific and Indian Oceans, *Earth Planet. Sci. Lett.*, *387*, 240-251.

Griffiths, M. L., et al. (2009), Increasing Australian-Indonesian monsoon rainfall linked to early Holocene sea-level rise, *Nature Geoscience*, *2*(9), 535-539.

Griffiths, M. L., et al. (2010), Evidence for Holocene changes in Australian-Indonesian monsoon rainfall from stalagmite trace element and stable isotope ratios, *Earth Planet. Sci. Lett.*, *292*(1-2), 27-38.

Grottoli, A. G., J. F. Adkins, W. R. Panero, D. M. Reaman, and K. Moots (2010), Growth rates, stable oxygen isotopes (delta O-18), and strontium (Sr/Ca) composition in two species of Pacific sclerosponges (Acanthocheatetes wellsi and Astrosclera willeyana) with delta O-18 calibration and application to paleoceanography, *Journal of Geophysical Research-Oceans*, *115*.

Hanebuth, T. J. J., H. K. Voris, Y. Yokoyama, Y. Saito, and J. i. Okuno (2011), Formation and fate of sedimentary depocentres on Southeast Asia's Sunda Shelf over the past sea-level cycle and biogeographic implications, *Earth-Science Reviews*, *104*(1-3), 92-110.

Heinrich, H. (1988), Origin and consequences of cyclic ice rafting in the northeast Atlantic-ocean during the past 130,000 years, *Quaternary Research*, *29*(2), 142-152.

Hemming, S. R. (2004), Heinrich events: Massive late pleistocene detritus layers of the North Atlantic and their global climate imprint, *Reviews of Geophysics*, *42*(1).

Henderson, G. M., and N. C. Slowey (2000), Evidence from U-Th dating against Northern Hemisphere forcing of the penultimate deglaciation, *Nature*, *404*(5773), 51-55.

Hendy, C. H. (1971), Isotopic geochemistry of speleothems. 1. Calculation of effects of different modes of formation on isotopic composition of speleothems and their applicability as palaeoclimatic indicators, *Geochimica Et Cosmochimica Acta*, *35*(8), 801-&.

Hendy, I. L., and J. P. Kennett (2000), Dansgaard-Oeschger cycles and the California Current System: Planktonic foraminiferal response to rapid climate change in Santa Barbara Basin, Ocean Drilling Program hole 893A, *Paleoceanography*, *15*(1), 30-42.

Huang, Y. M., and I. J. Fairchild (2001), Partitioning of Sr2+ and Mg2+ into calcite under karst-analogue experimental conditions, *Geochimica Et Cosmochimica Acta*, *55*(1), 47-52.

Indermuhle, A., et al. (1999), Holocene carbon-cycle dynamics based on CO2 trapped in ice at Taylor Dome, Antarctica, *Nature*, *398*(5723), 121-125.

Ivanovich, M. and R.S. Harmon (Eds.). (1992) *Uranium-series Disequilibrium: Applications to Earth, Marine, and Environmental Sciences*, 2nd Ed. New York, NY: Oxford University Press.

Kanner, L. C., S. J. Burns, H. Cheng, and R. L. Edwards (2012), High-Latitude Forcing of the South American Summer Monsoon During the Last Glacial, *Science*, *335*(5058), 570-573.

Kawamura, K., et al. (2007), Northern Hemisphere forcing of climatic cycles in Antarctica over the past 350,000 years, *Nature*, *448*(7155), 912-U914.

Kelly, M. J., R. L. Edwards, H. Cheng, D. X. Yuan, Y. J. Cai, M. L. Zhang, Y. S. Lin, and Z. S. An (2005), High resolution characterization of the Asian Monsoon between 145,000 and 99,000 years BP from Dongge Cave, China and global correlation of events surrounding Termination II, *Palaeogeography Palaeoclimatology Palaeoecology*, *235*(1-2), 20-38.

Kim, S. T., and J. R. Oneil (1997), Equilibrium and nonequilibrium oxygen isotope effects in synthetic carbonates, *Geochimica Et Cosmochimica Acta*, *51*(15), 3451-3475.

Klein, S. A., and D. L. Hartmann (1993), The seasonal cycle of low stratiform clouds, *J. Clim.*, *5*(8), 1587-1505.

Koutavas, A., J. Lynch-Stieglitz, T. M. Marchitto, and J. P. Sachs (2002), El Niño-like

pattern in ice age tropical Pacific sea surface temperature, *Science*, *297*(5579), 225-230.

Lea, D. W., D. K. Pak, and H. J. Spero (2000), Climate impact of late quaternary equatorial Pacific sea surface temperature variations, *Science*, *289*(5485), 1719-1724.

Lea, D. W. (2004), The 100 000-yr cycle in tropical SST, greenhouse forcing, and climate sensitivity, *J. Clim.*, *17*(11), 2170-2179.

Lea, D. W., D. K. Pak, C. L. Belanger, H. J. Spero, M. A. Hall, and N. J. Shackleton (2005), Paleoclimate history of Galapagos surface waters over the last 135,000 yr, *Quaternary Science Reviews*, *25*(11-12), 1152-1157.

Levi, C., L. Labeyrie, F. Bassinot, F. Guichard, E. Cortijo, C. Waelbroeck, N. Caillon, J. Duprat, T. de Garidel-Thoron, and H. Elderfield (2007), Low-latitude hydrological cycle and rapid climate changes during the last deglaciation, *Geochemistry Geophysics Geosystems*, *8*.

Ludwig, K. R., and D. M. Titterington (1994), Calculation of (230)Th/U isochrons, ages, and errors, *Geochimica Et Cosmochimica Acta*, *58*(22), 5031-5042.

Madden, R.A. and Julian P.R. (1972) Description of global-scale circulation cells in tropics with a 40–50day period. *J. Atmos. Sci.* **29**, 1109–1123.

Martinson, D. G., N. G. Pisias, J. D. Hays, J. Imbrie, T. C. Moore, and N. J. Shackleton (1987), Age dating and the orbital theory of the ice ages - development of a high-resolution 0 to 300,000 year chronostratigraphy, *Quaternary Research*, *27*(1), 1-29.

McManus, J. F., R. Francois, J. M. Gherardi, L. D. Keigwin, and S. Brown-Leger (2004), Collapse and rapid resumption of Atlantic meridional circulation linked to deglacial climate changes, *Nature*, *428*(5985), 834-837.

Meckler, A. N., M. O. Clarkson, K. M. Cobb, H. Sodemann, and J. F. Adkins (2012), Interglacial Hydroclimate in the Tropical West Pacific Through the Late Pleistocene, *Science*, *335*(5085), 1301-1304.

Milankovitch. M. (1941). Kanon der Erdbestrahlung une sei Eiszeitenproblem. Acad. R. Serbe (Belegrade), ed. Spec. 133 Sect. Sci. Math. Naturaies. 533. (translated by the Israel Program for Scientific Translations. Jerusalem, 1970).

Moerman, J. W., K. M. Cobb, J. F. Adkins, H. Sodemann, B. Clark, and A. A. Tuen (2013), Diurnal to interannual rainfall delta O-18 variations in northern Borneo driven by regional hydrology, *Earth Planet. Sci. Lett.*, *359*, 108-119.

Moerman, J. W., K. M. Cobb, J.W. Partin, S. Lejau, J. Malang, B. Clark, and A. A. Tuen, Borneo cave dripwater isotope timeseries resolve the 2009-2012 ENSO cycle, in prep.

Monnin, E., A. Indermuhle, A. Dallenbach, J. Fluckiger, B. Stauffer, T. F. Stocker, D. Raynaud, and J. M. Barnola (2001), Atmospheric CO2 concentrations over the last glacial termination, *Science*, *291*(5501), 112-114.

NGRIP members (2004), High-resolution record of Northern Hemisphere climate extending into the last interglacial period. Nature 431, 147-151.

Oppenheimer, C. (2003), Climatic, environmental and human consequences of the largest known historic eruption: Tambora volcano (Indonesia) 1815, *Progress in Physical Geography*, *27*(2), 230-259.

Oppo, D. W., B. K. Linsley, Y. Rosenthal, S. Dannenmann, and L. Beaufort (2003), Orbital and suborbital climate variability in the Sulu Sea, western tropical Pacific, *Geochemistry Geophysics Geosystems*, *4*.

Oppo, D.W., Sun, Y.B., 2005. Amplitude and timing of sea-surface temperature change in the northern South China Sea: Dynamic link to the East Asian monsoon. Geology 33, 785-788.

Parrenin, F., et al. (2007), The EDC3 chronology for the EPICA dome C ice core, *Climate of the Past*, *3*(3), 485-497.

Partin, J. W., K. M. Cobb, J. F. Adkins, B. Clark, and D. P. Fernandez (2007), Millennial-scale trends in west Pacific warm pool hydrology since the Last Glacial Maximum, *Nature*, *449*(7151), 452-U453.

Partin, J.W. (2008), *Stalagmite reconstructions of western tropical Pacific climate from the last glacial maximum to present.* (Doctoral Dissertation).

Peltier, W. R., and R. G. Fairbanks (2005), Global glacial ice volume and Last Glacial Maximum duration from an extended Barbados sea level record, *Quaternary Science Reviews*, *25*(23-24), 3322-3337.

Percival, D.B., and A.T. Walden (1993), *Spectral analysis for physical applications--Multitaper and conventional univariate techniques*. Cambridge University, 580 pp.

Peterson, L. C., G. H. Haug, K. A. Hughen, and U. Rohl (2000), Rapid changes in the hydrologic cycle of the tropical Atlantic during the last glacial, *Science*, *290*(5498), 1947-1951.

Petit, J. R., et al. (1999), Climate and atmospheric history of the past 420,000 years from the Vostok ice core, Antarctica, *Nature*, *399*(5735), 429-435.

Rafter, P. A., and C. D. Charles (2012), Pleistocene equatorial Pacific dynamics inferred from the zonal asymmetry in sedimentary nitrogen isotopes, *Paleoceanography*, *27*.

Rashid, H., R. Hesse, and D. J. W. Piper (2003), Evidence for an additional Heinrich event between H5 and H5 in the Labrador Sea, *Paleoceanography*, *18*(4).

Robinson R. A. and R. H. Stokes (1955), Electrolyte Solutions. 2nd edn. (revised) Butterworths. London.

Ropelewski, C. F., and M. S. Halpert (1987), Global and regional scale precipitation patterns associated with the El-Niño southern oscillation, *Monthly Weather Review*, *115*(8), 1505-1525.

Rosenthal, Y., D. W. Oppo, and B. K. Linsley (2003), The amplitude and phasing of climate change during the last deglaciation in the Sulu Sea, western equatorial Pacific, *Geophysical Research Letters*, *30*(8).

Rosholt, J.N., Mobilization and weathering, in: M. Ivanovich, R.S. Harmon (Eds.), Uranium Series Disequilibrium : Applications to Environmental Problems, Claren- don Press, Oxford, 1982, pp. 157-180.

Rozanski, K., L. Araguasaraguas, and R. Gonfiantini (1992), Relation between long-term trends of O-18 isotope composition of precipitation and climate, *Science*, *258*(5084), 981-985.

Sachs, J. P., and S. J. Lehman (1999), Subtropical North Atlantic temperatures 50,000 to 30,000 years ago, *Science*, *285*(5440), 755-759.

Schimanski, A., and K. Stattegger (2005), Deglacial and Holocene evolution of the Vietnam shelf: stratigraphy, sediments and sea-level change, *Marine Geology*, *214*(4), 355-387.

Schmidt, G. A., et al. (2013), Using paleo-climate comparisons to constrain future projections in CMIP5, *Clim. Past Discuss.*, *9*(1), 775-835.

Scholz, D., and D. L. Hoffmann (2011), StalAge - An algorithm designed for construction of speleothem age models, *Quaternary Geochronology*, *5*(3-4), 359-382.

Schrag, D. P., J. F. Adkins, K. McIntyre, J. L. Alexander, D. A. Hodell, C. D. Charles, and J. F. McManus (2002), The oxygen isotopic composition of seawater during the Last Glacial Maximum, *Quaternary Science Reviews*, *21*(1-3), 331-342.

Schulz, H., U. von Rad, and H. Erlenkeuser (1998), Correlation between Arabian Sea and Greenland climate oscillations of the past 110,000 years, *Nature*, *393*(5580), 54-57.

Shackleton, N. J., M. A. Hall, and E. Vincent (2000a), Phase relationships between millennial-scale events 54,000-24,000 years ago, *Paleoceanography*, *15*(5), 555-559.

Shackleton, N. J. (2000b), The 100,000-year ice-age cycle identified and found to lag

temperature, carbon dioxide, and orbital eccentricity, *Science*, *289*(5485), 1897-1902.

Shakun, J. D., P. U. Clark, F. He, S. A. Marcott, A. C. Mix, Z. Liu, B. Otto-Bliesner, A. Schmittner, and E. Bard (2012), Global warming preceded by increasing carbon dioxide concentrations during the last deglaciation, *Nature*, *484*(7392), 49-+.

Siegenthaler, U., et al. (2005), Stable carbon cycle-climate relationship during the late Pleistocene, *Science*, *310*(5752), 1313-1317.

Steig, E. J., D. L. Morse, E. D. Waddington, M. Stuiver, P. M. Grootes, P. A. Mayewski, M. S. Twickler, and S. I. Whitlow (2000), Wisconsinan and Holocene climate history from an ice core at Taylor Dome, western Ross Embayment, Antarctica, *Geografiska Annaler Series a-Physical Geography*, *82A*(2-3), 213-235.

Steinke, S., M. Kienast, J. Groeneveld, L. C. Lin, M. T. Chen, and R. Rendle-Buhring (2008), Proxy dependence of the temporal pattern of deglacial warming in the tropical South China Sea: toward resolving seasonality, *Quaternary Science Reviews*, *27*(7-8), 588-700.

Stirling, C. H., T. M. Esat, M. T. McCulloch, and K. Lambeck (1995), High-precision U-series dating of corals from western-Australia and implications for the timing and duration of the last interglacial, *Earth Planet. Sci. Lett.*, *135*(1-4), 115-130.

Stirling, C. H., T. M. Esat, K. Lambeck, and M. T. McCulloch (1998), Timing and duration of the Last Interglacial: evidence for a restricted interval of widespread coral reef growth, *Earth Planet. Sci. Lett.*, *150*(3-4), 745-752.

Storey, M., R. G. Roberts, and M. Saidin (2012), Astronomically calibrated Ar-40/Ar-39 age for the Toba supereruption and global synchronization of late Quaternary records, *Proceedings of the National Academy of Sciences of the United States of America*, *109*(45), 18584-18588.

Stott, L., C. Poulsen, S. Lund, and R. Thunell (2002), Super ENSO and global climate oscillations at millennial time scales, *Science*, *297*(5579), 222-225.

Stott, L., A. Timmermann, and R. Thunell (2007), Southern hemisphere and deep-sea warming led deglacial atmospheric CO(2) rise and tropical warming, *Science*, *318*(5849), 435-438.

Sutton, M. (2009), Review of Distribution Coefficients for Radionuclides in Carbonate Minerals, Lawrence Livermore National Laboratory.

Svensson, A., et al. (2013), Direct linking of Greenland and Antarctic ice cores at the Toba eruption (74 ka BP), *Climate of the Past*, *9*(2), 749-755.

Thomas, A. L., G. M. Henderson, P. Deschamps, Y. Yokoyama, A. J. Mason, E. Bard, B. Hamelin, N. Durand, and G. Camoin (2009), Penultimate Deglacial Sea-Level Timing from Uranium/Thorium Dating of Tahitian Corals, *Science*, *324*(5931), 1185-1189.

Thompson, W. G., M. W. Spiegelman, S. L. Goldstein, and R. C. Speed (2003), An open-system model for U-series age determinations of fossil corals, *Earth Planet. Sci. Lett.*, *210*(1-2), 355-381.

Thompson, W. G., and S. L. Goldstein (2005), A radiometric calibration of the SPECMAP timescale, *Quaternary Science Reviews*, *25*(23-24), 3207-3215.

Thomson, D.J. (1982), Spectrum estimation and harmonic analysis, *Proc. IEEE, 70*, 1055–1095.

Timmermann, A., et al. (2007), The influence of a weakening of the Atlantic meridional overturning circulation on ENSO, *J. Clim.*, *20*(19), 4899-4919.

Timmreck, C. (2012), Modeling the climatic effects of large explosive volcanic eruptions, *Wiley Interdisciplinary Reviews-Climate Change*, *3*(5), 545-554.

Visser, K., R. Thunell, and L. Stott (2003), Magnitude and timing of temperature change in the Indo-Pacific warm pool during deglaciation, *Nature*, *421*(5919), 152-155.

Waelbroeck, C., L. Labeyrie, E. Michel, J. C. Duplessy, J. F. McManus, K. Lambeck, E. Balbon, and M. Labracherie (2002), Sea-level and deep water temperature changes derived from benthic foraminifera isotopic records, *Quaternary Science Reviews*, *21*(1-3), 295-305.

Wang, P. X. (1999), Response of western Pacific marginal seas to glacial cycles: paleoceanographic and sedimentological features, *Marine Geology*, *155*(1-4), 5-39.

Wang, Y. J., H. Cheng, R. L. Edwards, Z. S. An, J. Y. Wu, C. C. Shen, and J. A. Dorale (2001), A high-resolution absolute-dated Late Pleistocene monsoon record from Hulu Cave, China, *Science*, *294*(5550), 2345-2348.

Wang, Y. J., H. Cheng, R. L. Edwards, X. G. Kong, X. H. Shao, S. T. Chen, J. Y. Wu, X. Y. Jiang, X. F. Wang, and Z. S. An (2008), Millennial- and orbital-scale changes in the East Asian monsoon over the past 224,000 years, *Nature*, *451*(7182), 1090-1093.

Weiss, R. F., and B. A. Price (1980), Nitrous-oxide solubility in water and seawater, *Marine Chemistry*, *8*(4), 347-359.

Williams, M. (2012), Did the 73 ka Toba super-eruption have an enduring effect? Insights from genetics, prehistoric archaeology, pollen analysis, stable isotope geochemistry, geomorphology, ice cores, and climate models, *Quaternary International*, *259*, 87-93.

Wolff, E. W., J. Chappellaz, T. Blunier, S. O. Rasmussen, and A. Svensson (2010), Millennial-scale variability during the last glacial: The ice core record, *Quaternary Science Reviews*, *29*(21-22), 2828-2838.

Xie, P. P., and P. A. Arkin (1997), Global precipitation: A 17-year monthly analysis based on gauge observations, satellite estimates, and numerical model outputs, *Bull. Amer. Meteorol. Soc.*, *78*(11), 2539-2558.

Xu, J., A. Holbourn, W. Kuhnt, Z. Jian, and H. Kawamura (2008), Changes in the thermocline structure of the Indonesian outflow during Terminations I and II, *Earth Planet. Sci. Lett.*, *273*(1-2), 152-152.

Yokoyama, Y., K. Lambeck, P. De Deckker, P. Johnston, and L. K. Fifield (2000), Timing of the Last Glacial Maximum from observed sea-level minima, *Nature*, *405*(5797), 713-715.

Yuan, D. X., et al. (2004), Timing, duration, and transitions of the Last Interglacial Asian Monsoon, *Science*, *304*(5570), 575-578.

Zebiak, S. E., and M. A. Cane (1987), A model El-Niño Southern Oscillation, *Monthly Weather Review*, *115*(10), 2252-2278.

Zhang, R., and T. L. Delworth (2005), Simulated tropical response to a substantial weakening of the Atlantic thermohaline circulation, *J. Clim.*, *18*(12), 1853-1850.

Zhao, M., Huang, C.-Y. Wang, C.-C. Wei, G. (2006) A millennial-scale U(37)(K ') sea-surface temperature record from the South China Sea (8 degrees N) over the last 150 kyr: Monsoon and sea-level influence. *Palaeogeography Palaeoclimatology Palaeoecology* 236, 39.